QCD Processes and Hadron Production in High Energy e^+e^- Annihilation

Philip Nicholas Burrows

Oriel College

A thesis submitted for the degree of Doctor of Philosophy
at the University of Oxford

September 1988

QCD Processes and Hadron Production in High Energy e+e- Annihilation

Philip Nicholas Burrows

Oriel College, Oxford

Submitted for the degree of Doctor of Philosophy

Michaelmas Term, 1988

Abstract

A study is presented of general features of the reaction $e^+e^- \rightarrow$ hadrons. The data are interpreted in terms of current models of the underlying QCD and hadronisation processes. These models are outlined in detail and their predictions are compared with most of the available experimental data collected between 12.0 and 46.8 GeV mean centre of mass energies.

The model arbitrary parameters were optimised to give a generally good description of the global properties of the large hadronic event sample accumulated by the TASSO detector at 35 GeV: The Lund $O(\alpha_s^2)$ model describes properties in the event plane very well, but is deficient in the properties transverse to this plane. The Webber LLA model gives a good description of the transverse observables, but overestimates those quantities in the plane. The Lund LLA + $O(\alpha_s)$ model provides a good representation of the transverse properties but underestimates some quantities in the plane, though the discrepancy is much smaller than for the LLA model.

The evolution of the observables as a function of c.m. energy between 12.0 and 41.5 GeV is generally well described, the Lund LLA + $O(\alpha_s)$ model representing the data best. It is concluded that this model is successful in reproducing accurately most features of the data because it includes QCD calculations of both hard and multiple soft gluon emission processes.

The model predictions are extended up to W = 200 GeV, where the two parton cascade models give similar predictions of the event properties which differ significantly from those of the $O({\alpha_s}^2)$ model.

Top quark production is simulated at W = 200 GeV for a top mass of 60 GeV/c^2 and the distributions of thrust, aplanarity, $p_{T_{in}}$, $p_{T_{out}}$ and rapidity are found to be most sensitive to its presence.

The data at 35 GeV are also analysed in terms of explicit multijet final states and compared with the QCD model calculations. The $O(\alpha_s^2)$ model is unable to account for the observed rates of 4- and 5- jets per event, though it reproduces the 2- and 3- jet rates reasonably well. The LLA model gives a better description of the rates of $\geq$ 4-jets but gives too few 3-, and too many 2-jet events. The LLA + $O(\alpha_s)$ model is able to reproduce all jet rates well. All the models describe the trend of the evolution of the jet rates between $< \sqrt{s} >$ = 14 and 43.8 GeV.

It is shown that the rate of 3-jet events seen in the data decreases as s increases in a manner consistent with the Q^2 dependence of α_s as predicted by QCD.

Acknowledgements

A large number of people have contributed to this thesis in many different ways. I am indebted to **all** my family, friends and colleagues who have helped, but am particularly grateful to the following:

First and foremost my mother, who has always given me her love and support no matter how undeserved, and my father and grandmother.

My supervisor, Mike Bowler, for his untiring interest in my work and for always being available to help and advise.

Gunnar Ingelman, from whom I have learned an immense amount in the course of several close collaborations.

David Saxon, for his interest in, and support of, my work.

Paul Dauncey and David Mellor, for tolerating my ignorance and answering my questions.

Klara Albers, Janusz Chwastowski and his family, Alex Martin, Julian Shulman, Dong Su and Ian Tomalin, for enriching life in Hamburg.

Laurence Morland, who has endured six years of my company at Oriel and who thought he had escaped by going to California. Also Matthew Rampley for providing assorted diversions and amusement.

Clare Balkwill, who has endured three years of my company in the Nuclear Physics Laboratory, and her daughter Helen for the free cuddles.

Ian Silvester, Liz Veitch and Jon Nash, for having to share an office with me and surviving.

Liz and James Gillies and Jerry Dodd, for their friendship and support.

Sylvie Strobel-Colleville, for providing me with something to think about beyond this thesis.

All members of the TASSO Collaboration, listed in Appendix A, without whom this thesis would end here.

The taxpayers of the United Kingdom, represented by the Science and Engineering Research Council, for providing partial financial support for this research.

I would also like to thank:

The Lund University particle theory group and Bryan Webber, for writing long and complicated Monte Carlo computer programs.

The Oxford Nuclear Physics and DESY Laboratories, for their hospitality and use of facilities.

Oriel College Boat Club, for use of the 'Arthur Crow'.

The Hamburgische Staatsoper, for such cheap tickets and for keeping me out of mischief.

Oriel College kitchens, for partial nutritional support.

Last, and by no means least, the many other friends and colleagues not mentioned explicitly.

Contents

Chapter 1: Hadron Production in e+e− Annihilation

1.1 Introduction 8
1.2 QCD Calculations of the Total Hadronic Cross Section 13
1.3 $O(\alpha_s)$ Matrix Elements 14
1.4 $O(\alpha_s{}^2)$ Matrix Elements 17
1.5 Parton Cascade QCD Calculations 18
1.6 The Problem of Hadronisation 20
1.7 The Lund $O(\alpha_s{}^2)$ Model 21
1.8 The Webber LLA Model 22
1.9 The Lund LLA + $O(\alpha_s)$ Model 24
1.10 The Gottschalk Model 26

Chapter 2: Experimental Apparatus and Data Selection

2.1 Introduction 27
2.2 Production of High Energy Electrons and Positrons 27
2.2.1 The Accelerator System 27
2.2.2 The Luminosity 28
2.3 The TASSO Detector 30
2.3.1 Introduction 30
2.3.2 The Central Proportional Chamber 32
2.3.3 The Central Drift Chamber 32
2.3.4 The Inner Time of Flight Counters 32
2.4 The Hadronic Event Triggers 33
2.5 Data Reduction and Processing: Selection of Hadronic Events 34
2.5.1 PASS-1 36
2.5.2 PASS-2 36
2.5.3 PASS-3 37
2.5.4 PASS-4 37
2.6 Simulation of the Detector 39

Chapter 3: Inclusive Studies of the Hadronic Final State at W = 35 GeV

3.1 Introduction 42
3.2 Definition of Observables 43

3.3 Event Selection Cuts 44
3.4 Backgrounds to the Data Sample 44
3.4.1 The Two-photon Background 45
3.4.2 The Tau Pair Background 46
3.5 Corrections for MILL Track-finding 47
3.6 Model Parameter Tuning 50
3.6.1 The Tuning Approach 50
3.6.2 The Tuning Method 51
3.6.3 Tuned Parameter Values 52
3.6.4 Comparison with the $D^{*\pm}$ Fragmentation Function 53
3.7 Corrections to the Data 55
3.8 Qualitative Comparison of the Models with the Data 56
3.8.1 The Webber Model 57
3.8.2 The Lund $O(\alpha_s{}^2)$ Model 58
3.8.3 The Lund LLA + $O(\alpha_s)$ Model 58
3.8.4 Summary 59
3.9 A Quantitative Comparison 59
3.9.1 What is χ^2? 59
3.9.2 Comparison of QCD Models with the Data in Terms of χ^2 . . 61
3.10 Conclusion 62

Chapter 4: Energy Evolution of Observables and Model Predictions at Higher Energies

4.1 Introduction 63
4.2 Evolution between $< W > = 12$ and 41.5 GeV 64
4.2.1 The Data 64
4.2.2 Comparison between Models and Data 65
4.2.3 Summary 67
4.3 Predictions of the Models up to $W = 200$ GeV 67
4.3.1 Motivation 67
4.3.2 The Model Results 68
4.4 Differential Distributions at Higher Energies 70
4.4.1 Multiplicity Distributions and KNO Scaling 71
4.5 Summary 72

Chapter 5: Multijet Final States in e^+e^- Annihilation

5.1 Introduction 74
5.2 Event Selection 76
5.3 The Jet Algorithm 77
5.3.1 The Lund Algorithm 'LUCLUS' 77

5.3.2 The JADE Algorithm 'JCLUST' 80
5.4 Jet Rates at $\sqrt{s} = 35$ GeV 82
5.5 Systematic Checks 83
5.5.1 Different Jet Algorithms 83
5.5.2 Change of Model Parameters 84
5.6 Relationship between Hadron Jets and Partons 84
5.7 Energy Evolution of the Jet Rates 85
5.8 The Q^2 Dependence of α_s 87
5.9 Summary and Conclusions 88

Chapter 6: Summary, Conclusions and Outlook 90

Appendix A: The TASSO Collaboration 1978 - 1988 94

Appendix B: The TASSO Coordinate System 96

References 97

CHAPTER 1

HADRON PRODUCTION IN e+e- ANNIHILATION

1.1 INTRODUCTION

This thesis contains a study of aspects of the process $e^+e^- \rightarrow$ hadrons. Our present understanding views this reaction as being divided into two stages: the primary process $e^+e^- \rightarrow$ partons, followed by the transformation of the partons into hadrons.

Our theory of the strong interactions between partons, *i.e.* quarks and gluons, is known as Quantum Chromodynamics (QCD) [1], a so-called renormalisable non-Abelian gauge theory, which is now briefly outlined [2]. The theory describes the interactions of a triplet of spin-1/2 quarks possessing the quantum number colour (c = r,b,g) through an octet of vector gluons within a Yang-Mills gauge theory [3]. The spinor quark fields $q_c(x)$ transform as the fundamental representation of the SU(3) group whilst the gluon fields $A^a_\mu(x)$ (a = 1,2,...,8) transform according to the adjoint representation. The SU(3) colour transformations are generated by the 3×3 matrices $T^a = \lambda^a/2$ where λ^a are the Gell-Mann matrices [4] which obey the commutation relations:

$$[T^a, T^b] \quad = \quad i\, f^{abc}\, T^c \tag{1.1}$$

and f^{abc} are the structure constants of SU(3). The Lagrangian density of QCD has the form:

$$\mathcal{L} \quad = \quad -\frac{1}{4}\, F^a_{\mu\nu}\, F^{\mu\nu,a} \; + \; \bar{q}\,(i\gamma_\mu\, D^\mu \; - \; m)\, q$$

where $F^{\mu\nu}$ is the field strength tensor:

$$F^a_{\mu\nu} \quad = \quad \partial_\mu\, A^a_\nu \; - \; \partial_\nu\, A^a_\mu \; + \; g\, f^{abc}\, A^b_\mu\, A^c_\nu$$

and D_μ is the covariant derivative:

$$D_\mu \quad = \quad \partial_\mu \; - \; i\, g\, T^a\, A^a_\mu(x)$$

g is the bare coupling constant of the theory, m the bare mass of the quark field and the gluons are massless.

Physical quantities such as cross sections can be calculated from the Lagrangian, but are found to be divergent. The infinities are removed by the process of renormalisation in which they are 'absorbed' into the basic constants of the theory such as the couplings and masses, which thereby acquire finite values. The couplings and masses are hence physical constants and cannot be calculated by the theory. The requirement of invariance under a mathematical operation known as a local gauge transformation, described by the gauge group of the theory SU(3), leads to a unique Lagrangian which severely restricts the possible interaction terms between the quarks and gluons. This local gauge invariance is also necessary to ensure that the theory is renormalisable.

The structure of QCD is similar to that of the field theory Quantum Electrodynamics (QED) which describes pure electromagnetic interactions. QED is an Abelian gauge theory, which means that the commutator analogous to (1.1) vanishes. The charged matter fields hence transform by simple phase transformations described by the U(1) group and the field quanta are uncharged. However, QCD is a non-Abelian gauge theory in which the quarks transform under the more complicated SU(3) colour group and the field quanta, *i.e.* gluons, themselves carry colour charge and can interact with one another. An Abelian form of QCD with colour neutral gluons has been ruled out by experiment (see [2] and references therein).

Another characteristic feature of non-Abelian gauge theories is that the coupling strength decreases with the four-momentum-transfer-squared, Q^2, in the interaction. This leads to the property of asymptotic freedom in which, at high Q^2 or small distances, the coupling strength decreases and the quarks and gluons are quasi-free, and explains the observation that in high energy electron-nucleon scattering experiments the electrons scatter off pointlike, freely moving partons within the nucleon [5]. By contrast in large distance or low Q^2 interactions, the coupling strength increases so that quarks and gluons remain bound together or 'confined' in colour singlet states. This is also in agreement with the observation that only colour neutral hadrons, not free quarks and gluons, are produced in particle interactions. Unfortunately, because the coupling strength is relatively large in 'soft' low Q^2 processes, the transition of partons into hadrons, known as hadronisation or fragmentation, cannot be calculated by perturbative QCD methods. Non-perturbative calculations are very difficult; so-called 'lattice' QCD calculations [6] show some promise in predicting static hadronic properties, but as yet there is little progress towards calculation of dynamical processes. At present therefore, hadronisation can only be described by phenomenological models, to be discussed later in this chapter.

The essential features of QCD are thus [2]:

(i) quarks with spin 1/2 exist as colour triplets

(ii) gluons with spin 1 exist as colour octets

(iii) the coupling $q\bar{q}g$ exists

(iv) the couplings ggg and gggg exist

(v) the coupling constants in (iii) and (iv) are equal

(vi) the effective universal coupling g decreases with increasing energy scale like $\ln Q^2$

Most, but not all, of these features have been tested experimentally, and the theory is found to provide an excellent qualitative description of the data. Unfortunately quantitative predictions are difficult to test to high precision, for the QCD calculations of parton-level properties have to be compared with the measured hadrons, a process usually requiring a phenomenological fragmentation model as intermediary, thereby introducing additional theoretical uncertainty. The experimental evidence for (i)-(vi) is briefly reviewed here, for a more detailed review see [2].

As already mentioned, the first direct evidence for the existence of quarks came from the observation at SLAC in 1968 that in electron-nucleon scattering experiments, at high Q^2 the electron scatters from quasi-free pointlike particles carrying roughly one third of the nucleon mass. These particles were identified with the quarks which had been postulated by Gell-Mann and Zweig in 1964 as a calculational device to explain the spectra of mesons and baryons in terms of bound $q\bar{q}$ and qqq (or $\bar{q}\bar{q}\bar{q}$) states respectively [7]. If the quarks are assigned spin 1/2, possess the quantum number flavour (f = u,d,s,c,b) and are triplets in terms of the colour quantum number (c = r,b,g) then a consistent picture of the existence and quantum numbers of virtually all known hadrons can be created*. The colour quantum number is required to explain the existence of states such as Δ^{++} (= u↑u↑u↑) or Ω^- (= s↑s↑s↑), which otherwise should not exist as they contain three quarks in identical quantum states, thereby violating the principles of Fermi-Dirac statistics.

To explain the measured charges of the hadrons the quarks are assigned fractional charges: u(2/3), d(-1/3), s(-1/3), c(2/3), b(-1/3) in units of the electron charge, although alternative models with integer charged quarks have been proposed [8] and have not yet been convincingly excluded experimentally.

The number of colours N_c can be determined experimentally, for the decay width of the reaction $\pi^0 \rightarrow 2\gamma$ should be proportional to N_c^2 within the quark model, and measurements yield $N_c = 3$ [9]. An impressive test is via the measurement of the total hadronic cross section in e^+e^-annihilation. To lowest order in QED:

$$R \equiv \frac{\sigma(e^+e^- \rightarrow \text{hadrons})}{\sigma(e^+e^- \rightarrow \mu^+\mu^-)} = N_c \Sigma\, q_f^2$$

where q_f is the charge of the quark of flavour f and the sum is over all flavours. R therefore also provides a measurement of Σq_f^2. The experimental value at c.m. energy $W = 35$ GeV is $R = 3.90 \pm 0.05$ [10], consistent with the above charge assignment of the quarks, $\Sigma\, q_f^2 = 11/9$, only if $N_c = 3$. The measured value does not agree exactly with the results of this naive calculation because electroweak and QCD effects must also be taken into account; see *eg.* [11]. R is shown as a function of $s = W^2$ in Fig. 1.1, taken from [11], which includes data up to c.m. energies of ~ 52 GeV, the highest energy data published to date [12]; the magnitude of the QCD and electroweak contributions to the simple QPM value is indicated. Sudden increases in R occur at energies marking the thresholds for production of new quark flavours; the c and b thresholds around $s \sim 10$ and 100 GeV^2 respectively are clearly visible. The existence of a sixth quark known as top (t) with charge 2/3 is predicted by the currently accepted Standard Model of elementary particle interactions, although its expected mass cannot be calculated. The top quark would produce a step increase in R of 4/3, which has not yet been observed

* There are a few hadron resonances which have properties which are difficult to interpret in terms of the Quark Parton Model (QPM) and may be candidates for so-called glueball states, particles which are bound states of gluons only.

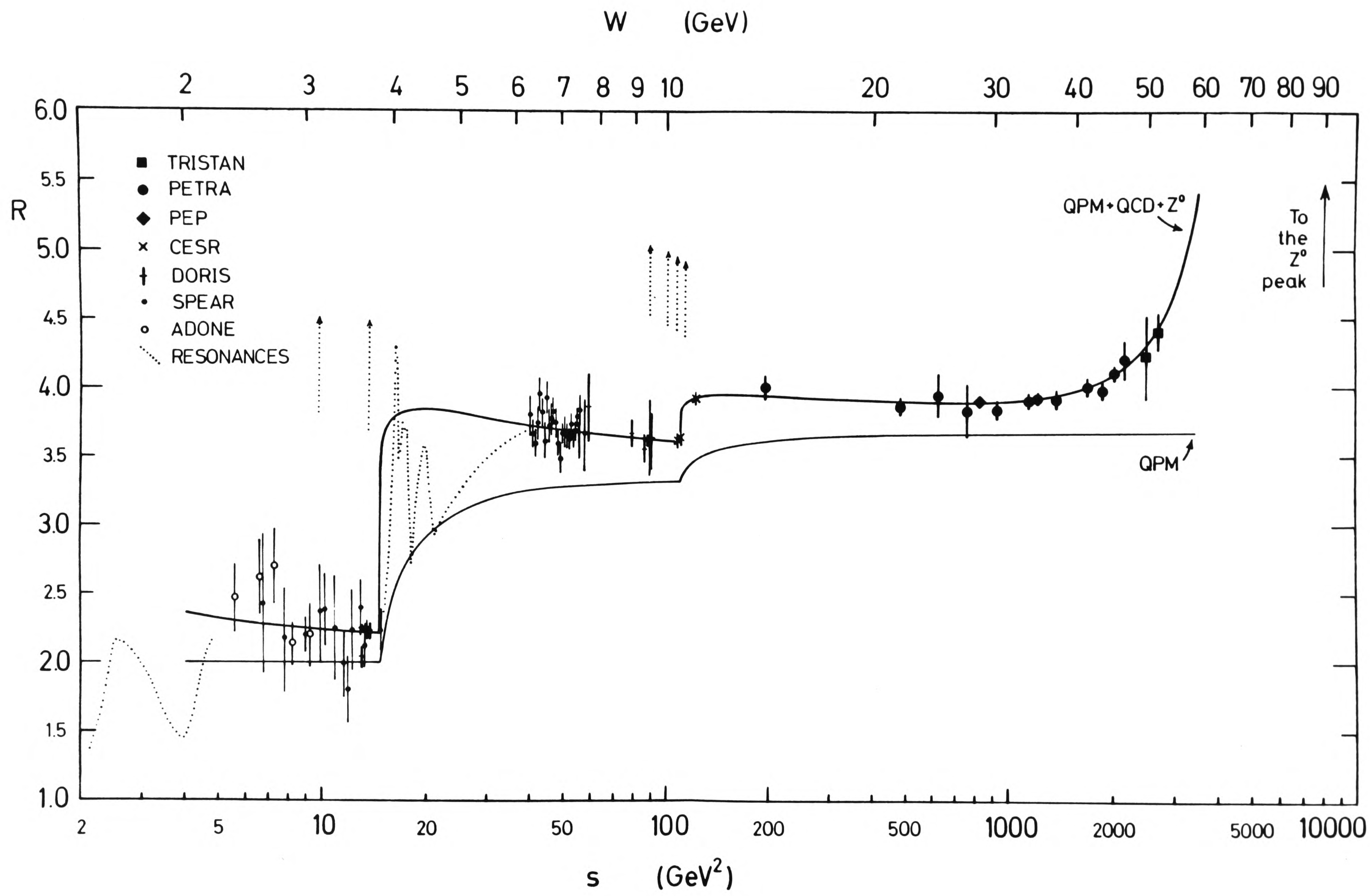

Figure 1.1: The ratio $R = \sigma(e^+e^- \to \text{hadrons})/\sigma(e^+e^- \to \mu^+\mu^-)$ as a function of the centre of mass energy squared.

in e^+e^-collisions at TRISTAN up to 56 GeV, enabling a lower limit of $\sim$ 28 GeV/c^2 to be set upon its mass [13].

The assignment of spin 1/2 to the quarks, in addition to providing a consistent explanation of all known hadron spins, has been verified experimentally in terms of the distribution of the angle θ between the jet axis and the e^+e^-beam direction in hadronic two-jet events (Fig. 1.2a). These events are interpreted in terms of the production of a back-to-back quark-antiquark pair: $e^+e^- \rightarrow q\bar{q}$, which after fragmentation of the colour field between them give rise to two hadronic jets. The angular distribution of the jet axis is predicted to be proportional to $(1 + \cos^2\theta)$, a general result for the single photon production of two massless spin-1/2 particles neglecting electroweak interference effects [14], and has been measured to be so [15,16].

Evidence for the existence of massless electrically neutral particles within the nucleon first came from the discovery that in the electron-nucleon scattering experiments mentioned earlier, only one half of the nucleon momentum was carried by the charged quarks. The remaining momentum can therefore be assigned to the gluons which mediate the strong interaction between the quarks. More direct evidence came from the observation of three-jet events in e^+e^-anihilation (Fig. 1.2b); these are understood in terms of the radiation of a hard gluon by either the quark or antiquark in the final state (Fig. 1.4), each parton giving rise to its own hadron jet after fragmentation [17], and provide a demonstration of the quark-gluon coupling. In addition gluon jets have been observed in high energy proton-antiproton collisions [18]. Even though the gluon has not been observed directly as a particle, there is such an overwhelming amount of evidence for its existence to be beyond reasonable doubt. Measurements of the topologies of three-jet events have also demonstrated that the gluon is a spin-1 particle [19].

Unfortunately properties (iv) - (vi) of QCD have not yet been demonstrated conclusively. The gluon self-coupling can be tested using four-jet events (Fig. 1.2c), interpreted as $e^+e^- \rightarrow q\bar{q}gg$ or $q\bar{q}q\bar{q}$ (Fig. 1.5). The processes in Figs. 1.5a,c may be described as 'QED-like': the radiation of a gluon by a quark in QCD is analogous to the radiation of a bremsstrahlung photon by an electron in QED, whilst the gluon splitting into a $q\bar{q}$ pair is analogous to the conversion of a photon into an e^+e^-pair. However the

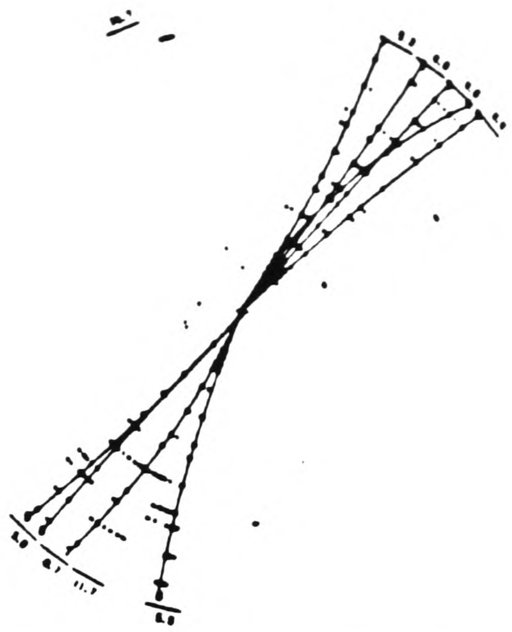

Figure 1.2a: **A two jet event observed in the TASSO detector**

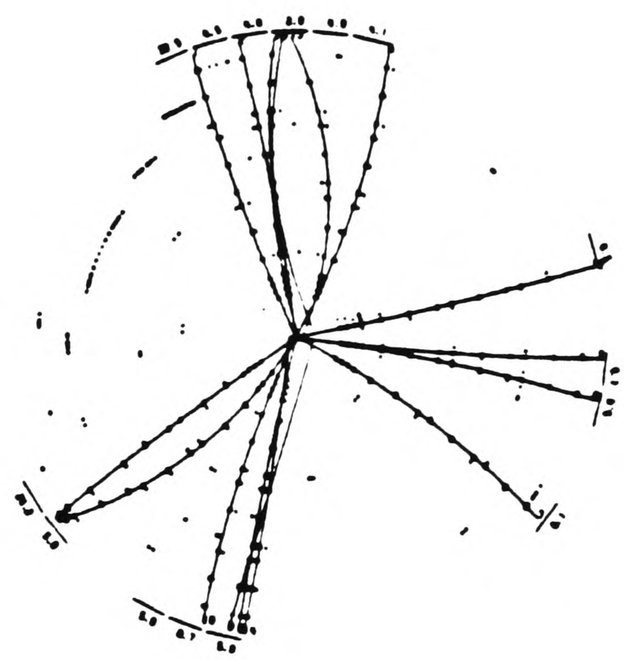

Figure 1.2b: **A three jet event observed in the TASSO detector**

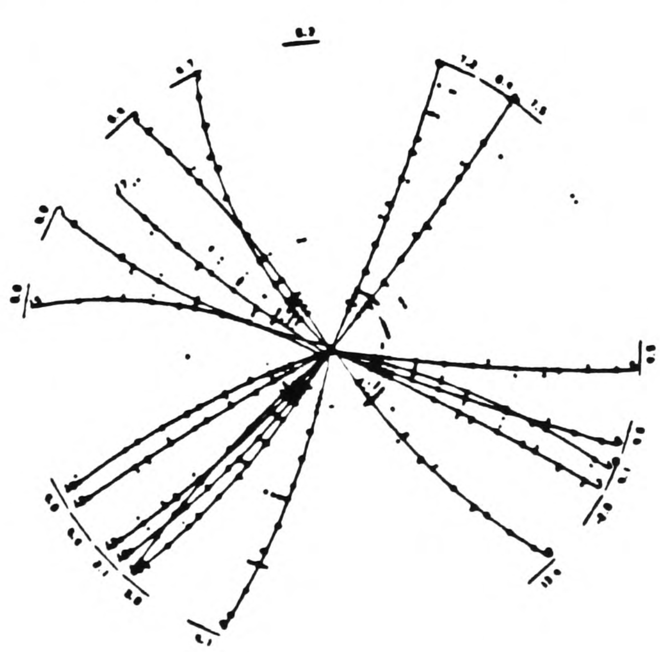

Figure 1.2c: **A four jet event observed in the TASSO detector**

QCD processes in Fig. 1.5b include the gluon self-coupling and have no analogue in QED because the photon carries no electric charge; these events may be described as 'QCD-like'. QCD predicts that a 4-parton event sample is dominated by the QCD-like events and that the angle between the two gluons is peaked at smaller values for these events than for the QED-like events [20]. Monte Carlo calculations have shown (see *eg.* [21]) that the majority of four-jet events, where the jets are reconstructed using some reasonable algorithm (see Chapter 5), arise from four-parton events. Assigning the two lowest energy jets in an event to be the two gluon jets, measuring the distribution of the angle between them and comparing this distribution with the QCD-predicted distributions for the QCD-like and QED-like events therefore provides a test of the gluon self-coupling. Such studies have been performed at PETRA [21,22] but the number of events containing four distinct jets is so low that no conclusion can be drawn from the limited statistics.

The question as to whether the coupling strength decreases as $\ln Q^2$ has not yet been answered conclusively, but will be addressed in Chapter 5.

In summary therefore, QCD is a theory which is in good agreement with experiment wherever it has been tested, though to date the strength of the tests has not been sufficient to put it on as firm a footing as the other components of the Standard Model.

1.2 QCD CALCULATIONS OF THE HADRONIC CROSS SECTION

QCD calculations of the total hadronic cross section involve amplitudes corresponding to parton-level Feynman diagrams. This cross section, derived by squaring the sum of the amplitudes, may be expanded in terms of powers of α_s/π, where α_s is the strong coupling constant: $\alpha_s = g^2/4\pi$ ($\hbar = c = 1$). The Feynman diagrams which give rise to the first three terms in the series are shown in Figs. 1.3-1.5 [23]. Fig. 1.3a shows the 'zeroth' order process in which just a $q\bar{q}$ pair is produced. This process can be calculated from electroweak theory alone, where the quarks couple to the virtual boson through their electric charge. However there are also virtual corrections to $q\bar{q}$ pair production, the $O(g^2)$ and $O(g^4)$ diagrams being shown in Figs. 1.3b, 1.3c respectively. Fig. 1.4a shows the $O(g)$ diagrams giving a $q\bar{q}$ pair + one gluon in the final state, the $O(g^3)$

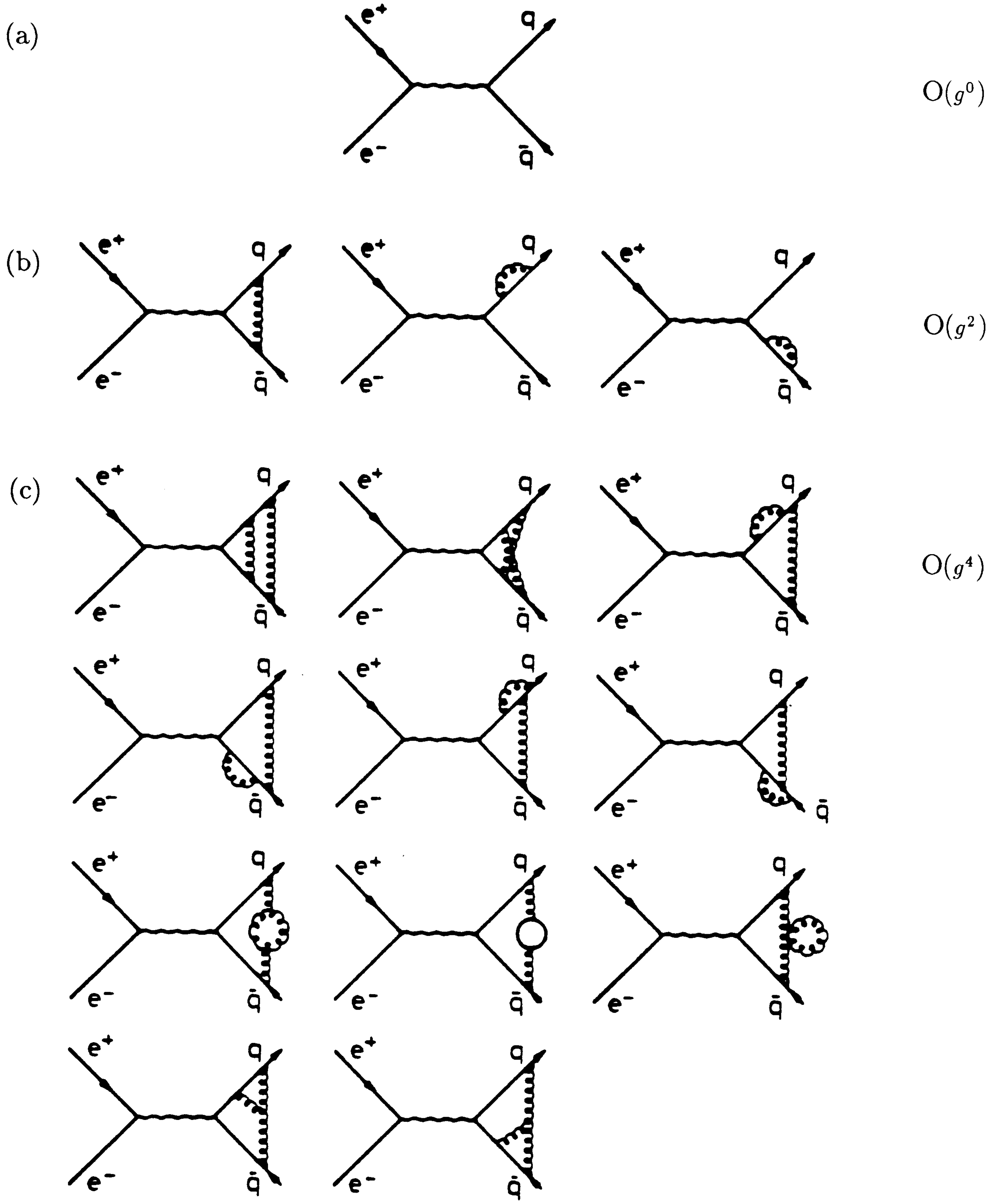

Figure 1.3:

Diagrams for $e^+e^- \to q\bar{q}$: (a) lowest order; (b) radiative correction to order α_s; and (c) radiative correction to order α_s^2.

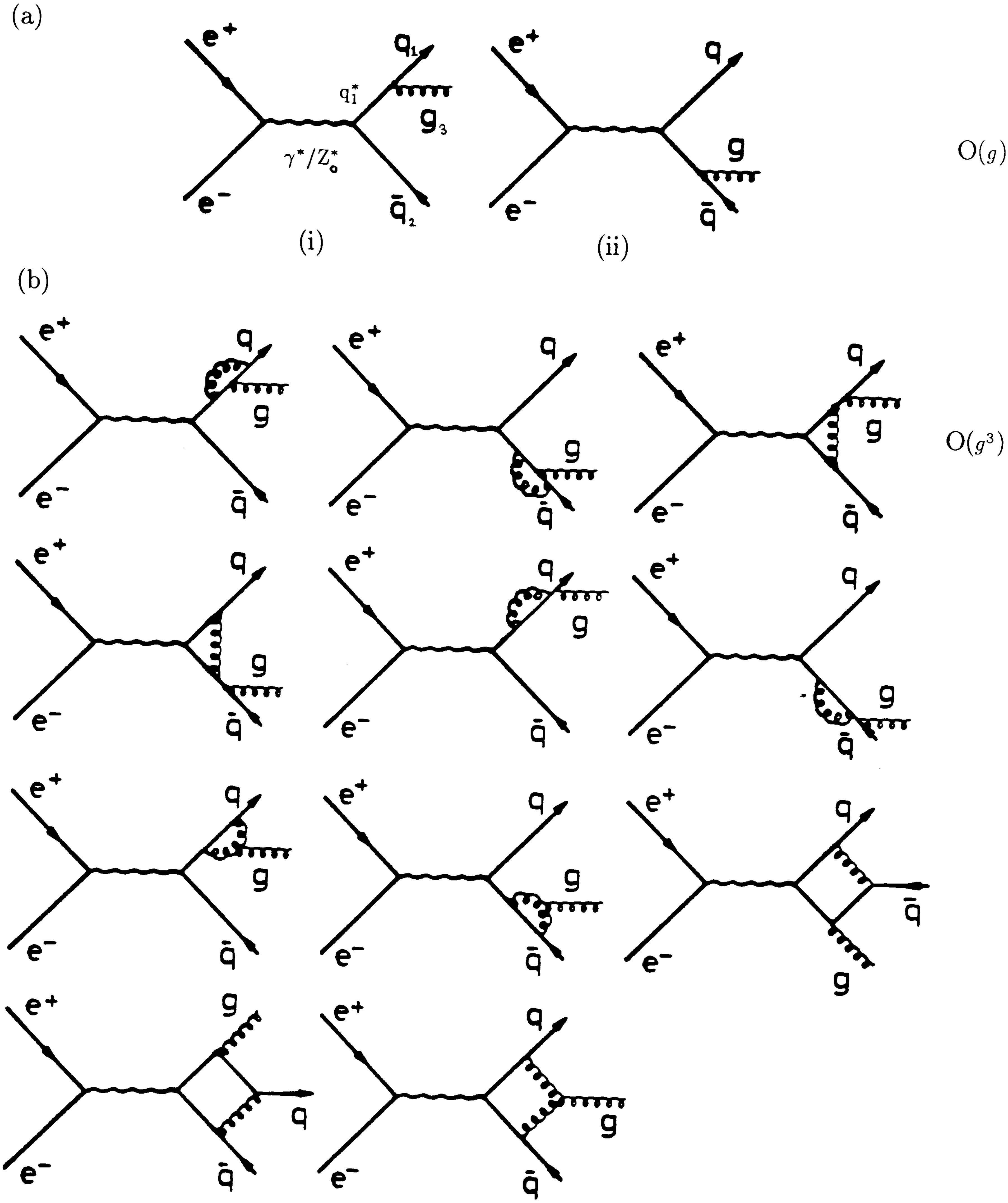

Figure 1.4:

Diagrams for $e^+e^- \to q\bar{q}g$: (a) lowest order; and (b) radiative correction due to the gluon to order α_s.

$O(g^2)$

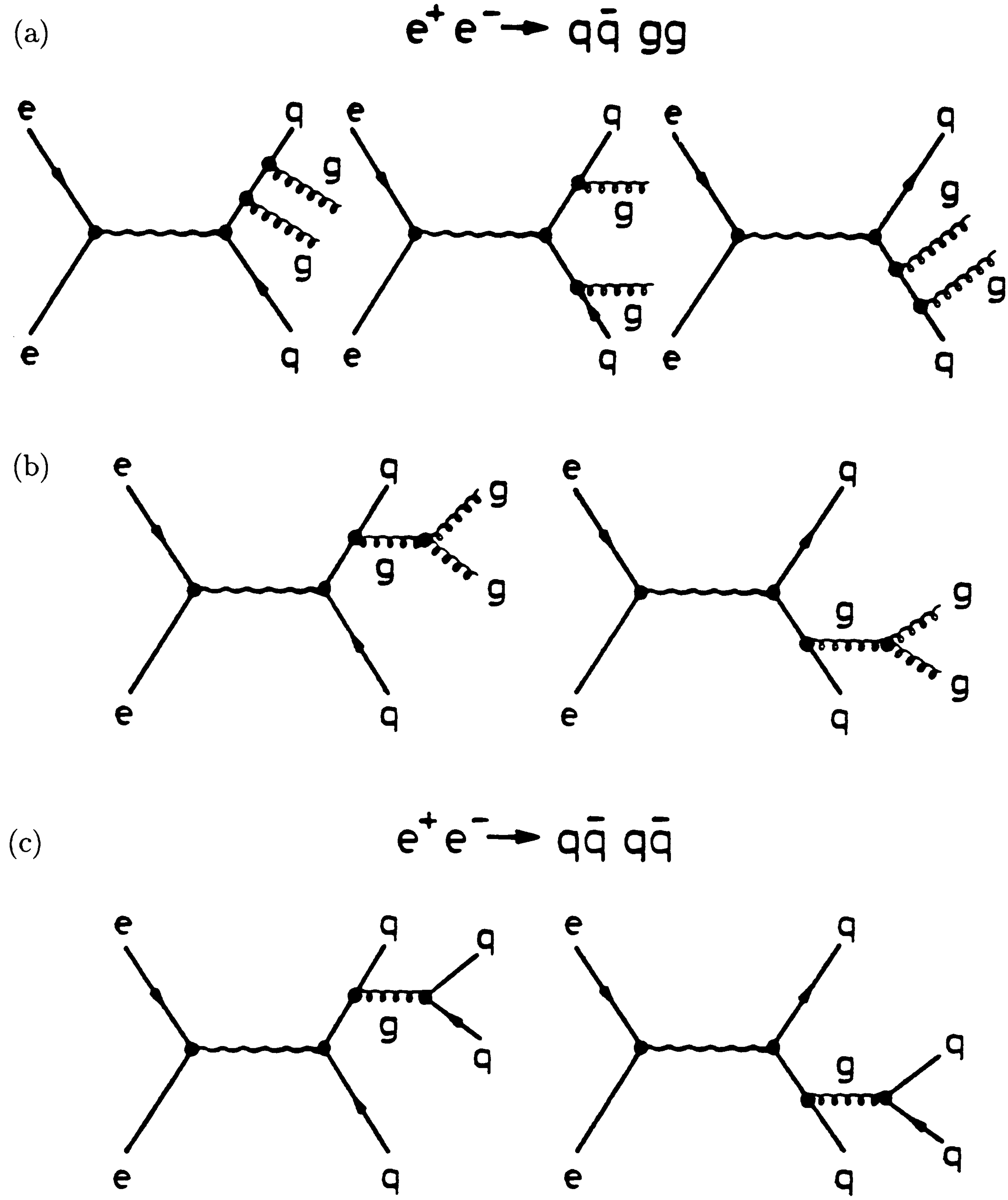

Figure 1.5:

Feynman-diagrams for four-jet events.

virtual corrections to the 3-parton state being shown in Fig. 1.4b. Finally, Fig. 1.5 shows the $O(g^2)$ diagrams giving 4 partons. It is clear that with each successive increase in the power of g, the number of contributing diagrams greatly increases.

Following the parametrisation of [11]:

$$R = 3\sum_f \left(R_f^0 + \left(\frac{\alpha_s}{\pi} + A\left(\frac{\alpha_s}{\pi}\right)^2 + \left(B - \frac{\pi^2}{48}\left(11 - \frac{2N_f}{3}\right)^2 \right)\left(\frac{\alpha_s}{\pi}\right)^3 + \ldots \right) F_f^{ew} \right) \tag{1.2}$$

where N_f is the number of quark flavours f and R_f^0 and F_f^{ew} represent the electroweak interaction terms (see [11] for details).

It is hoped that this series converges otherwise perturbation theory breaks down. Convergence requires *both* that $\frac{\alpha_s}{\pi} < 1$ *and* that the coefficients of $\left(\frac{\alpha_s}{\pi}\right)^n$ do not become very large as the power n increases. The coefficient of $\left(\frac{\alpha_s}{\pi}\right)^2$ has been calculated [24,25]:

$$A = 1.986 - 0.115\,N_f \simeq 1.41$$

and the constant B has been calculated very recently [26]:

$$B = 95.865 - 4.216\,N_f + 0.086\,N_f^2 \simeq 76.94$$

which gives the large value 64.85 for the coefficient of $\left(\frac{\alpha_s}{\pi}\right)^3$. Taking $\alpha_s = 0.2$ as a reasonable value:

$$\frac{\alpha_s}{\pi} : 1.41\left(\frac{\alpha_s}{\pi}\right)^2 : 64.85\left(\frac{\alpha_s}{\pi}\right)^3 \simeq 1 : 0.09 : 0.26$$

The third order term is hence larger than the second and not small relative to the first, which is rather unfortunate as it raises doubts as to whether the series converges and hence whether perturbation theory is applicable.

1.3 $O(\alpha_s)$ MATRIX ELEMENTS

The Feynman diagrams which contribute terms to the hadronic cross section up to and including $O(\alpha_s)$ are those in Figs. 1.3a,b and 1.4a. The amplitudes for all these diagrams are added and squared; $O(\alpha_s)$ contributions arise from the squared amplitudes for Fig. 1.4a and the product of the amplitudes for Figs. 1.3a and 1.3b.

Each of the diagrams in Fig. 1.3b is ultra-violet divergent, *viz* the integrals over the virtual gluon momenta k diverge for $k \to \infty$. Adding the contributions of all three diagrams the divergences cancel. These diagrams also give infra-red divergences, corresponding to $k = 0$, which cancel if one adds the contributions from the process $e^+e^- \to q\bar{q}g$ which are also infra-red divergent (Fig. 1.4a). If the quarks are assumed massless a further divergence arises for these diagrams, the so-called collinear divergence, where the virtual gluon is collinear with the outgoing quark. These divergences are controlled by the process of dimensional regularisation, in which the Feynman diagram amplitudes are calculated for arbitrary dimension $n > 4$. (See [27] for details.)

The differential cross section for production of massless 3-parton final states has been calculated [28]:

$$\frac{1}{\sigma}\frac{d^2\sigma}{dx_1 dx_2} = \frac{2\alpha_s}{3\pi}\frac{x_1^2 + x_2^2}{(1-x_1)(1-x_2)} \tag{1.3}$$

where $x_i = 2E_i/W$ is the parton energy fraction in the hadronic centre of mass frame. The cross section for $m \neq 0$ has also been derived [29] and must be applied near threshold for $e^+e^- \to c\bar{c}g$ or $b\bar{b}g$ where quark masses cannot be neglected. Similarly the $q\bar{q}g$ cross section for $e^\pm$ beams of arbitrary polarisation has been calculated [30] and is a rather complicated expression [2]. Cross sections for observables such as thrust [31] and the energy-energy correlation [32] have been calculated in $O(\alpha_s)$ [33,34] respectively.

The expression (1.3) is singular for $x_1 \to 1$ and/or $x_2 \to 1$. $x_1 \to 1$, $x_2 \neq 1$ corresponds to the radiation of a gluon which is collinear with the q or $\bar{q}$ (the collinear divergence), whilst the other case $x_1 \to 1$, $x_2 \to 1$ corresponds to the radiation of a vanishingly soft gluon (the infra-red divergence). In both cases the gluon is irresolvable from the q or $\bar{q}$. One can therefore define a region of the $q\bar{q}g$ phase space around the singularities where the gluon is irresolvable and one has a two-parton configuration, whilst outside this region all three partons are considered to be resolved. The integral over the singular region actually cancels with the virtual one-loop corrections to $e^+e^- \to q\bar{q}$ (Fig 1.3b) and both the $q\bar{q}$ and $q\bar{q}g$ cross sections hence remain finite.

This singular region of phase space is defined by parton resolution criteria. One such approach is due to Sterman and Weinberg [35] who impose restrictions on the relative angles and energies of parton pairs. Another commonly used method (see *eg.* [36]) is to form the scaled invariant mass-squared:

$$y_{ij} = \frac{m_{ij}^2}{s}$$

for each pair of partons i, j, and to require that all $y_{ij} > y_{min}$ for the event to be counted as a 3-parton event, otherwise it is counted as a 2-parton event. Note, however, that both integrated 2- and 3-parton cross sections now depend on y_{min} [2]:

$$\sigma^{2-\text{parton}}(y_{min}) = \sigma^{(2)}\left[1 + \frac{\alpha_s(Q^2)}{2\pi}C_F\left(-2\ln^2 y_{min} - 3\ln y_{min} + 4y_{min}\ln y_{min} - 1 + \frac{\pi^2}{3}\right)\right]$$

$$\sigma^{3-\text{parton}}(y_{min}) = \sigma^{(2)}\frac{\alpha_s(Q^2)}{2\pi}C_F\left(2\ln^2 y_{min} + 3\ln y_{min} - 4y_{min}\ln y_{min} + \frac{5}{2} - \frac{\pi^2}{3}\right)$$

where $\sigma^{(2)}$ is the $O({\alpha_s}^0)$ contribution.

From a theoretical point of view, y_{min} cannot be chosen too small otherwise $\sigma^{3-\text{parton}}$ can exceed σ^{tot} and $\sigma^{2-\text{parton}}$ can be negative, which is unphysical. On the other hand y_{min} should not be too large otherwise the 3-parton cross section will be very small, in contradiction to the experimental observation of 3-jet events. $y_{min} \sim 0.02$ is often used in the PETRA c.m. energy range $12 \leq W \leq 47$ GeV and gives a rate of resolved 3-parton events of about 70% at $W \sim 35$ GeV [22]. The relationship between the resolved 3-parton events and the experimentally resolved 3-jet events is discussed in Chapter 5.

From above it can be seen that the inclusive 3-parton cross section is directly proportional to α_s, which, to first order, is given by [37]:

$$\alpha_s^{(1)}(Q^2) = \frac{12\pi}{(33 - 2N_f)\ln(\frac{Q^2}{\Lambda^2})} \tag{1.4}$$

where N_f is the number of active flavours. The fundamental constant of QCD is hence not the coupling $\alpha_s(\sim g^2)$ but the scale parameter Λ. Here Q^2 is usually taken to be s, the hadronic c.m. energy-squared.

1.4 O($\alpha_s{}^2$) MATRIX ELEMENTS

Second order perturbative QCD calculations are very involved; the amplitudes corresponding to all the diagrams in Figs. 1.3 - 1.5 must be summed and squared, including the gluon self-coupling diagrams (Fig. 1.5b) which appear for the first time. The collinear and infra-red divergences are handled in the way described in Section 1.3, by dimensional regularisation and by isolating the singular regions of phase space using the same parton resolution criteria. The diagrams in Fig. 1.5 thus contribute to the 2,3 and 4-parton cross sections, the first (second) case being when two (one) parton pairs are collinear or two (one) partons are vanishingly soft; those in Fig. 1.4 contribute to the 2 and 3-parton cross sections and those in Fig. 1.3 only to the 2-parton cross section. Again, the singularities arising from the integrals over the degenerate regions of phase space cancel, yielding finite integrated 2,3 and 4-parton cross sections which are functions of y_{min} (see [2] for details). For $y_{min} = 0.02$ the rate of events containing four resolved partons is roughly 10% at $W = 35$ GeV (see Chapter 5).

The coupling α_s is not uniquely defined, but depends on technical details such as the renormalisation scheme used (see *eg.* [2,38]) and the definition of the Q^2 scale. In calculating a physical quantity up to O($\alpha_s{}^n$) at the parton level, one attempts to choose a scheme which minimises the values of the (uncalculated) higher order corrections O($\alpha_s{}^{n+1}$) *etc.* Clearly this can only be done at O($\alpha_s{}^2$) (or higher), where the second order terms can be compared with the first order ones so that the Q^2 scale which optimises the perturbation theory can be chosen. The most commonly used prescription is the modified minimal subtraction ($\overline{\mathrm{MS}}$) scheme, in which [24]:

$$\alpha_s^{(2)}(Q^2) = \frac{12\pi}{(33-2N_f)\ln(Q^2/\Lambda^2_{\overline{MS}}) + 6(153-19N_f)/(33-2N_f)\ln(\ln(Q^2/\Lambda^2_{\overline{MS}}))} \tag{1.5}$$

and $Q^2 = s$.

Within this scheme the O($\alpha_s{}^2$) corrections to observables such as the total hadronic cross section are typically of the order of a few per cent, so that it was hoped that the O($\alpha_s{}^3$) + higher terms would be by comparison very small, *viz* that the perturbative series (equation 1.2) converges fast, although the recent calculations to O($\alpha_s{}^3$) (Section 1.2) have cast some doubt on this.

Parton-level calculations complete to $O(\alpha_s{}^2)$ are thus complex and difficult. There have been several independent calculations for massless partons within the $\overline{\mathrm{MS}}$ scheme [36,39,40,41,42]. Historically there is some controversy concerning these calculations (see *eg.* [42,43]), though the differences between the results of the various groups are now understood. Probably the most widely used matrix elements are due to Gutbrod, Kramer and Schierholz [41] where certain approximations were made. It has subsequently been shown [42] that the difference between the approximate and an exact calculation produces a decrease in the 3-parton cross section by roughly 10%. The consequences of this will be mentioned in Chapter 5.

1.5 PARTON CASCADE QCD CALCULATIONS

The calculation of third, let alone higher, order QCD contributions in perturbation theory is even more complex due to the large number of Feynman diagrams contributing. The third order term in the perturbative expansion for R has recently been calculated, but presently the second order calculation is the best 'exact' matrix element calculation of parton cross sections available. An alternative perturbative treatment is provided by the Leading Logarithm Approximation (LLA). In this approach the quarks produced in $e^+e^- \rightarrow q\bar{q}$ may be very much off mass-shell and are allowed to radiate gluons, which may themselves branch into parton pairs. A parton shower or cascade thereby develops (Fig. 1.6).

The probability for each branching is given by the Altarelli-Parisi equations [44]*, derived for an 'infinite momentum frame' where all parton energies are much larger than their masses:

$$\mathrm{d}^2 P_{a\rightarrow \mathrm{bc}}(m^2, z) \quad = \quad \frac{\alpha_s(Q^2)}{2\pi}\frac{\mathrm{d}m^2}{m^2}\, P_{a\rightarrow \mathrm{bc}}(z)\mathrm{d}z$$

which lead to the Sudakov form factor. That is, the probability that a parton with a maximum (virtual) mass m **does not** branch between m and a minimum mass m_{min} is:

* These equations are only strictly valid in the collinear limit.

$$S_a(m^2) \quad = \quad \exp\left(-\int_{m^2_{min}}^{m^2} \frac{\mathrm{d}m^2}{m^2} \int_{z_-(m)}^{z_+(m)} \frac{\alpha_s(Q^2)}{2\pi}\, \mathrm{d}z\, P_{a\to bc}(z)\right) \qquad (1.6)$$

where $P_{a\to bc}(z)$ is the Altarelli-Parisi splitting kernel [44] for the branching $a \to b\,c$ in which the daughter takes some fraction z of the parent's momentum, *eg.*

$$P_{q^*\to qg}(z) \quad = \quad \frac{4}{3}\,\frac{1+z^2}{1-z}$$

and m_{min} is a small cutoff scale which prevents divergences in $P(z)$.

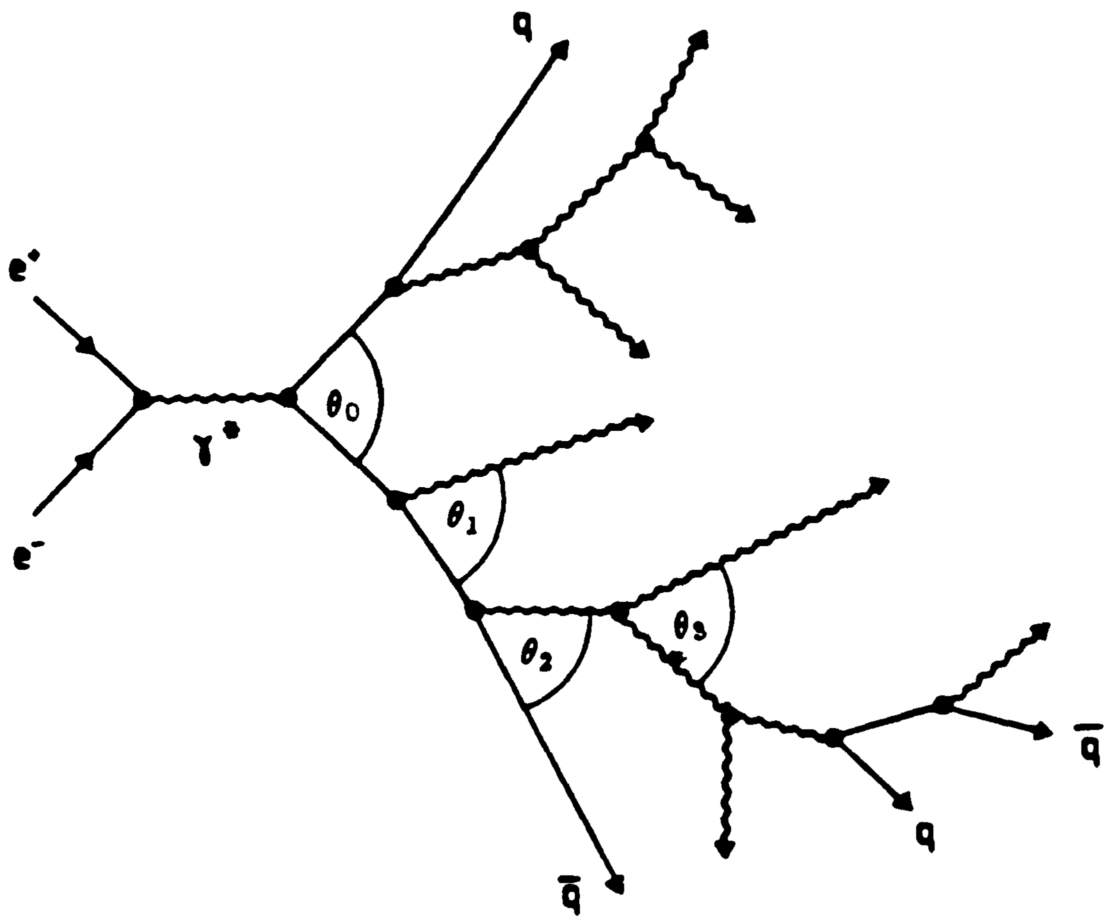

Figure 1.6: Schematic representation of a parton cascade.

The total cross section for the shower is assumed to be proportional to the product of independent probabilities, one for each branching, *viz* no interference between diagrams for all possible branchings in the shower is taken into account. The LLA model thus incorporates many orders of α_s. Such an iterative Markov process is suitable for Monte Carlo simulation, and several models have been developed in recent years [45]. The latter assumption is a good approximation in the case in which the Q^2 at each branching is much less than that at the preceeding branching in the cascade. This approximation is poor when a hard parton is emitted at large angle relative to the parent's trajectory. A decreasing Q^2 at successive parton branchings is built into the formalism, so that the most energetic wide-angle parton radiated by the q or $\bar{q}$ is usually the first gluon emitted. The LLA may therefore be expected to estimate poorly, relative to an exact calculation, the cross section for partonic states containing a hard gluon, namely 'hard 3-jet events'. Note that this may be *either* an **under**estimate *or* an **over**estimate depending on the details of the calculation.

There are in principle only two parameters which affect the cascade evolution: the QCD scale Λ_{LL}, and Q_0 defining the virtuality beneath which partons are not allowed to radiate; both of these regulate the amount of parton bremsstrahlung. It must be noted that Λ_{LL} is **not** the same as $\Lambda_{\overline{MS}}$; $\Lambda_{\overline{MS}}$ is extracted from a finite order calculation within a certain renormalisation scheme, whereas Λ_{LL} is not well defined but is supposed to approximate the Λ used in an infinite order calculation. In experimentally determining Λ by comparing QCD model calculations with data one might therefore expect $\Lambda_{\overline{MS}} > \Lambda_{LL}$; the lack of multiple parton emission in the finite order calculation being made up by boosting the amount of emission to $O({\alpha_s}^2)$.

1.6 THE PROBLEM OF HADRONISATION

The QCD calculations discussed so far concern the properties of the final state partons produced by the e^+e^-annihilation. Experimentally one observes composite colour singlet states, namely hadrons. No free coloured state has ever been seen, although one experiment claims to find fractional charge [46]. In order to compare the predictions of the QCD calculations with experimental data one therefore needs a model of hadronisation.

As it is believed that QCD provides the correct description of the interaction of coloured partons via the strong force, there being no experimental evidence to the contrary, in principle it should also provide a description of soft processes in which quarks become confined in colour singlet hadrons. This confinement property can be understood in terms of the Q^2 dependence of α_s. From equations 1.4 and 1.5 it can be seen that as $Q^2 \rightarrow \Lambda^2$, $\alpha_s \rightarrow \infty$, *viz* at low Q^2 (*i.e.* large separations) in parton interactions the strong force becomes very large, so that individual 'free' partons cannot exist. However, from equation 1.2, if $\alpha_s/\pi \sim 1$ the perturbative series does not converge and the calculation breaks down. The QCD scale Λ is not well determined experimentally, but seems to lie between about 0.1 and 0.7 GeV [38], so that α_s/π becomes $>> 1$ for $Q^2 \leq \sim 1$ GeV^2.

Because of this inapplicability of perturbative QCD at a scale ~ 1 GeV, the hadronisation schemes imposed after the parton production are by necessity phenomenological. The phenomenology, however, must itself be a manifestation of QCD from which we may eventually deduce a sound theory of hadronisation.

Theoretical models of the process $e^+e^- \rightarrow$hadrons therefore comprise a perturbative QCD calculation of the final parton state together with a phenomenological scheme to describe the fragmentation of the parton system into observable hadrons. There are arbitrary parameters associated with both of these processes. Such models are usually incorporated into Monte Carlo event generator programs. The bulk of this thesis is concerned with the predictions of the three most successful of these 'perturbative QCD + fragmentation' models, described below. For a comprehensive review of this field see [47]; see also [48] for a discussion of some underlying physics matters.

1.7 THE LUND O($\alpha_s{}^2$) MODEL

The Lund O($\alpha_s{}^2$) model generates up to 4-parton states according to the GKS matrix element (ME) calculations [41] and is included as a parton level generator option in JETSET version 6.3 [49]. The parameters for the ME calculation are the QCD scale $\Lambda_{\overline{MS}}$ and the parton pair resolution cutoff y_{min} (see Section 1.3).

Hadronisation is imposed after the parton production according to the Lund string model [50]. A colour triplet string is stretched between the final quarks, the gluons being kinks on the string, with the correct colour ordering; this may be interpreted physically as representing the colour flux tube arising from the non-Abelian QCD field between the partons [51]. The string is then fragmented according to the Lund recipe to obtain the final state hadrons: the probability that a hadron h produced directly from the string break-up will carry a momentum fraction $z = (E + p_{\parallel})_h/(E + p_{\parallel})_q$ is*

* This should not be confused with the variable 'z' used in the parton cascade

$$f(z) = \frac{1}{z}(1-z)^a \exp\left(-\frac{bm_T^2}{z}\right) \qquad (1.7)$$

where q refers to the initial quark, $m_T^2 = p_T^2 + m^2$ is the hadron transverse mass-squared and a, b are parameters. This fragmentation function is used for all flavours of the initial $\mathrm{q\bar{q}}$ and is said to be symmetric; this means that on average the same results are obtained independent of whether the iterative fragmentation is started from the q or $\bar{\mathrm{q}}$ end of the string, a result which is only true for a very limited class of functions [52]. The quarks from the string are given a transverse momentum according to a Gaussian distribution $\sim e^{-p_T^2/2\sigma^2}$ whose width, σ, is another free parameter of the model. There are other string fragmentation parameters, such as the strange quark- and various diquark- suppression factors, which are of secondary importance to the inclusive global properties of hadronic final states.

After the string break-up, hadrons containing heavy quarks (b,c), and hadron resonances, are then decayed [53] to give 'stable' particles: pions, kaons, electrons, muons, neutrinos and the corresponding antiparticles.

1.8 THE WEBBER LLA MODEL

Version 4.2 of the program BIGWIG is considered, implementing the physics in [54]. In the primary process $e^+e^- \to \gamma/Z \to \mathrm{q\bar{q}}$ the initial quark and antiquark are assigned maximum allowed virtualities according to a particular distribution and are boosted to a frame in which their directions are perpendicular, one consequence being that the model does not preserve strict Lorentz invariance; it has been shown [55] that the final hadronic system is sensitive to the virtuality assignment and the boost factor γ, though these issues are not considered here. The off-mass-shell quarks then emit gluons, which may themselves radiate other gluons or split to $\mathrm{q\bar{q}}$ pairs, producing a parton cascade as described in Section 1.5. Parton virtualities thereby decrease by bremsstrahlung as the cascade evolves, the process being stopped when the virtuality of each parton falls below a cutoff value Q_0, whence it is put on mass shell.

---

calculations (Section 1.5).

Soft gluon interference terms [56] are included by the imposition of 'angular ordering' of the parton branchings, *i.e.* the angle θ_i between two daughter partons in a branching i is less than the angle at the previous branching (*eg.* $\theta_3 < \theta_2 < \theta_1 < \theta_0$ in Fig. 1.6), the very first branching angle being set at 90^0 by the boost. This requirement restricts the phase space for soft gluon emission, which corresponds physically to gluons of long wavelength being unable to resolve the individual colour charges of the partons in the cascade, which therefore acts coherently for soft gluon production. It has been shown [57] that such a 'coherent' cascade model with cluster hadronisation is able to reproduce the 'string effect' [58], the depletion of particles in the region opposite the gluon-assigned jet in planar 3-jet events in e^+e^-, whilst a cascade + cluster model without the interference [59] (a 'conventional' or 'incoherent' cascade) shows no such depletion. The interference effects are small at PETRA energies, even at the parton level [60], and are diminished by hadronisation [61], though they may be large at very high energies [62,63].

α_s is allowed to 'run' throughout the cascade, the first-order formula (equation 1.4) being used at each branching, with Q^2 decreasing at successive branchings. There is some degree of theoretical arbitrariness as to the choice of Q^2 scale; in this model $Q^2 \simeq p_T^2$ is used, as it is suggested [64] that this choice may effectively take into account higher order corrections to the interference effects.

At the termination of the cascade, when all partons have been put on mass shell, all gluons are split into $q\bar{q}$ pairs, each parton then joining with a neighbour of the correct colour index to form a colourless cluster. Heavy quarks (b,c) are then decayed. Clusters whose mass exceeds a certain value M_c are split into two and all clusters are allowed to decay by phase space, via resonances, to stable final state particles. This hadronisation mechanism is not infra-red stable, in that the radiation of additional very soft gluons can considerably alter the arrangement of colourless clusters and hence change the resulting hadronic final state.

The three most important arbitrary parameters in the Webber model are hence the cascade virtuality cutoff Q_0, the LLA scale parameter Λ_{LL} and the cluster mass parameter M_c. Alternative prescriptions for setting up the cascade within the basic framework of the Webber model involve other parameters [55,65], but these will not be considered here.

(A new program [66] incorporating a revised model [67] with additional QCD features [68] has been made available only very recently, and hence no results are shown in this thesis.)

1.9 THE LUND LLA + O(α_s) MODEL

The latest Lund cascade model [69] is also included as a parton-level generator option in JETSET version 6.3; the inclusion of the O(α_s) matrix element in the calculation in a theoretically satisfying way is an important development and will hence be described in some detail here.

The cascade evolves according to the Altarelli-Parisi equations with evolution variables m and z (Section 1.5), *eg.* referring to Fig. 1.4a(i), $m = m_{1^*}$ and $z = z_1$:

$$z_1 = \frac{p_0 \cdot p_1}{p_0 \cdot p_{1*}} = \frac{E_1}{E_{1*}}$$

where the latter equality is valid in the rest frame of the virtual boson. From equation 1.6, branches are generated by solving for m:

$$S_a(m^2) = \frac{S_a(m^2_{max})}{R}$$

where R is a random number between 0 and 1 and $m_{max} \sim \sqrt{s}$. z is chosen according to $P(z)$ (Section 1.5). Note that the mass of the decaying parton is only fixed by the branching.

There is no boosting of the initial q$\bar{\text{q}}$ pair to a frame in which they are at 90^0. Instead the first parton branching is defined by matching the cascade onto the exact O(α_s) matrix element by using a rejection technique: summing the LLA probabilities for diagrams 1.4a(i) and (ii) leads to the following 3-parton cross section:

$$\frac{1}{\sigma}\frac{\mathrm{d}^2\sigma}{\mathrm{d}x_1\mathrm{d}x_2} = \frac{2\alpha_s}{3\pi}\frac{A_{shower}(x_1,x_2)}{(1-x_1)(1-x_2)}$$

where [69]:

$$A_{shower}(x_1,x_2) = 1+\frac{1-x_1}{(1-x_1)+(1-x_2)}\left(\frac{x_1}{2-x_2}\right)^2+\frac{1-x_2}{(1-x_1)+(1-x_2)}\left(\frac{x_2}{2-x_1}\right)^2$$

A form is thus reached which is very similar to the exact $O(\alpha_s)$ 3-parton matrix element (equation 1.3), having an identical singularity structure. This provides an opportunity to correct for the neglect of the interference terms between 1.4a(i) and (ii) in the leading logarithm result: All branches in the parton cascade are generated according to the Sudakov form factor, but the **first** is accepted with a probability:

$$p = \frac{d^2\sigma_{matrix}}{d^2\sigma_{shower}} = \frac{A_{matrix}}{A_{shower}}$$

where $A_{matrix} = x_1^2 + x_2^2$ and $A_{matrix} < A_{shower}$ for all x_1,x_2, *i.e.* the LLA calculation **overestimates** the 3-parton cross section relative to the exact $O(\alpha_s)$ result. p is simply a well-behaved function of x_1 and x_2 which approaches unity in the limit x_1 or $x_2 \to 1$ and 9/20 in the region $x_1 = x_2 = 1/2$. By thus combining the LLA cross section with a probability determined from the 3-parton matrix element one should reproduce the correct rate of hard 3-jet events and compensate for the phase space region in which the LLA is known to be a poor approximation.

Coherence is imposed, in a manner analogous to the angular ordering described in the previous section, by an ordering of successive branchings in terms of m, z; *eg.* referring to Fig. 1.4a(i):

$$\frac{z_1(1-z_1)}{m_1^2} > \frac{(1-z_{1^*})}{z_{1^*}m_{1^*}^2}$$

All quantities in this inequality are Lorentz invariants, so that the whole branching process is formally Lorentz invariant, though the gauge changes from one vertex to the next.

The cascade model has two arbitrary parameters: the virtuality cutoff Q_0 and the LLA scale parameter Λ_{LL}, though there are certain theoretical degrees of freedom in the treatment of the kinematics of the cascade evolution, as well as in the choice of Q^2 scale for α_s (see [70] for a more complete discussion). For all results presented here the prescriptions chosen in the default version of JETSET [61] have been used, where *eg.* $Q^2 \simeq p_T^2$. Hadronisation after the parton production is imposed according to the Lund string model as briefly discussed in Section 1.7. The same string fragmentation parameters are involved, though they are not necessarily expected to have similar values as for the $O(\alpha_s{}^2)$ model because the parton configurations are very different in the two cases (see Chapter 3). This fragmentation scheme is infra-red stable, *viz* the hadronic final state is insensitive to the addition of very soft gluons to the parton configuration, which simply appear as vanishingly small kinks on the string.

1.10 THE GOTTSCHALK MODEL

The Caltech-II model [71] is a rather complicated mixture of QCD calculations and phenomenology. The multiparton system produced by a coherent parton cascade is broken up into smaller mass colourless subsystems, *i.e.* clusters, by a string mechanism. The clusters are then decayed according to a parametrisation of low energy data, a scheme much more complicated than the phase space description used by Webber. A large number of parameters is involved, though it is claimed that many of these are either redundant or well-constrained by the low energy data. A detailed study of this model has shown [72] that it does not provide a particularly good description of most global features of e^+e^- annihilation data at $W = 29$ GeV, and compares unfavourably with the three models mentioned in Sections 1.7 - 1.9. The Caltech-II model will hence not be further discussed here.

CHAPTER 2

EXPERIMENTAL APPARATUS AND DATA SELECTION

2.1 INTRODUCTION

The analysis described in this thesis uses data collected by the TASSO (Two Arm Spectrometer SOlenoid) detector, located in the south east interaction region of the e^+e^- storage ring PETRA (Positron-Elektron Tandem Ring Anlage) at the DESY (Deutsches Elektronen-SYnchrotron) laboratory in Hamburg, Federal Republic of Germany. The main features of PETRA are outlined in Section 2.2 and details of the components of TASSO relevant to this analysis are given in Section 2.3. The experimental trigger for hadronic events is mentioned in Section 2.4, whilst the data reduction scheme and event selection criteria are presented in Section 2.5. Section 2.6 describes the computer program used to simulate the detector effects. All of these details have been extensively described previously [55,73,74].

2.2 PRODUCTION OF HIGH ENERGY ELECTRONS AND POSITRONS

2.2.1 The Accelerator System

The system of accelerators at the DESY laboratory is shown in Fig. 2.1. Electrons are initially accelerated to an energy of 50 MeV in the linear accelerator LINAC I and then injected into the synchrotron ring DESY, where they are further accelerated to 7 GeV, before finally being injected into the PETRA storage ring. Positrons are produced by bombarding a heavy metal target (copper, tungsten or lead) with a 150 MeV electron beam. The electrons shower in the target and produce positrons via e^+e^-pair production from bremsstrahlung photons. The positrons are then accelerated to 400 MeV in LINAC II, accumulated in the PIA (Positron Intensitäts Akkumulator)

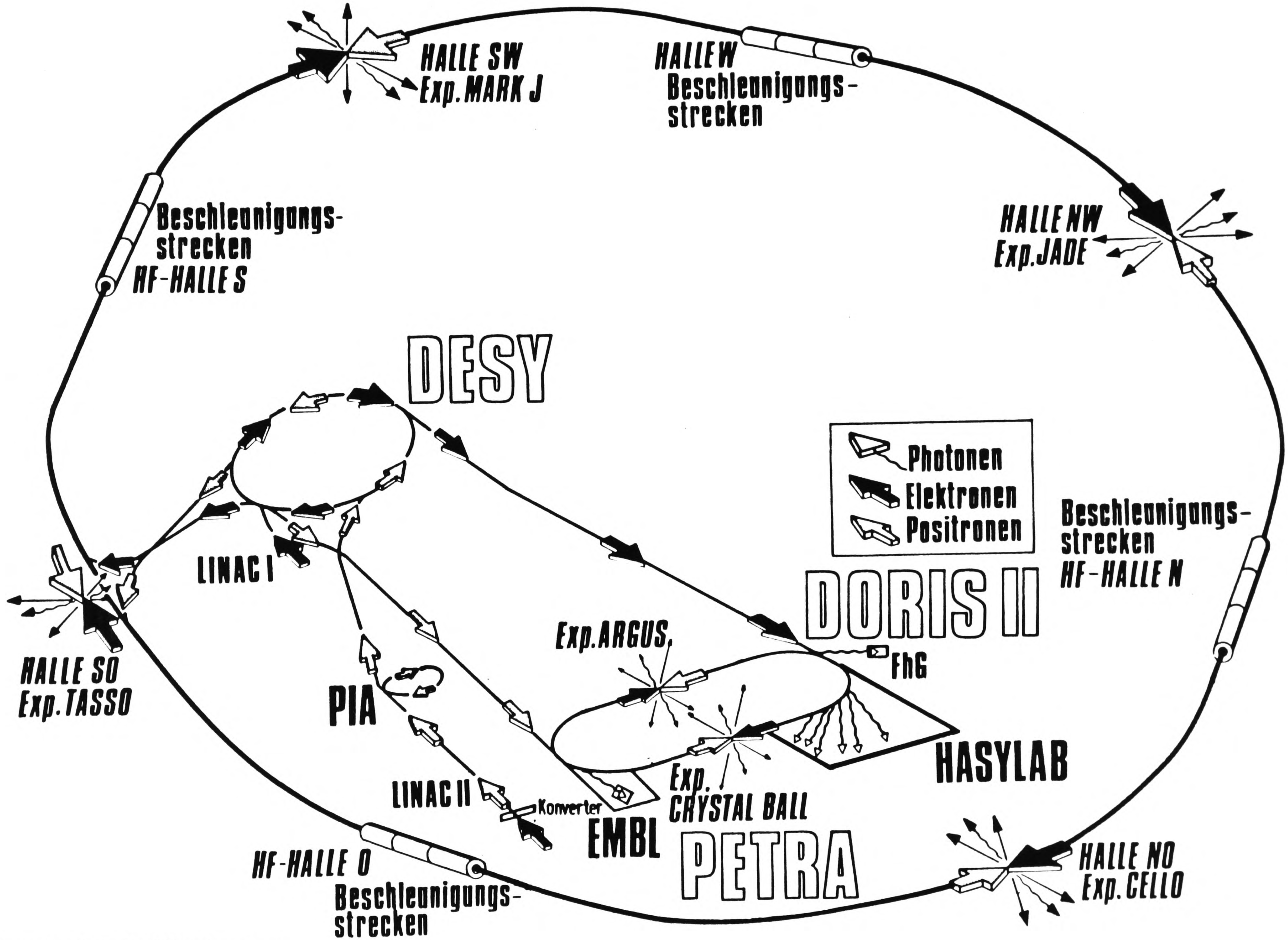

Figure 2.1: Layout of the DESY laboratory.

and injected into DESY for acceleration up to 7 GeV. Both electrons and positrons at 7 GeV are transferred to PETRA until a sufficiently high beam current, typically several mA, is obtained, at which point the beams are accelerated to the required energy.

The PETRA 'ring' has a perimeter of 2.3 km and consists of four long straight sections (Fig. 2.1) housing the radiofrequency cavities for accelerating the beams, joined by circular arcs containing bending and focusing magnets. The electron and positron beams circulate in opposite directions within the same vacuum pipe, which is maintained at 10^{-9} torr. At the centre of each of the four arcs is a short straight section where the beams intersect, at which points experimental halls house the detectors. Each beam consists of two 'bunches' of particles circulating 180^0 apart, with a bunch crossing occuring at each experiment every 3.84 μs. Typical bunch widths are $\sim$ 1mm in x (horizontally in the plane of PETRA), $\sim$ 0.1mm in y (vertically) and $\sim$ 10mm in z (along the beam direction). After many bunch crossings the beam currents become degraded as a result of e^+e^-interactions: a typical run during 1986 would start with currents of $\sim$ 10 mA, which reduced to $\sim$ 3 mA after about three hours, at which point the beams were dumped and PETRA was refilled. A fill typically required between 30 and 60 minutes. Apart from brief shutdown periods for maintenance, PETRA was run continuously between March and November 1986, when it ceased to operate as an e^+e^-storage ring, and is now being used as part of the pre-accelerator system for the HERA (Hadron-Elektron Ring Anlage) electron-proton collider project.

2.2.2 The Luminosity

The performance of a colliding beam machine is expressed in terms of the luminosity L delivered. For a process $e^+e^- \rightarrow$ X with cross section σ, the event rate dN/dt for luminosity L is given by:

$$dN/dt \quad = \quad L\,\sigma \tag{2.1}$$

and L can be expressed in terms of the collider parameters, *eg.* for Gaussian bunches:

$$L \quad = \quad \frac{n_+\,n_-\,f\,n_b}{4\pi\,\sigma_x\,\sigma_y}$$

where:

n_+ is the number of positrons per bunch

n_- is the number of electrons per bunch

f is the frequency of rotation

n_b is the number of bunches per beam

σ_x is the r.m.s. width of the bunch along the x axis

σ_y is the r.m.s. width of the bunch along the y axis

Since some of these quantities *eg.* σ_x, σ_y cannot be measured very accurately, each detector monitors L independently by counting the rate dN/dt of events whose cross section σ is known. This method has the additional advantages that fluctuations in the beam conditions at each intersection point are automatically taken into account, and that periods of 'dead time', when a detector was not operating even though there were colliding beams, do not contribute to the luminosity measurement. The process used is Bhabha scattering: $e^+e^- \rightarrow e^+e^-$, monitored at both small and wide angles to the beam pipe:

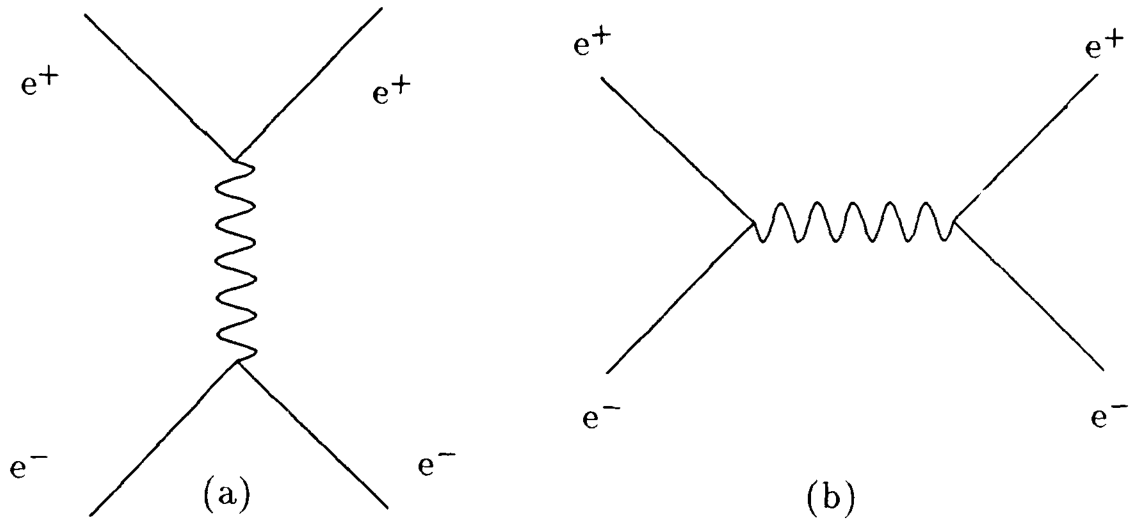

Figure 2.2: Lowest order diagrams for the Bhabha scattering process.

The forward Bhabha events involve low four-momentum transfers, *i.e.* small Q^2, where the t-channel photon exchange diagram (Fig. 2.2a) dominates and gives a high cross section. QED has been tested thoroughly in the low Q^2 region by many experiments, so that the QED calculation of the forward Bhabha cross section may be assumed to be accurate and used to determine the luminosity. Because of the high event rate the statistical errors are small, but the systematic uncertainty on the measurement using the small angle Bhabha events was typically $\pm(3.5 - 4.5)\%$ [75]. The rate of wide angle Bhabha events, where there is also a small contribution from the s-channel annihilation diagram (Fig. 2.2b), is much lower, so that the statistical error is larger. The luminosity determined independently from these events was in good agreement with that from the small angle events and had a total uncertainty of similar magnitude [75].

From equation 2.1 it can be seen that the dimensions of L are area^{-1} time^{-1}, normally expressed in $cm^{-2}s^{-1}$ or $nb^{-1}s^{-1}$, where 1 nb $= 10^{-37}$ m^2. Integrated over a period of time the luminosity is given in nb^{-1}. The luminosity measured by TASSO is shown as a function of the c.m. energy and time in Fig. 2.3. The machine luminosity was improved towards the end of 1980 by the installation of so-called mini-β quadrupole magnets near each interaction point to give better focusing of the beams. Between 1983 and 1985 PETRA ran at high beam energies around 22 GeV with the r.f. cavities being run at the limit of their power, causing a much lower luminosity, typically $\sim$150 nb^{-1} per day in 1985. During the 1985 winter shutdown half of these cavities were removed, and in the 1986 running at E_{beam} = 17.5 GeV the luminosity was considerably higher at around 500 nb^{-1} per day.

The last run was on 3^{rd} November 1986. Throughout its long life PETRA remained the world's highest energy e^+e^-collider; the peak c.m. energy of 46.8 GeV was achieved in 1984. To date this has been exceeded only by the TRISTAN collider at the KEK laboratory in Japan, which has produced e^+e^-annihilation events at c.m. energies up to 57 GeV [13].

2.3 THE TASSO DETECTOR

2.3.1 Introduction

TASSO was designed, built and run by an international collaboration of 13 institutes. Between 1979 and the end of 1986 at least 226 physicists worked on the experiment [76] and most are listed in Appendix A; in addition a large number of technical and support staff contributed to the construction and maintenance of the detector.

TASSO was designed to be a multi-purpose detector with particular emphasis on the detection and identification of charged particles. Sectional views of TASSO in the

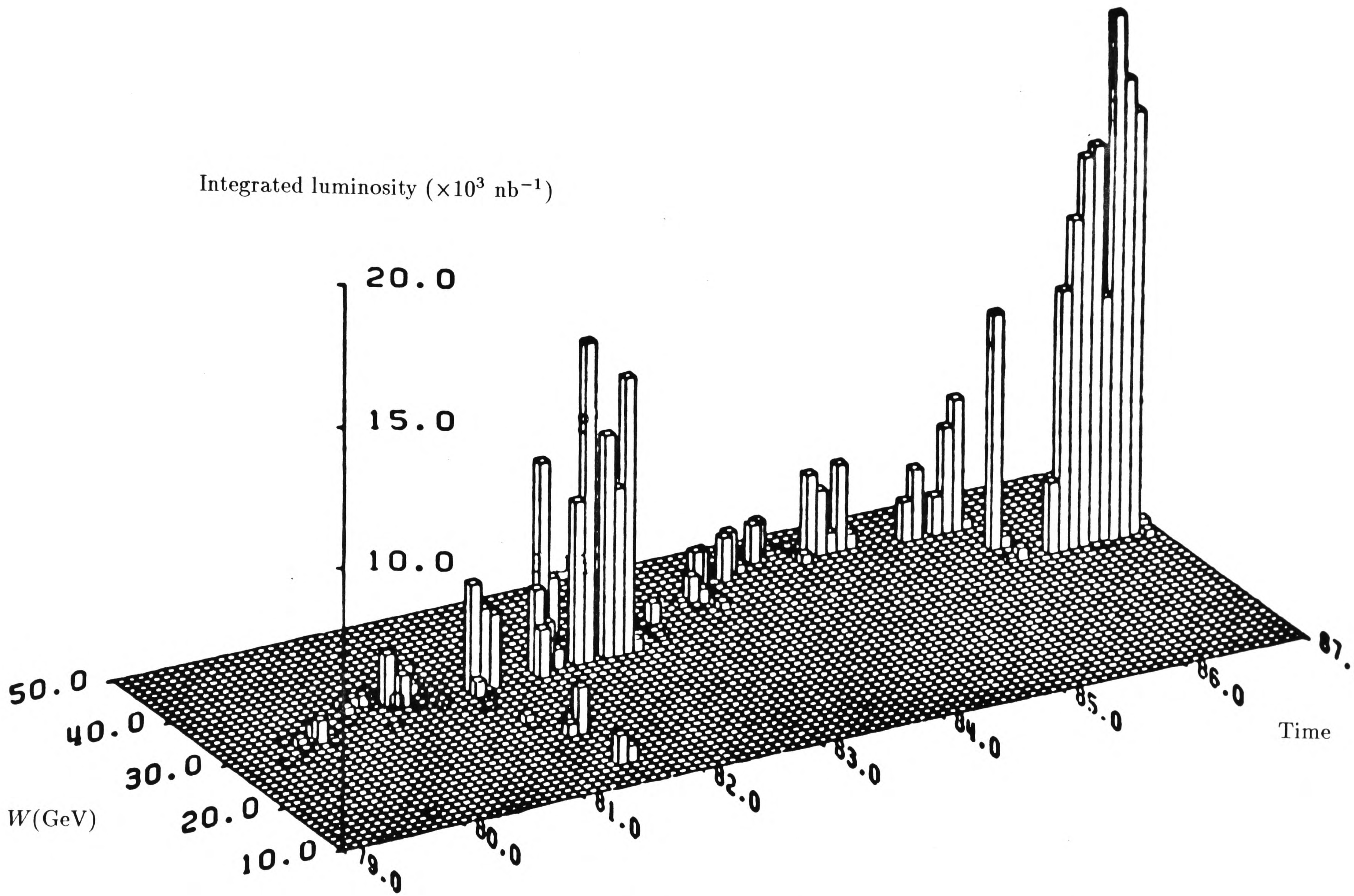

Figure 2.3: The integrated luminosity collected per month by the TASSO detector as a function of the c.m. energy and time of operation.

vertical plane containing the beam axis ($y-z$ plane), the vertical plane transverse to the beam axis ($x-y$ plane) and the horizontal plane containing the beam axis ($x-z$ plane) are shown in Figs. 2.4 a-c respectively. (The TASSO coordinate system is explained in Appendix B).

The central detector [77] comprises a set of tracking chambers used to measure the positions and momenta of charged particles. In order of increasing radius are a compact high precision drift chamber (vertex detector or VXD [78]), a central proportional chamber (CPC) [79], the main drift chamber (DC) [80] and the inner time of flight counters (ITOF) [81]. These lie within the aluminium solenoid coil of inner radius 135 cm and length 440 cm which produces a uniform magnetic field of 0.5 T parallel to the beam axis.

The external detector consists of the hadron arms, the barrel, yoke and the endcaps; these provide particle identification and calorimetry information.

The hadron arms [82] are situated along the x-axis on either side of the coil. Working away from the interaction point each contains a planar tube chamber (PTC) [83], a series of three threshold Čerenkov counters (aerogel, freon and carbon dioxide) [84], a time of flight system (HTOF) [85], a shower counter system (HASH) [86], iron shielding which acts as a muon filter and finally muon chambers [87].

Above and below the coil, forming the barrel, are the lead-liquid argon shower counters [88] used for electron and photon identification. Outside these the iron yoke acts both as a path for the return flux of the magnet and as a muon filter; the muon chambers themselves lie outside the yoke.

In each of the endcap regions are a time of flight system (ECTOF), liquid argon calorimeters (LAEC) [89], iron shielding and a pair of muon chambers. There is also a forward detector system [90] close to the beam pipe to measure particles at small forward and backward angles and a luminosity monitor for the small angle Bhabha events [90,91].

Those components of the central detector used extensively in this analysis are described in more detail below.

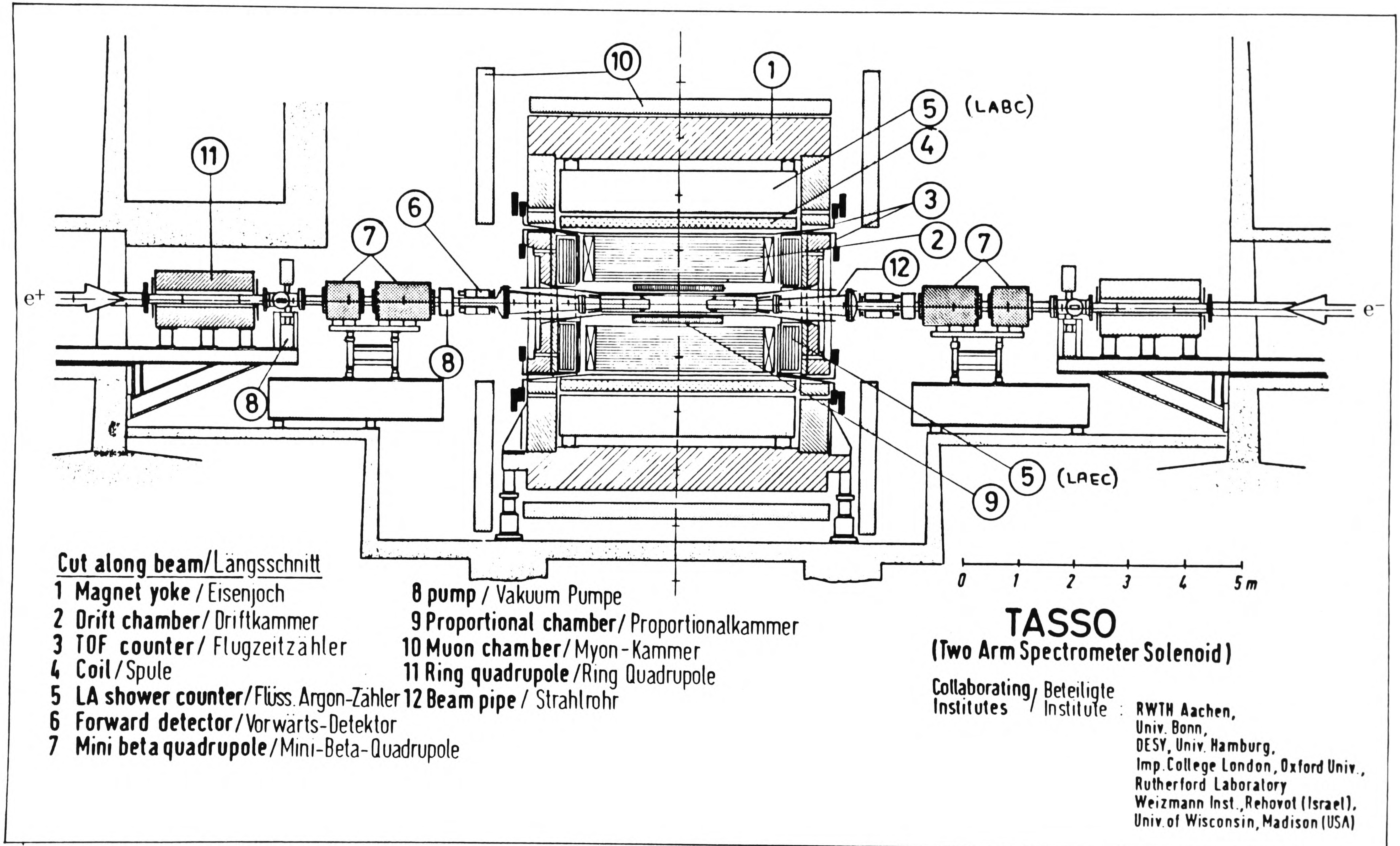

Figure 2.4(a): The TASSO detector - side view

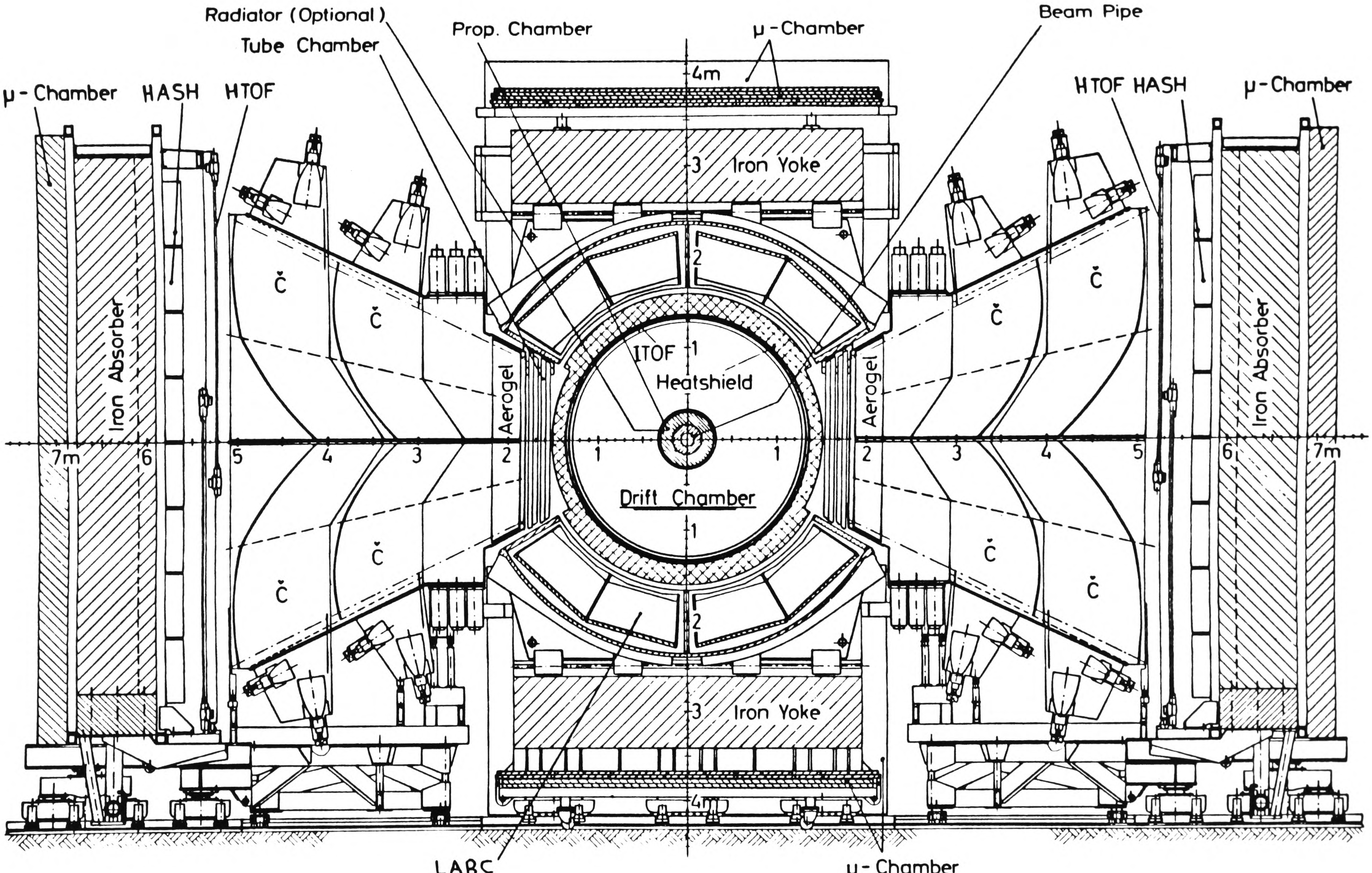

Figure 2.4(b): The TASSO detector - cross section perpendicular to the beam

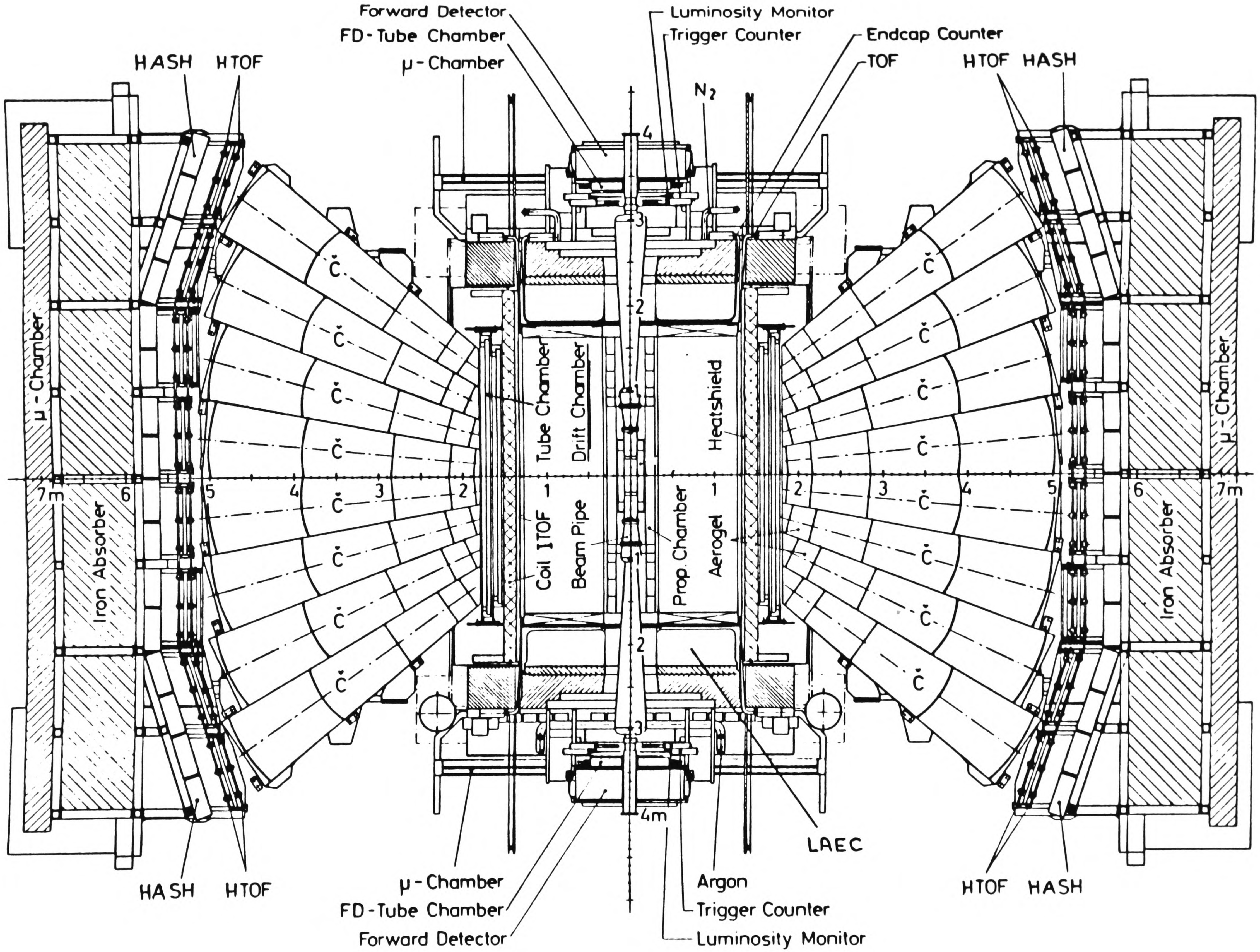

Figure 2.4(c): The TASSO detector - top view

2.3.2 The Central Proportional Chamber

The CPC [79] is a cylindrical multiwire proportional chamber used to provide a fast trigger for the experiment and for charged track reconstruction in the central detector. The chamber has an active length of 140 cm and inner and outer radii of 18.0 and 28.6 cm respectively, which corresponds to full coverage for polar angles θ with respect to the beam of $|\cos\theta| < 0.92$. It is filled with a gas mixture of roughly 75% argon, 25% isobutane and 0.25% freon. It has four cylindrical layers of active radial width 14 mm spaced 30 mm apart, each consisting of 480 anode wires parallel to the beam. Each anode layer lies between two sets of 120 helical cathode strips of average width 8 mm at a pitch angle of 36.5^0, but in opposite senses of rotation. The anodes can measure track reconstruction with a resolution of ~ 0.7 mm in the $r - \phi$ plane and the cathodes have a resolution along the z axis of ~ 3 mm.

2.3.3 The Central Drift Chamber

The DC [80] is a high precision wire chamber filled with a gas mixture of 50% argon and 50% ethane from which most of the charged particle tracking information is obtained. It has 15 cylindrical coaxial layers of drift cells, each containing a 30 μm tungsten sense wire and two sets of 120 μm molybdenum potential wires. Nine of the 15 layers are parallel to the beam (the 0^0 wires) and the other six (the α wires) are inclined at angles of $\pm 4.5^0$ to provide a measurement of the z coordinate along a track, enabling a full three-dimensional reconstruction to be made.

The chamber active length is 323 cm with inner and outer layer radii of 36.7 cm and 122.2 cm respectively, giving full coverage for $|\cos\theta| < 0.80$. The spatial resolution averaged over a drift cell is ~ 250 μm.

2.3.4 The Inner Time of Flight Counters

The ITOF counters [81] consist of 48 identical plastic scintillators arranged cylindrically around the DC at a radius of 132 cm, giving a polar angle coverage of $|\cos\theta| < 0.83$. Passage through the scintillator by a charged particle induces ionisation and hence the emission of light which is detected by photomultiplier tubes at each end of the counter.

The timing of this signal relative to the bunch crossing allows the particle velocity to be inferred. Combined with knowledge of the momentum, the particle mass and hence species can be derived. The timing resolution of the counters varies from roughly 0.35 ns at the ends to 0.5 ns at the centre. No such particle identification is used in this analysis, though the ITOFs form an important part of the experimental trigger and are used for rejecting cosmic ray events.

2.4 THE HADRONIC EVENT TRIGGERS

There are bunch crossings at PETRA every 3.84 μs, *i.e.* a rate of 2.6×10^5 Hz; in most of these crossings no measurable interactions occur. The purpose of a trigger is hence to recognise a particle event as it occurs so that the information from the detector can be read out and recorded. Here, a *bona fide* event means one of the type $e^+e^- \rightarrow e^+e^-$, $\mu^+\mu^-$, $\tau^+\tau^-$, hadrons, e^+e^-+ hadrons. In addition a trigger also serves as the first stage of the process of rejection of non-*bona fide* events arising from the following background sources:

(i) synchrotron radiation

(ii) beam gas events in which an electron or positron collides with a gas molecule in the beam pipe

(iii) beam pipe events involving collisions of an off-momentum particle with the wall of the vacuum pipe

(iv) cosmic ray events

(v) electronic noise in the detector

Such events do not necessarily originate from the interaction region ($z \sim 0$) but can occur anywhere in z; their rate is very large relative to that for the genuine events, so that the trigger rate is still dominated by the background. For example, in 1986 the trigger rate was typically between 1 and 10 Hz depending on the beam currents and PETRA operating conditions, though only about 100 hadronic events were collected per day, during which time the experiment was active for around 18 hours.

In practice there are different triggers for the different *bona fide* event processes.

Each individual trigger consists of logical combinations of several decisions based on signals from different parts of the detector. Interesting events are characterised by the multiplicity and topology of their charged tracks, energy deposits in the calorimeters and shower counters and by hits in the muon chambers. There are two triggers which are responsible for the detection and recording of hadronic events; both involve crude track-finding using information from the CPC, DC and ITOF to give so-called prepro tracks[1]. The first hadronic event trigger requires at least four or five prepro tracks to have been found, the latter number being used during the period of highest energy running, to suppress the backgrounds recorded in the central detector. The second trigger requires at least one pair of prepro tracks back-to-back to within about $\pm 27^0$. This is principally designed to detect Bhabha and $\mu^+\mu^-$ events, but can also pick up some low multiplicity hadronic events which are missed by the first trigger.

When an event satisfies a trigger condition the detector is read out and the data are buffered locally on disk[2] before being written to a so-called dump tape. The readout process takes about 40 ms, during which time the detector is insensitive and $\sim 10^4$ further beam crossings occur. In order to minimise such 'dead time' it is very important to choose the experimental trigger requirements to reject as many background events as possible, though without discarding genuine events.

2.5 DATA REDUCTION AND PROCESSING: SELECTION OF HADRONIC EVENTS

In selecting events of the type $e^+e^- \rightarrow$ hadrons from the many events which triggered the detector there are two classes of non-hadronic events which need to be removed by appropriate cuts: (a) the backgrounds described in Section 2.4 which do not involve interactions between an electron and a positron; (b) genuine e^+e^-events of the types:

(1) $e^+e^- \rightarrow e^+e^-$ (Bhabha scattering)

[1] For further details see [74].

[2] Until the end of 1984 the online computer was a Norsk Data NORD 10S, thereafter it was a Digital Equipment Corporation VAX 730.

(2) $e^+e^- \rightarrow \mu^+\mu^-$

(3) $e^+e^- \rightarrow \tau^+\tau^-$

(4) $e^+e^- \rightarrow e^+e^-\gamma\gamma$, $\gamma\gamma \rightarrow$ hadrons

The trigger requirements were designed to suppress the type (a) events, though a large number inevitably gets through, whilst allowing through the vast majority of the type (b) events.

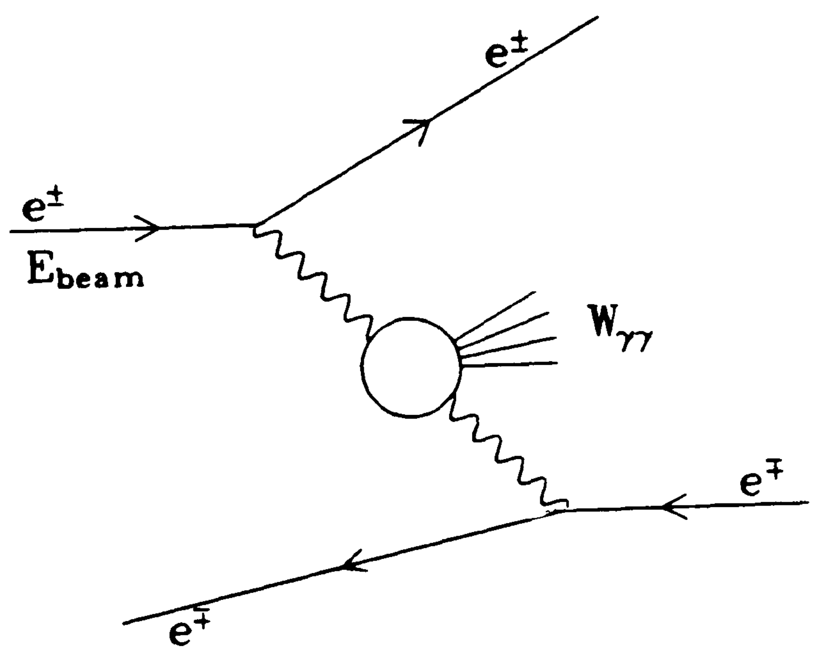

Figure 2.5: Representation of a two-photon interaction.

The normal hadronic events typically contain many charged tracks occupying a large fraction of the total solid angle, whereas the backgrounds have distinctively different topologies which make them easy to isolate in principle. As mentioned in Section 2.4, the type (a) events are z-independent; in addition, those events due to synchrotron radiation, beam gas and beam pipe interactions generally result in a single cone of many tracks, often originating close to or within the beam pipe wall. For type (b), Bhabha scattering (1) and muon pair (2) events generally have just two back-to-back tracks, each with roughly the beam momentum. However, photons radiated by either or both of the final state leptons in interactions with the detector material, which convert to e^+e^-pairs, give extra tracks which can fake low multiplicity hadronic events. Similarly $\tau^+\tau^-$ events (3) in which both particles decay into one charged track are easily distinguished from hadronic events. However, a sizeable fraction (13% [92]) of taus decay into three charged particles, so that many events have a distinctive 1-against-

3 or 3-against-3 track topology. Finally, in event type (4), virtual photons radiated by the incoming leptons (Fig. 2.5) interact to give hadrons and an e^+e^-pair in the final state. Because of the low four-momentum-transfer-squared, Q^2, involved, the electron and positron are usually deflected at small angles to the beam and are not measured in the central detector, whilst the hadronic system has low multiplicity and a small momentum sum.

There are four stages to the process of isolating the hadronic events from both types of background, known as PASS-1 to PASS-4.

2.5.1 PASS-1

The first stage of the data processing consists of running a preliminary fast track reconstruction program FOREST [93] on all events passing one of the triggers; this is done either online using the IBM emulators[1] or offline using the DESY IBM computer to analyse the dump tapes. FOREST uses a tree algorithm to reconstruct initially tracks in $r-\phi$ using hits in the DC 0^0 wires, assuming that the space-drift time relations are linear across the drift cells. If a track is found, hits from the α wires are used to fit in z. All detected events are thus processed and written onto the PASS-1 tapes. For the 110 pb^{-1} of data collected in 1986, 40 million triggers were written to 1650 PASS-1 tapes.

2.5.2 PASS-2

PASS-2 tapes are produced from PASS-1 tapes by applying sets of loose cuts to the events based on the topologies of the FOREST tracks and the energy deposits in the calorimeters. Each set of cuts is designed to remove a large fraction of the background to the events of interest, thereby reducing the number of events to be processed subsequently by the full track-finding program, and hence the computer time needed. The most important cuts for selecting hadronic events are:

(1) ≥ 2 tracks reconstructed in $r-\phi$

(2) ≥ 1 track reconstructed in three dimensions with[2] $|d_0| < 2.5$ cm and $|z_0| < 15.0$

[1] These were initially 168E and later 370E emulators [94].

[2] These track parameters are explained in Appendix B.

cm.

2.5.3 PASS-3

At this stage there is a pre-selection of events satisfying:

(1) ≥ 3 tracks reconstructed in $r - \phi$ with $|d_0| < 2.5$ cm

(2) ≥ 2 tracks reconstructed in three dimensions with $|d_0| < 2.5$ cm and $|z_0| < 15.0$ cm

These events are then run through the MILL track-finding program, which uses a road algorithm taking the FOREST tracks as a first iteration, and then attempts to find new tracks using the remaining unassociated DC hits. Again, tracks are first reconstructed in the $r - \phi$ plane and then if successful in the z direction also. Corrections for non-linearity of the space-drift time relations and the entrance angles of tracks to drift cells are applied, and CPC anode hits are also included in the fit. The r.m.s. transverse momentum resolution, including multiple scattering, for the MILL tracks was [16]:

$$\frac{\sigma_p}{p_t} = 0.016\,(1 + p_t^2)^{1/2} \qquad (p_t \text{ in GeV}/c)$$

The angular two-track resolution was typically $\sigma_\phi = 4$ mrad in azimuth and $\sigma_\theta = 6$ mrad in polar angle. MILL is a more efficient and precise track-finder than FOREST, but requires a factor of roughly 10 times more computer processing time per hadronic event. The MILLed events are written to the PASS-3 tapes and the FOREST tracks are not used further.

2.5.4 PASS-4

This stage comprises the final hadronic selection. Firstly, every track in a PASS-3 event is required to satisfy the TRKSEL (TRacK SELection) cuts:

(1) Reconstruction in three dimensions

(2) $\chi^2_{r\phi}$ per d.o.f. < 10.0 for the $r - \phi$ track fit

(3) $|d_0| < 5.0$ cm

(4) transverse momentum $p_{xy} > 0.1$ GeV/c

(5) $|\cos\theta| < 0.87$

(6) $|z_0 - \bar{z}_0| < 20.0$ cm, where $\bar{z}_0$ is the average z_0 of all the tracks in the event passing cuts (1)-(5).

The HADSEL (HADronic SELection) cuts are then applied considering only those tracks passing TRKSEL:

(1) ≥ 4 tracks for $W \leq 26.0$ GeV.

≥ 5 tracks for $W \geq 26.0$ GeV.

(2) The event is divided into two hemispheres by the plane perpendicular to the sphericity axis (see Section 3.2). For events containing just 1 against 3 tracks and $W \leq 26.0$ GeV, the invariant mass m_3 of the 3-track system must satisfy $m_3 > m_\tau$, the tau mass, where each track is assumed to have the charged pion mass.
For events containing just 3 against 3 tracks and $W > 16.0$ GeV, $m_3 > m_\tau$ for both 3-track systems.

(3) $|\bar{z}_0| < 6.0$ cm

(4) $|\Sigma_i\, Q_i| < 4$ for $W < 16.0$ GeV, where Q_i is the charge of track i.

(5) At least one track in both the forward and backward hemispheres for $W < 16.0$ GeV.

(6) $\Sigma_i |p_i| > 0.265\, W/c$

These cuts discriminate against beam gas scattering (3 to 6), $\tau^+\tau^-$ production (1,2), Bhabha scattering and muon pair production (1) and $\gamma\gamma$ scattering (1,6).

Until 1985 all events satisfying the above criteria were visually scanned to remove any remaining backgrounds. From 1985 onwards a computer program was used to make a pre-selection of 'dubious' events, and only these were subsequently scanned. Events assigned as type (a) 'fakes' were discarded, as were type (b) Bhabha and muon pair events; however, no attempt was made to discard tau pair or $\gamma\gamma$ events*. Roughly 3% of all events were rejected [16], most of them being Bhabha events producing electromagnetic showers in the material before the tracking chambers.

All events surviving the HADSEL and scanning procedures were written to the

* These are considered in Section 3.4.

PASS-4 tapes and comprise the final hadronic sample; for the 1986 running roughly one hadronic event was found for every 10^3 triggers. The numbers of PASS-4 events are shown as a function of beam energy in Table 2.1.

Table 2.1: Number of events as a function of beam energy

Beam energy	1978-84	1985	1986
6-7	258		
7-8	2704		
8-9	37		
9-10			
10-11	1584		
11-12	330		
12-13	231		
13-14	139		
14-15	146		
15-16	726		
16-17	3896		
17-18	17252	172	31175
18-19	336	1	1
19-20	155	2084	
20-21	646		
21-22	779	1934	
22-23	2434		
23-24	415		

2.6 SIMULATION OF THE DETECTOR

The end-product of the TASSO data reduction scheme is a set of events, each containing a number of reconstructed tracks representing the passage of charged particles through the detector. For any given event, the tracks which are measured usually represent closely the actual particles, but not exactly so. First, neutral particles do not produce any tracks at all. In addition, because of inefficiencies in the wires and electronics of the tracking chambers and in the track-finding, it is possible that a charged particle may not be measured as a track. Conversely, if there are noise hits in the chambers, completely spurious tracks may be reconstructed from these and unassigned genuine hits, which do not correspond to any real particles. Even when a particle does produce a measured track, the momentum determined from the curvature will be smeared from the 'true' value because of the finite resolution of the tracking chambers and bias introduced by the track-finding algorithm. Furthermore, the 'true' particles can interact with the detector material and be scattered or produce new particles, or can decay within the detector.

Hence, in order to reconstruct the 'true' particle events from the measured tracks, careful unfolding is necessary, taking all of the previous effects into account. Clearly such unfolding cannot be done for individual events, but only on a statistically averaged basis for samples of many events. For this purpose it is useful to have a computer program which simulates all of these detector effects: Monte Carlo generated events using, for example, one of the models described in Chapter 1, can be fed into the simulation program to produce hits corresponding to those in the real chambers. The same track-finding programs and selection cuts as for the real data can then be applied, and the final processed events compared with the initially generated sample to study how the detector has distorted the 'true' events. From these Monte Carlo datasets, correction factors for all the simulated detector effects can be determined and applied to the real data.

In this analysis the computer program used was SIMPLE (SIMulation Program for Large e^+e^- Experiments [95], which allows simulation of many events in reasonable computer time. SIMPLE takes events generated by a supplied perturbative QCD + fragmentation model, allowing for photon radiation by an electron or positron in the initial state [96] and electroweak effects, and traces the particles through a simulation of the TASSO inner detector, including scattering, interactions, decays and photon conversions. These effects are parametrised from observed events in TASSO. Charged particles give hits in the CPC and DC which are then smeared by the measured resolution and efficiency. The smeared hits associated with each charged particle are fitted in three dimensions to give the measured track. A hit-dependent track-finding efficiency, determined from real MILLed events, is used, so that not all charged particles produce a track. Noise and crosstalk hits can be generated, but are not used to give spurious tracks as there is no routine associating combinations of hits into tracks; only genuine hits produced by a particle are used for that track fit.

The various parametrisations and approximations mean that SIMPLE is fast in terms of computer processing time per event. The simulation, however, remains an approximate one, so that for detailed studies it is necessary to MILL the SIMPLE events so that they can be properly compared with the real data. This is discussed further in Chapter 3.

CHAPTER 3

INCLUSIVE STUDIES OF THE HADRONIC FINAL STATE AT W = 35 GeV

3.1 INTRODUCTION

In the last 10 years a wealth of information has been collected at PETRA and PEP on hadron production in high energy e^+e^- annihilation. Many studies of the properties of hadronic final states have been performed [16,43,97,98,99,100] and comparisons made with perturbative QCD + fragmentation models [55,57,72,101]. In this chapter the distributions of physical quantities obtained from the 1986 TASSO hadronic data at $W =$ 35 GeV are compared with the predictions of the latest generation of QCD fragmentation models described in Chapter 1. The 35 GeV data sample was used because it comprises the largest number of events collected by TASSO at a single energy, under the excellent low noise conditions of the 1986 PETRA running.

The most important of the arbitrary parameters of the models were first optimised to provide a good description of a few relevant quantities, and then the models were tested more globally in terms of many observables. The important observables in global studies of hadronic final states are defined in Section 3.2. The event selection cuts, background to the data sample, parameter tuning and data correction procedures are described in Sections 3.3-3.7. The results of the comparison between models and data at $W = 35$ GeV are given in Sections 3.8 and 3.9; the energy evolution across the PETRA range and the model predictions up to $W = 200$ GeV are shown in the next chapter and the study of multijet rates is presented in Chapter 5.

3.2 DEFINITION OF OBSERVABLES

Both global event shape observables and single track inclusive distributions are studied, using charged particles only. Event shapes may be characterised by using the sphericity tensor [102]:

$$T_{\alpha\beta} = \frac{\sum_{j=1}^{N} p_{j\alpha} p_{j\beta}}{\sum_{j=1}^{N} \mid \mathbf{p_j} \mid^2}$$

where the sums are over the N particles in the event. The eigenvalues of this tensor, Q_1, Q_2, Q_3, are ordered such that $Q_3 > Q_2 > Q_1$ and satisfy $Q_1 + Q_2 + Q_3 = 1$. The event axis is taken to be the sphericity axis, the eigenvector corresponding to Q_3, and the event plane is that defined by the eigenvectors corresponding to Q_3 and Q_2. The variables aplanarity

$$A = 3/2 Q_1 \qquad 0 \leq A \leq 1/2$$

and sphericity

$$S = 3/2(Q_1 + Q_2) \qquad 0 \leq S \leq 1$$

are commonly used to characterise events. Extreme two-jet events have $S = 0$, whilst $S \to 1$ for spherical events. Extreme planar events have $A = 0$. Closely related event observables are:

$$< p^2_{T_{in}} > \; = \; < p^2 > Q_2 \qquad \text{and} \qquad < p^2_{T_{out}} > \; = \; < p^2 > Q_1$$

where $p_{T_{in}}$ and $p_{T_{out}}$ are the particle momentum components transverse to the sphericity axis in and out of the event plane respectively, and the average is over all particles in the event.

The particle momenta enter quadratically into the sphericity tensor, so that the sphericity axis is more sensitive to high momentum tracks than, for example, the thrust axis, where the thrust T is defined [31]:

$$T = \frac{\mathrm{Max} \sum_{j=1}^{N} \mid p_{\parallel j} \mid}{\sum_{j=1}^{N} \mid \mathbf{p_j} \mid} \qquad 1/2 \leq T \leq 1$$

which is linear in particle momenta, and hence infra-red safe, the axis being chosen to maximise $\sum \mid p_{\parallel j} \mid$. Extreme two-jet events have $T = 1$. Particle rapidity is defined

$$y = \frac{1}{2}\ln\left(\frac{E+p_{\parallel}}{E-p_{\parallel}}\right)$$

with respect to the thrust axis. A commonly used fragmentation variable is the scaled track momentum $x_p = 2 \mid \mathbf{p} \mid /\sqrt{s}$, useful because no knowledge of particle species and hence masses is required.

The scaled invariant mass-squared of the two hemispheres in the event, M_h^2/s, M_l^2/s [103], are well-behaved quantities in perturbative calculations. Here the event is divided into hemispheres by the plane perpendicular to the sphericity axis and 'h' denotes the hemisphere with the greater mass, 'l' that with the lower mass. Because only charged particles are used in this analysis we divide the mass-squared by the *visible* energy-squared, E_{vis}^2, rather than by s, where E_{vis} is the energy sum of the particles measured in the tracking chambers assuming they all have the pion mass.

3.3 EVENT SELECTION CUTS

For the comparison between models and data described in Sections 3.8 and 3.9 additional cuts were applied to the data. To ensure a large acceptance for the particles in jets, only events with $\mid \cos\theta_{jet} \mid < 0.7$ were considered, where θ_{jet} is the angle between the sphericity axis and the beam axis. Events with a hard photon in the initial state were suppressed by requiring $\mid \cos\theta_n \mid > 0.2$, where θ_n is the angle between the normal to the event plane and the beam direction. From the initial sample of 31176 events, 18849 survived these cuts and were used in the subsequent analysis.

3.4 BACKGROUNDS TO THE DATA SAMPLE

It is necessary to estimate the contamination to the PASS-4 data sample arising from background events which pass the cuts described in Section 2.5. Bhabha events can enter the hadronic sample only if they generate extra tracks, *eg.* through the conversion of radiated photons or interactions in the detector material. The residual contamination from this source was estimated to be negligible [104] as such events are generally easily identified in the visual scan. z-independent and fake events (Section 2.4) are similarly easily identified and removed in the scan and any remaining contribution was negligible [16,55,104,105].

3.4.1 The Two-photon Background

At $W = 35$ GeV the total cross section, $\sigma_{\gamma\gamma}$, for events of the type $e^+e^-\gamma\gamma \rightarrow e^+e^- +$ hadrons is enormous (see eg. [106]) compared to the cross section σ_{had} for annihilation events: $e^+e^- \rightarrow$ hadrons. In the vast majority of such events the particles in the hadronic system have such low momentum transverse to the beam direction that they remain undetected in the beam pipe, *viz* the invariant mass of the hadronic system, $W_{\gamma\gamma}$, is small. The event invariant mass distribution of the 1986 PASS-4 data showed that virtually no events have masses less than 5 GeV [107]. Hence only those two-photon events with $W_{\gamma\gamma} \geq 5$ GeV are likely to be confused with annihilation events, provided they pass the HADSEL cuts, the most relevant being that the events contain ≥ 5 charged tracks and have momentum sums $> 0.265\, p_{beam}$. Even though such high $W_{\gamma\gamma}$ events are suppressed by a factor $1/W_{\gamma\gamma}$ in the cross section, it is shown below that $\sigma_{\gamma\gamma}(W_{\gamma\gamma} > 5)$ is comparable to σ_{had} at $W = 35$ GeV.

Because of their light masses, open production of particles containing u,d,s quarks in two-photon events is expected and has been observed [106]. Charmed particle production should be strongly suppressed as $W_{\gamma\gamma} > 3.1$ GeV is required, but has also been seen [106,108]; as yet there is no evidence for two-photon production of particles containing b quarks at e^+e^-energies studied to date. Neglecting threshold factors and assuming the quark flavours are produced according to the fourth power of their charges [106]:

$$\sigma_{\gamma\gamma}(W_{\gamma\gamma}) \quad = \quad \sigma_0(W_{\gamma\gamma}) \sum_{i=u,d,s,c} q_i^4$$

For production of u quarks only, $\sigma_{\gamma\gamma}(W_{\gamma\gamma} > 5) = 0.152$ nb [109]. Hence for production of all four flavours, $\sigma_{\gamma\gamma}(W_{\gamma\gamma} > 5) = 323$ pb.

By comparison, the annihilation hadronic cross section is given by (Section 1.1):

$$\sigma_{had} = \frac{86.9}{s} \times 1000 \times R \text{ pb}$$

At $s = W^2 = (35 \text{ GeV})^2$, taking $R = 3.90 \pm 0.05$ from a recent determination [10], $\sigma_{had} = 276$ pb. Hence the cross section for detectable two-photon hadronic events is comparable to that for annihilation hadronic events.

The contamination of $\gamma\gamma$ events in the PASS-4 sample was then estimated using a Monte Carlo simulation with the event generator of [109], requiring $W_{\gamma\gamma} > 5$ GeV, incorporating hadronisation according to a Field-Feynman scheme [110]. A large sample of n_{gen} events was generated with initial state radiative effects [96] and full SIMPLE detector simulation. After MILLing and applying TRKSEL and HADSEL cuts, n_{acc} accepted events remained. The acceptance for the $\gamma\gamma$ events was hence n_{acc}/n_{gen} and is given in Table 3.1. From this acceptance and the ratio of $\gamma\gamma$ and annihilation cross sections, the fraction of expected events in the PASS-4 sample was calculated (Table 3.1) to be about 0.9%, in good agreement with previous estimates [16,55]*.

3.4.2 The Tau Pair Background

Events of the type $e^+e^- \rightarrow \tau^+\tau^- \rightarrow$ hadrons can pass the HADSEL cut $m_3 > m_\tau$ through momentum smearing. In addition, extra tracks can be generated through radiated photon conversions or interactions such that the event is no longer of the 3-3 or 1-3 topology and the mass cut is not applied.

The background of τ events in the PASS-4 sample was estimated in the same way as for the two-photon events, using the event generator of [111], with the branching ratios for the τ decay modes in agreement [92] with the most up to date values [112].

* Note that the background to the 1986 data is not *a priori* expected to be the same as to the old TASSO data at $< W > \sim 34$ GeV, as the material between the interaction point and the Drift Chamber changed due to the installation of the new beryllium beam pipe and VXD at the end of 1982.

Roughly 87% of the decays were in the 1-prong mode, with about 13% giving 3-prongs. Taking $\sigma_{\tau^+\tau^-} = 91.4$ pb [92] gives the results shown in Table 3.1, with a percentage contamination of about 0.7%, again in good agreement with previous estimates [16,55].

Table 3.1: Estimate of background to the PASS-4 data

$\sqrt{s} = 35$ GeV	$\tau^+\tau^- \to$ hadrons	$\gamma\gamma \to$ hadrons
σ(pb)	91.4	323
Acceptance (%)	2.2 ± 0.1	0.78 ± 0.07
N^0 of events in PASS-4	224 ± 8	284 ± 30
Background (%)	0.72 ± 0.03	0.91 ± 0.10
Background after event cuts 3.3 (%)	0.35 ± 0.02	0.35 ± 0.05

The errors are statistical only. Systematic errors are difficult to estimate because of the visual scanning of roughly 10% of the events; it is possible that some $\gamma\gamma$ or $\tau^+\tau^-$ events were mistakenly discarded as Bhabha events. The above numbers can therefore be regarded as realistic upper limits on the background.

Whilst the overall percentage contamination is small, some bins in certain distributions are particularly sensitive to background. For example, the first few bins of the charged multiplicity distribution are estimated to contain a large proportion of $\gamma\gamma$ and τ events which are typically of low multiplicity, whilst the latter, having in general a few very energetic tracks, also populate bins of high x_p. The n_{ch} and x_p distributions for the 1986 PASS-4 data are shown in Fig. 3.1, together with the estimated background from $\tau^+\tau^-$ and $\gamma\gamma$ events. Around 25% of the content of the $n_{ch} = 5$ bin, and $\sim 5\%$ of the $0.7 \leq x_p \leq 1.0$ bin, is due to such contamination. To take this into account, the properly normalised background was statistically subtracted from each data distribution on a bin-by-bin basis.

3.5 CORRECTIONS FOR MILL TRACK-FINDING

The tuning procedure to be described in Section 3.6 involves generating large numbers of hadronic events with full SIMPLE detector simulation. The real data, however, at the

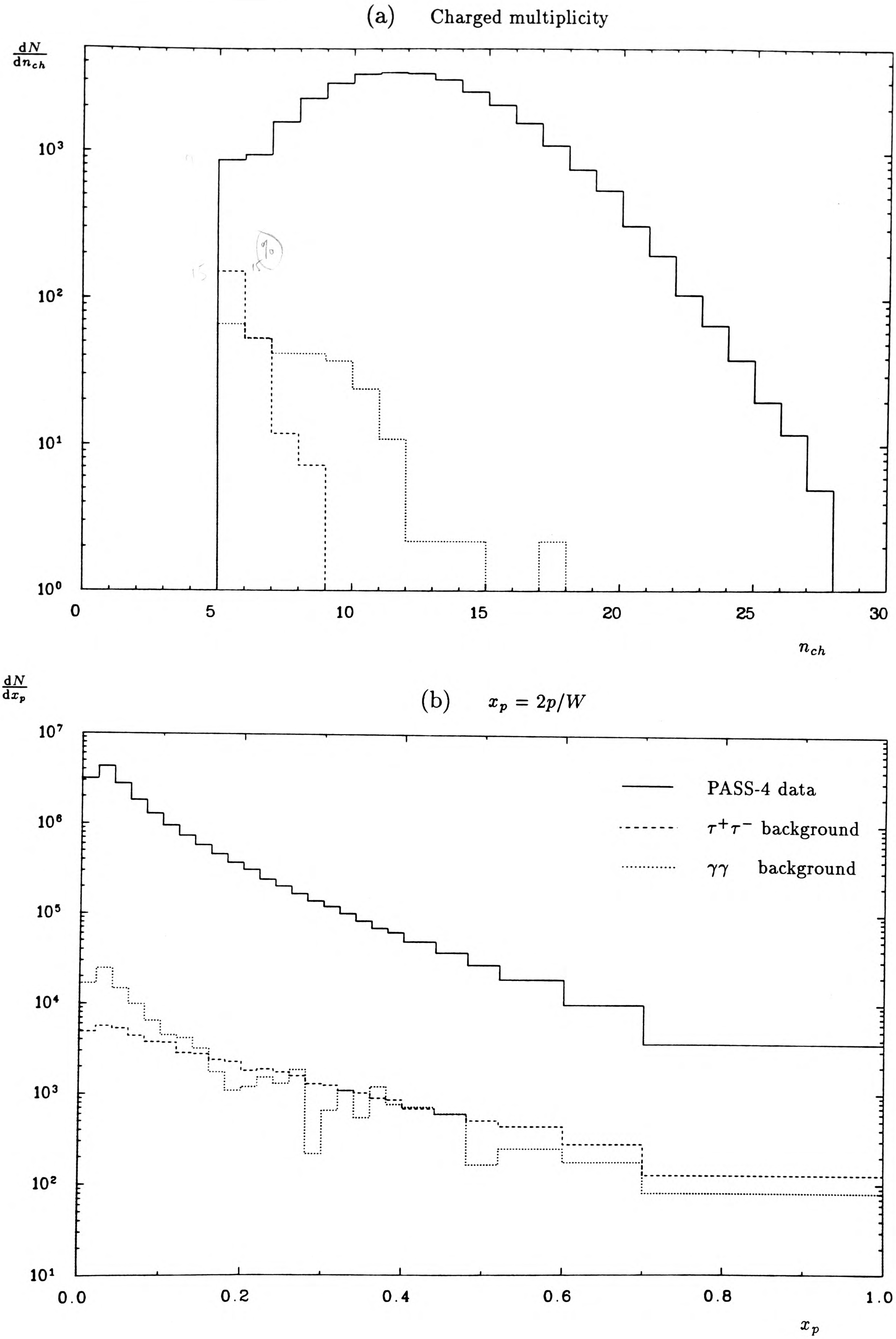

Figure 3.1: Background contributions to the PASS-4 data sample

PASS-4 stage have had the MILL track-finder applied. The SIMPLE track simulation involves the generation of spurious hits due to crosstalk and noise in the central tracking chamber, though the hits associated with a given generated track remain uniquely assigned to that track. In applying the MILL track-finder to the real data, there is the chance that hits in the chamber can be misassociated to the (*a priori* unknown) 'real' tracks, or that spurious tracks can be reconstructed from the many 'real' (*i.e.* genuine track-associated) and noise hits in the chamber. In particular, MILL occasionally finds [55] spurious, very straight tracks of high momentum (sometimes larger than the beam energy) from a set of hits with no apparent connection but which together have satisfied the necessary track formation criteria. Events containing such tracks will clearly be heavily biased, the sphericity and thrust axes being shifted towards the very energetic track.

In order to make a valid comparison between the real data and MC events with SIMPLE detector simulation one should therefore apply the MILL track-finder to the SIMPLE events. The only difficulty is a practical one in that MILL, like most complicated track-finders, requires a great deal of computer processing time, typically around 4.5s (DESY IBM cpu units) per event, compared with 0.5s per event for the full SIMPLE simulation, for hadronic events at W = 35 GeV *. Event generation, detector simulation and track-finding hence require about 5s total cpu per MC event so that it is impractical to MILL all of the MC datasets to be discussed below. In order to avoid introducing biases, the real data were hence corrected for the MILL effects so that they could be compared with the MC events at the SIMPLE stage.

A large sample of events was generated using a tuned version [113] of the $O(\alpha_s{}^2)$ generator in JETSET 6.2, with initial state radiative effects included [96], and passed through the SIMPLE detector simulation program. After the events were MILLed and TRKSEL and HADSEL cuts were applied, distributions of physical quantities were produced from the sample of accepted events. Table 3.2 shows the numbers of accepted tracks per event, before and after MILLing, in bins of x_p. (The errors are statistical only). MILLing accepted SIMPLE events picks up an extra ~30% of tracks in the range

* The precise time depends upon the event generator used and the c.m. energy, but the ratio of times is roughly 10:1 for MILLing:SIMPLE detector simulation.

$0.7 < x_p < 1.0$ and about 0.02 tracks per event with momentum larger than the beam momentum.

Table 3.2: Numbers of MC tracks per event

x_p	SIMPLE	MILLed SIMPLE
0.0 - 0.1	8.08 ± 0.03	8.16 ± 0.03
0.1 - 0.2	1.90 ± 0.01	1.97 ± 0.01
0.2 - 0.3	0.675 ± 0.008	0.679 ± 0.008
0.3 - 0.4	0.291 ± 0.006	0.287 ± 0.006
0.4 - 0.5	0.129 ± 0.004	0.128 ± 0.004
0.5 - 0.7	0.092 ± 0.003	0.096 ± 0.003
0.7 - 1.0	0.027 ± 0.002	0.034 ± 0.002
1.0 - ∞	0.003 ± 0.003	0.023 ± 0.003
0.0 - 1.0	11.20 ± 0.03	11.38 ± 0.03

For each distribution of a quantity x, a correction factor was determined for every bin i:

$$f_{x_i} = \frac{n^S_{x_i}}{n^{MS}_{x_i}}$$

where $n^S_{x_i}$ denotes the contents of the bin for the SIMPLE tracks and $n^{MS}_{x_i}$ for the MILLed SIMPLE tracks. The (background subtracted) data distributions were then multiplied by these factors:

$$n^{\mathrm{data}\,\prime}_{x_i} = f_{x_i} \times n^{\mathrm{data}}_{x_i}$$

The majority of the correction factors were close to unity, though for a few bins they may have been as low as 0.7 or as high as 1.4. For these purposes it was assumed that the correction factors were roughly independent of the event generator; this is certainly not true but is a good approximation to first order (see Section 3.7). Systematic errors on the MILL-corrected data were thus not considered at this stage, as any such errors were likely to be smaller than the statistical fluctuations arising from the samples of roughly 5000 MC events considered in the next section.

3.6 MODEL PARAMETER TUNING

3.6.1 The Tuning Approach

As mentioned in Chapter 1, the perturbative QCD + fragmentation models each include several arbitrary parameters which are loosely constrained to lie within certain ranges by theoretical considerations, but whose value may be varied within these bounds with considerable effect upon the resulting hadronic final state. In looking at the predictions of the models it is therefore necessary to choose somehow a particular set of parameters. The method of approach here is to consider for each model those few parameters whose variation has the greatest impact upon the hadronic final state and then to vary their values simultaneously within reasonable ranges to find that combination of values which optimises the description of some chosen observables.

One option is to optimise each model to give a good global description of many or all of the observables mentioned in Section 3.2. There are, however, several disadvantages to this procedure. Many of the observables are strongly correlated with one another; indeed almost every quantity is correlated with every other to a greater or lesser extent, so that tuning a few parameters to describe all observables is not really necessary. Furthermore, the more quantities which are tuned to, the less likely it is that each individual one will be very well described, each observable exerting its own influence on the tuning. For example, quantity X may choose an optimum value p_X of parameter p, whilst Y prefers a different value p_Y; optimising to X and Y simultaneously will give some value of p intermediate between p_X and p_Y; a reasonable description of both X and Y is thus obtained, at the expense of a very good description of either alone. Having optimised the model to many things it is then also difficult, because of correlations, to find other independent quantities against which to test it.

Instead the scheme adopted here is to choose a small set of relatively uncorrelated distributions of both event and single track observables, which are especially sensitive to the parameters to be optimised, namely:

(1) Sphericity, S

(2) Particle momentum transverse to the event plane, $p_{T_{out}}$

(3) Particle momentum fraction, x_p

(4) Particle multiplicity per event n_{ch}

where only charged particles are used. This set contains two event and two track variables. S is dominated by properties in the event plane ($Q_2 >> Q_1$) and is hence roughly orthogonal to $p_{T_{out}}$. The former is sensitive to hard gluon radiation in the event plane whilst the latter is sensitive to softer gluons and p_T arising from the hadronisation process. x_p is sensitive to the longitudinal fragmentation of jets, as is the event multiplicity n_{ch}. These distributions are hence suitable for determining optimum values of the parameters for both the perturbative QCD processes (Λ, Q_0) and the hadronisation (M_c, a, b, σ).

3.6.2 The Tuning Method

The tuning method is similar to that described in a previous TASSO publication [43]. For each model, n_g values of each of the n_p parameters were used to define a grid in a parameter space of dimension n_p. For each of the $n_g^{n_p}$ points in the grid, 7000 Monte Carlo events were generated with QED radiative corrections and put through the SIMPLE detector simulation program and hadronic event selection procedures, giving roughly 5000 events remaining. Distributions of the observables, normalised per event, were produced for each MC dataset and also for the background-subtracted, MILL-corrected TASSO data. For each bin of each distribution to be fitted, for every MC dataset the χ^2 was calculated between the MC and the same bin for the data. A second order polynomial in the n_p tuning parameters was then fitted to the $n_g^{n_p}$ χ^2's for that bin. The sum of the polynomials, over all bins in all distributions, was then minimised using the program MINUIT [114] to obtain the tuned values of the parameters.

The topography of the χ^2 space was examined by looking at the variation of χ^2 with the value of each parameter across its tuning range to ensure that a true global minimum, and not some local fluctuation, had been found by MINUIT.

An important point to note is that by this procedure the models (after detector simulation *etc.*) were compared with the essentially 'raw' TASSO data (after background subtraction). An alternative approach would have been to tune the models directly to the fully-corrected data, where the correction factors (see Section 3.7) were themselves determined from MC studies using the models. The former procedure is clearly less prone to possible biasing of the model tuning results than the latter.

3.6.3 Tuned Parameter Values

The tuned parameters are shown in Table 3.3, together with the default values and the values obtained by Mark II [72] for comparison. Any one parameter may be varied by $\sim \pm 10\%$ from the optimum value with minimal effect on the description of the data. However, for the Lund cascade model (Table 3.3c) it was found that a, b could be varied simultaneously across a wide range so as to preserve the agreement with the data in terms of the n_{ch} distribution and were only strongly constrained by the fit to x_p (see Section 3.8). This degree of freedom in a, b was much less evident for the Lund O(α_s^2) model (Table 3.3a), a reflection of the greater influence of the string fragmentation on the hadronic final state for the matrix element generator as compared with the cascade.

Table 3.3a: Parameters for the Lund O(α_s^2) model

Parameter	Default	Tuning Range	Tuned Value	Mark II
QCD scale in O(α_s^2) $\Lambda_{\overline{MS}}$ (GeV)	0.50	0.2 - 1.1	0.62	0.50
Parton pair resolution parameter y_{min}	0.02	Fixed	0.02	0.015
Fragmentation function parameter a	1.0	0.1 - 1.0	0.58	0.9
Fragmentation function parameter b	0.7	0.2 - 1.1	0.41	0.7
Gaussian p_T parameter $\sqrt{2}\sigma$ (GeV/c)	0.40	Fixed*	0.40	0.33

* in previous analyses [55,113] this parameter was found to be well-constrained by the data

Table 3.3b: Parameters for the Webber cascade model

Parameter	Default	Tuning Range	Tuned Value	Mark II
QCD LLA scale Λ_{LL} (GeV)	0.35	0.1 - 0.5	0.25	0.20
Cascade virtuality cutoff Q_0 (GeV)	0.75	0.6 - 2.0	0.61	0.75
Cluster-mass parameter M_c (GeV/c^2)	3.75	2.0 - 4.0	2.3	3.0

Table 3.3c: Parameters for the Lund cascade model

Parameter	Default	Tuning Range	Tuned Value	Mark II
QCD LLA scale Λ_{LL} (GeV)	0.40	0.15 - 1.2	0.26	0.40
Cascade virtuality cutoff Q_0 (GeV)*	1.0	0.5 - 2.0	1.0	1.0
Fragmentation function parameter a	0.50	0.1 - 1.0	0.18	0.45
Fragmentation function parameter b	0.90	0.1 - 1.0	0.34	0.90
Gaussian p_T parameter $\sqrt{2}\sigma$ (GeV/c)	0.35	0.33 - 0.42	0.39	0.33

* this parameter was not tuned simultaneously with the others, but was varied in the range shown after the optimum values of Λ_{LL}, a, b and σ had been found.

Probably because of this $a-b$ correlation, the Mark II optimum values for the Lund models are somewhat different than those obtained here, and they also obtain a good description of their data at 29 GeV. This allows a thorough and rigorous testing of the QCD models, in that they can only be fairly judged and compared after exploration of the range of their predictions arising from reasonable variations of their arbitrary parameters.

3.6.4 Comparison with the $D^{*\pm}$ Fragmentation Function

One important feature of the Lund string model is that the same fragmentation function (equation 1.7) is used for all primary quark flavours*. In practice many of the final state hadrons do not come directly from the fragmentation of the colour string, but rather

* Within this model the parameter b should be universal, though this is not the case for a, which in principle could take different values for different flavours but is assumed to be universal.

from the decay of resonances or heavy particles which were themselves produced in the string break up. One therefore does not expect the function in equation 1.7 to describe directly the final state particle momentum spectrum. However, a direct test of this function is available in the form of the momentum spectrum of primary $D^{*\pm}$ mesons produced in e^+e^-annihilation; for $x_p > 0.5$ such mesons must contain the primary c or $\bar{c}$ produced in $e^+e^- \rightarrow c\bar{c}$, and as charm production accounts for almost half of all events this is an important feature to reproduce correctly.

It was shown [115,116] from global tuning of the Lund $O(\alpha_s{}^2)$ model that TASSO data at $W = 35, 44$ GeV respectively preferred very small values of a, b around 0.1-0.2, with $a \sim b$. Unfortunately these same values gave a fragmentation spectrum of primary $D^{*\pm}$ mesons which was much softer than the data [115,116]. It is clear from equation 1.7 that fixing b at a higher value will give a harder spectrum and in the previous analyses b was thus fixed at 0.7 and a retuned, giving a value of about 1.1 - 1.3. The resulting $D^{*\pm}$ momentum spectrum using the large (a, b) combination was found to be in much better agreement with the data, but at the expense of a worse description of the global features such as the x_p and n_{ch} distributions [115,116].

The (a, b) values from the global tuning of the Lund $O(\alpha_s{}^2)$ model (Table 3.3a) are intermediate between these low and high (a, b) sets; (a, b) for the Lund cascade model (Table 3.3c) need not be the same as for the $O(\alpha_s{}^2)$ model and the former has yet to be compared with the $D^{*\pm}$ data. It is therefore interesting to see if these tuned models give a good description of the $D^{*\pm}$ fragmentation function.

The primary $D^{*\pm}$ fragmentation spectrum from high energy e^+e^-annihilation experiments [117] is shown in Fig. 3.2 [118] in terms of the variable $x = E_{D^*}/E_{beam}$[1]. The data are corrected for initial state radiation and detector effects[2]. Also shown in Fig.

---

[1] Note that great care must be taken with the experimental results as a large number of differently defined x's are sometimes used by the various experiments; see *eg.* [119].

[2] Similarly, caution must be exercised in trying to compare the high energy PETRA/PEP data with the lower energy CESR/DORIS data as effects such as initial state radiation and gluon softening alter the shape of the spectrum.

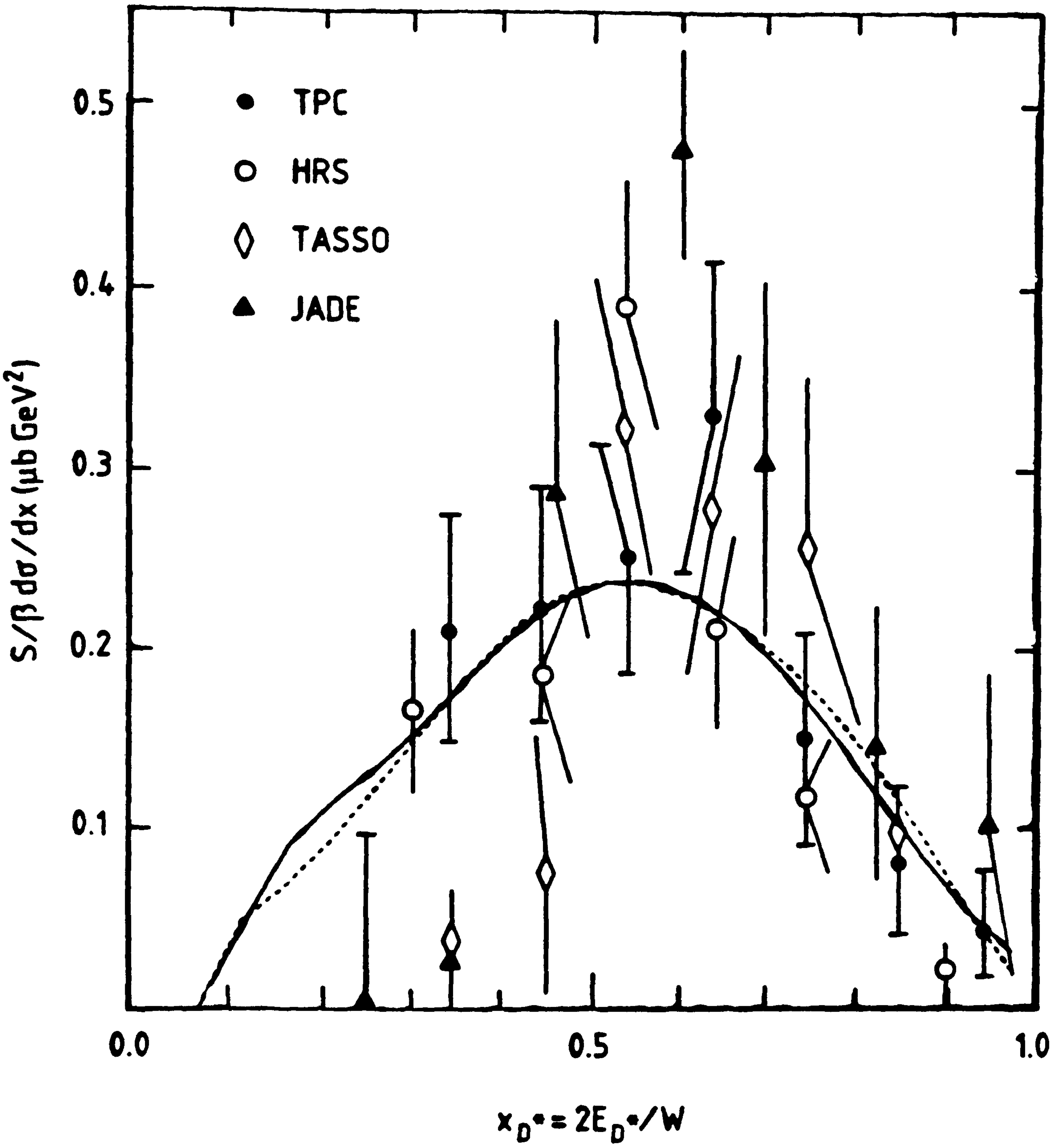

Figure 3.2: The D* fragmentation function measured in high energy e^+e^-annihilation experiments. The curves show the predictions of the Lund $O(\alpha_s{}^2)$ (dashed) and Lund LLA + $O(\alpha_s)$ (solid) models.

3.2 are the Lund $O(\alpha_s{}^2)$ and LLA + $O(\alpha_s)$ model predictions generated using the tuned values of (a, b) given in Table 3.3. In both cases the Monte Carlo spectra are in good agreement with the data beyond $x \sim 0.4$; however, it is clear that they overestimate the D^* population for $x \leq 0.4$. Both models give $< x > = 0.54$, which is just within the range 0.53 - 0.64 spanned by the data [118].

3.7 CORRECTIONS TO THE DATA

In order that results from different experiments can be compared it is usual to correct the distributions for detector acceptance and efficiency, particle interactions with the detector material, particle decays within the detector and the analysis cuts applied. As only charged particles were used here it is also necessary to correct for the undetected neutral particles. Finally, radiation of photons by the electron or positron in the initial state reduces the available energy in the e^+e^-centre of mass frame; *eg.* the actual mean hadronic c.m. energy is about 31.5 GeV for a nominal beam energy of 17.5 GeV; the amount of bremsstrahlung depends on the beam energies and it is conventional to correct for the effect so that data at different c.m. energies can be compared.

The correction factors can only be determined from a Monte Carlo simulation. The Lund cascade event generator with the tuned parameters of Table 3.3c was used together with SIMPLE simulation of all the detector effects. Initially, N_{gen}* events were generated at $W = 35$ GeV, with no QED radiative corrections, yielding the distributions $n_{gen}(x)$ of charged particles produced either in the fragmentation process or coming from the decay of particles with lifetimes less than 3×10^{-10}s. A second set of events was then generated, including QED radiative effects [96], and traced through the simulation of the TASSO detector, thereby producing hits in the tracking chambers. Energy loss, multiple scattering, photon conversions and nuclear interactions in the material of the detector as well as decays were taken into account. The events were then passed through the MILL track reconstruction, acceptance and selection programs used for the real data, yielding N_{det} accepted events corresponding to the distributions of observables $n_{det}(x)$.

A correction factor $C^i(x)$ for every bin i of every distribution x was then defined:

* $N_{gen} \sim 50000$

$$C^i(x) \quad = \quad \frac{n^i_{gen}(x)}{N_{gen}} / \frac{n^i_{det}(x)}{N_{det}}$$

The corrected distribution $n^i_{corr}(x)$ is then derived from the measured distribution $n^i_{meas}(x)$:

$$n^i_{corr}(x) \quad = \quad C^i(x)\, n^i_{meas}(x)$$

These correction factors $C^i(x)$ lie mainly in the range $0.6 < C^i(x) < 2.0$, though they are typically close to unity.

To estimate the systematic error in the correction process, this procedure was repeated using a totally different event generator incorporating an $O(\alpha_s{}^2)$ ME calculation with independent jet fragmentation [39,43], yielding a second set of correction factors. The systematic error was taken to be the difference between the two sets of correction factors, which was generally small.

The 'true' sphericity and thrust axes as well as the correction factors for the S, T, A and M^2/s distributions were determined using all (charged and neutral) particles which were either prompt or produced by the decay of particles with lifetimes less than 3×10^{-10}s.

Using a Lund Monte Carlo simulation, the charged multiplicity distribution was unfolded [120] as described in [16]. n_{ch} = 2,4 were taken from the Monte Carlo calculations. The systematic uncertainty in the unfolding procedure was estimated by using a Webber Monte Carlo simulation, the error being taken as the difference between the Lund and Webber unfolded values.

3.8 QUALITATIVE COMPARISON OF THE MODELS WITH THE DATA

For each model, the tuned parameter sets given above were used to generate 50000 MC events at W = 35 GeV, with no QED radiative corrections, no decays of particles with lifetimes greater than 3×10^{-10}s and no simulation of the detector. Distributions of the observables were then produced for each of these MC datasets and are shown in Figs.

3.3 - 3.16 compared with the fully-corrected 1986 TASSO data at W = 35 GeV*. The lines shown in the figures connect the Monte Carlo calculated points. Unless otherwise stated, the errors on the data are the sum in quadrature of the statistical errors, the uncertainty in the background subtraction and the errors from the correction procedure described in Section 3.7. For most distributions any additional systematic errors are estimated [16] to be of similar magnitude to the given errors. For the x_p distribution the total systematic errors are estimated to be 5% for $x_p < 0.05$; 4% for $0.05 < x_p < 0.7$ and 10% for $x_p > 0.7$ [16,55].

3.8.1 The Webber Model

The Webber model gives too many spherical events (Fig. 3.3), though it describes the aplanarity distribution (Fig. 3.4) quite well. The thrust (Fig. 3.5) is poorly described; the distribution is smeared about the peak at $T \sim 0.94$ giving both an excess of events at high T and also in the low-T tail. There are too many high $< p^2_{T_{in}} >$ events (Fig. 3.6) whilst the high tail of $< p^2_{T_{out}} >$ is well-represented (Fig. 3.7), though there is an excess in the first few bins at low $< p^2_{T_{out}} >$. The charged particle multiplicity distribution is shown in Fig. 3.8; the model produces too many high multiplicity events, the mean being $< n_{ch} >= 14.2$ compared to 13.6 ± 0.5 (total error) in the data. Turning to single particle distributions, $p_{T_{in}}$, $p_{T_{out}}$ p_T and x_p (Figs. 3.9 - 3.12) are well-described, though there is a slight excess of $p_{T_{in}}$ and p_T in the tails. Rapidity (Fig. 3.13) is not so well described, the MC giving too many particles for $y > 3$. M_h^2/s, M_l^2/s (Figs. 3.14, 3.15) are poorly represented with a large excess of events of low mass, though the description of $(M_h^2 - M_l^2)/s$ (Fig. 3.16) is much better.

The general conclusion is that quantities related to p_T out of the event plane are well-described, whilst those related to p_T in the plane are overestimated at high p_T. The latter is probably partly influenced by the low value of the mass above which clusters are split into two, $M_c = 2.3$ GeV/c^2, determined from the tuning. These results are in general agreement with those of Mark II [72], with minor differences in some distributions.

* These results appear in [121] where the data are also tabulated.

3.8.2 The Lund O($\alpha_s{}^2$) Model

The Lund O(α_s^2) model reproduces the sphericity distribution very accurately (Fig. 3.3), though gives far too few events of high aplanarity (Fig. 3.4). Thrust is much better described than by the Webber model (Fig. 3.5), though the peak is shifted to slightly lower T values than the data. There are slightly too many high $< p^2_{T_{in}} >$ events (Fig. 3.6) and too few high $< p^2_{T_{out}} >$ events (Fig. 3.7). $p_{T_{in}}$ and p_T are very well described (Figs. 3.9,3.11) though there is a deficiency of high $p_{T_{out}}$ tracks (Fig. 3.10). The charged multiplicity distribution (Fig. 3.8), x_p (Fig. 3.12) and rapidity (Fig. 3.13) are well described, though there are too few tracks in the range $1.4 < y < 2.4$; $< n_{ch} >$ = 13.8. The M^2/s distributions (Figs. 3.14 - 3.16) are reproduced satisfactorily.

Overall, the $p_{T_{in}}$-related quantities are accurately reproduced, whilst $p_{T_{out}}$ quantities are seriously underestimated at high $p_{T_{out}}$; there are slightly too few high thrust events. These results are in good agreement with Mark II.

3.8.3 The Lund LLA + O(α_s) Model

The best description of the data is provided by the Lund cascade model, which gives a generally good description of all observables, though inevitably with some discrepancies in some bins of certain distributions. The most serious examples are the underestimations of the high $p_{T_{in}}$ and p_T tails (Figs. 3.9,3.11). All other quantities are well reproduced. Of particular note is the excellent description of the thrust distribution (Fig. 3.5), which many models have had difficulty with in the past. In these observations we agree with the Mark II results, with only one major exception: we do not observe the serious shortfall of tracks at $x_p > 0.7$ seen in [72]. This is because of the different values of the fragmentation parameters (a, b) used in the comparisons. We have found that the combination (0.18,0.34) actually gives a very similar x_p spectrum to the default combination (0.5,0.9), except in the region $x_p > 0.6$, where the latter falls well below the former. The Mark II tuned values, (0.45,0.9) are clearly very close to the default and it is therefore no surprise that they find a much lower MC result in this region of x_p.

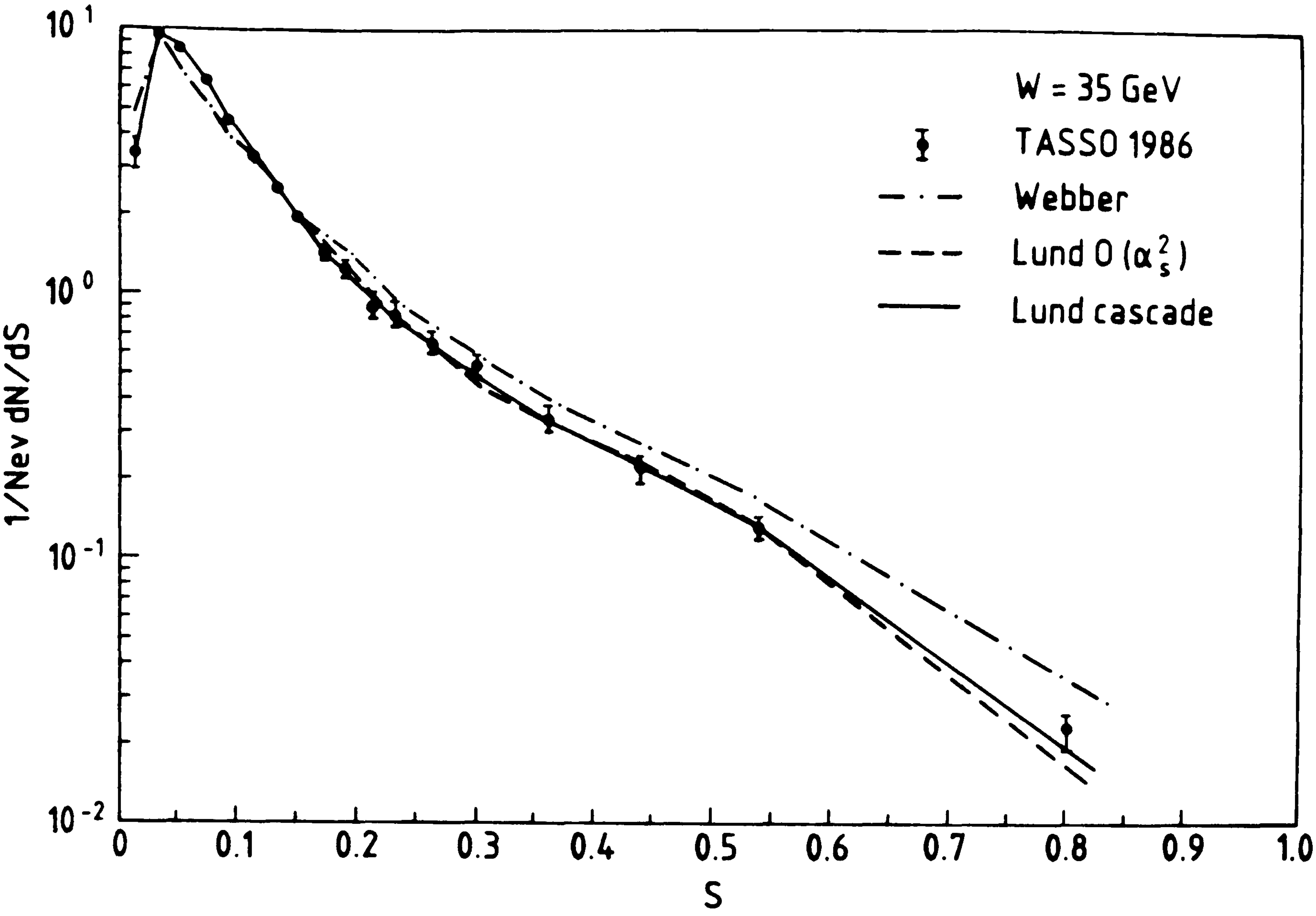

Figure 3.3: The sphericity distribution

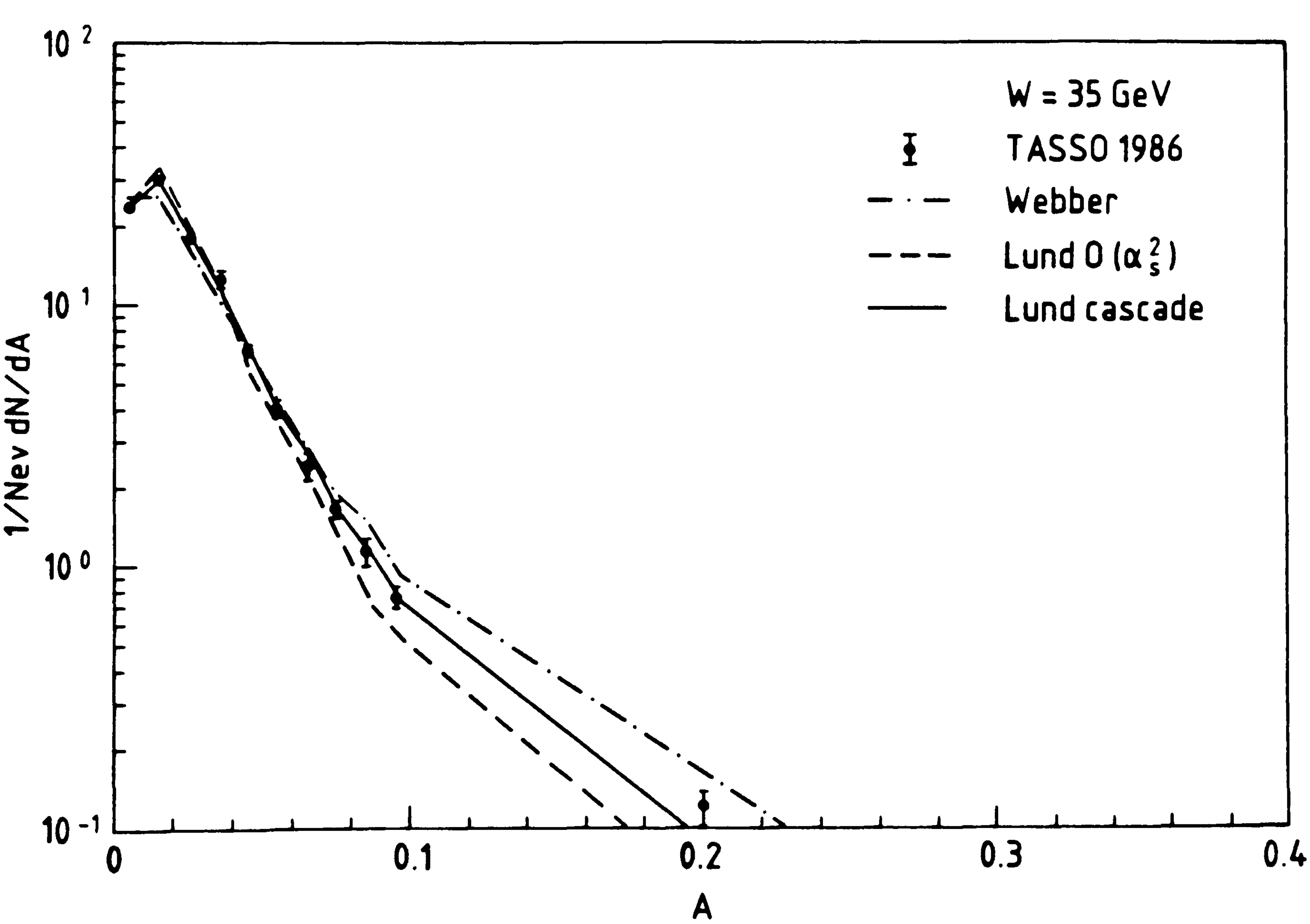

Figure 3.4: The aplanarity distribution

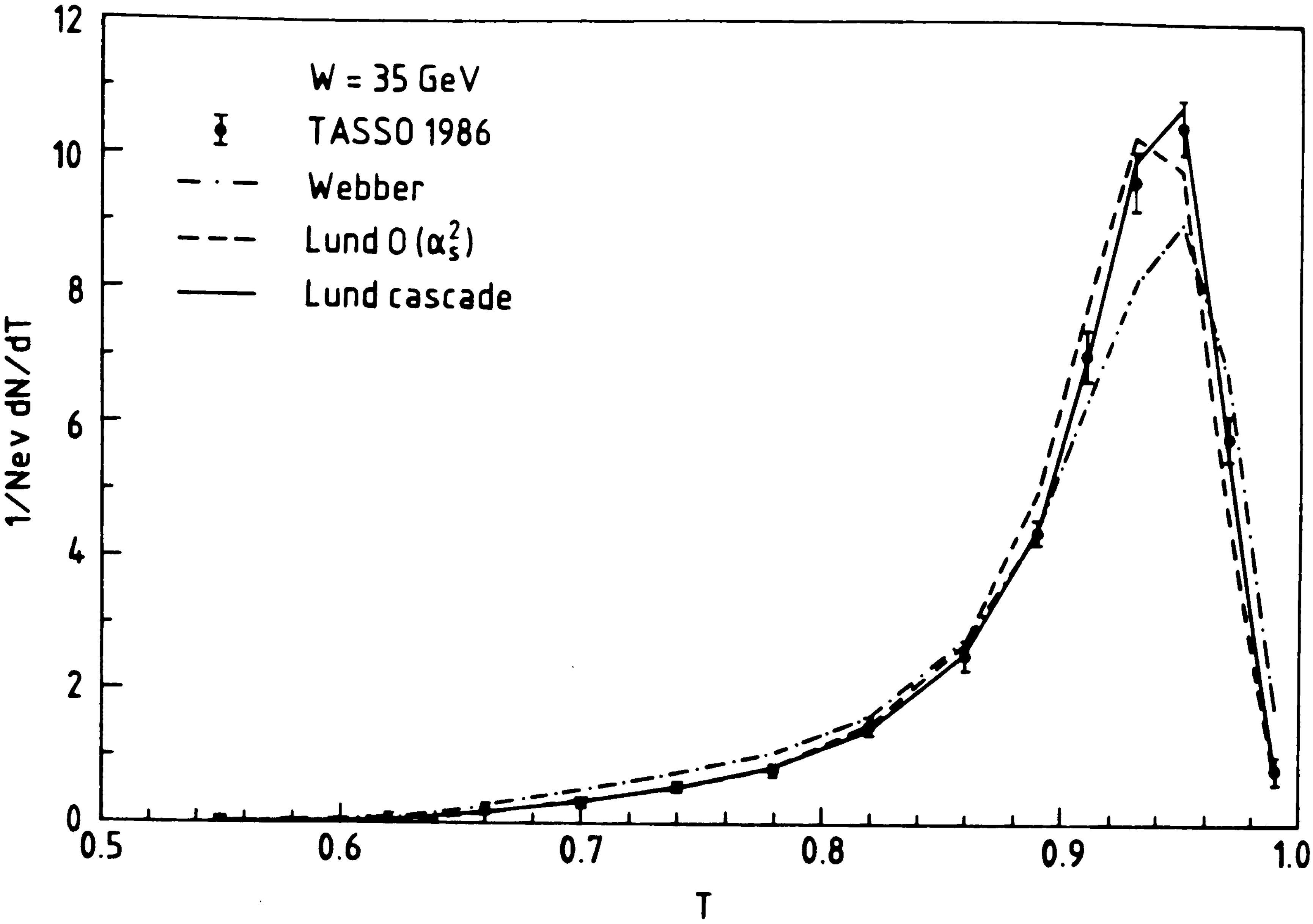

Figure 3.5: The thrust distribution

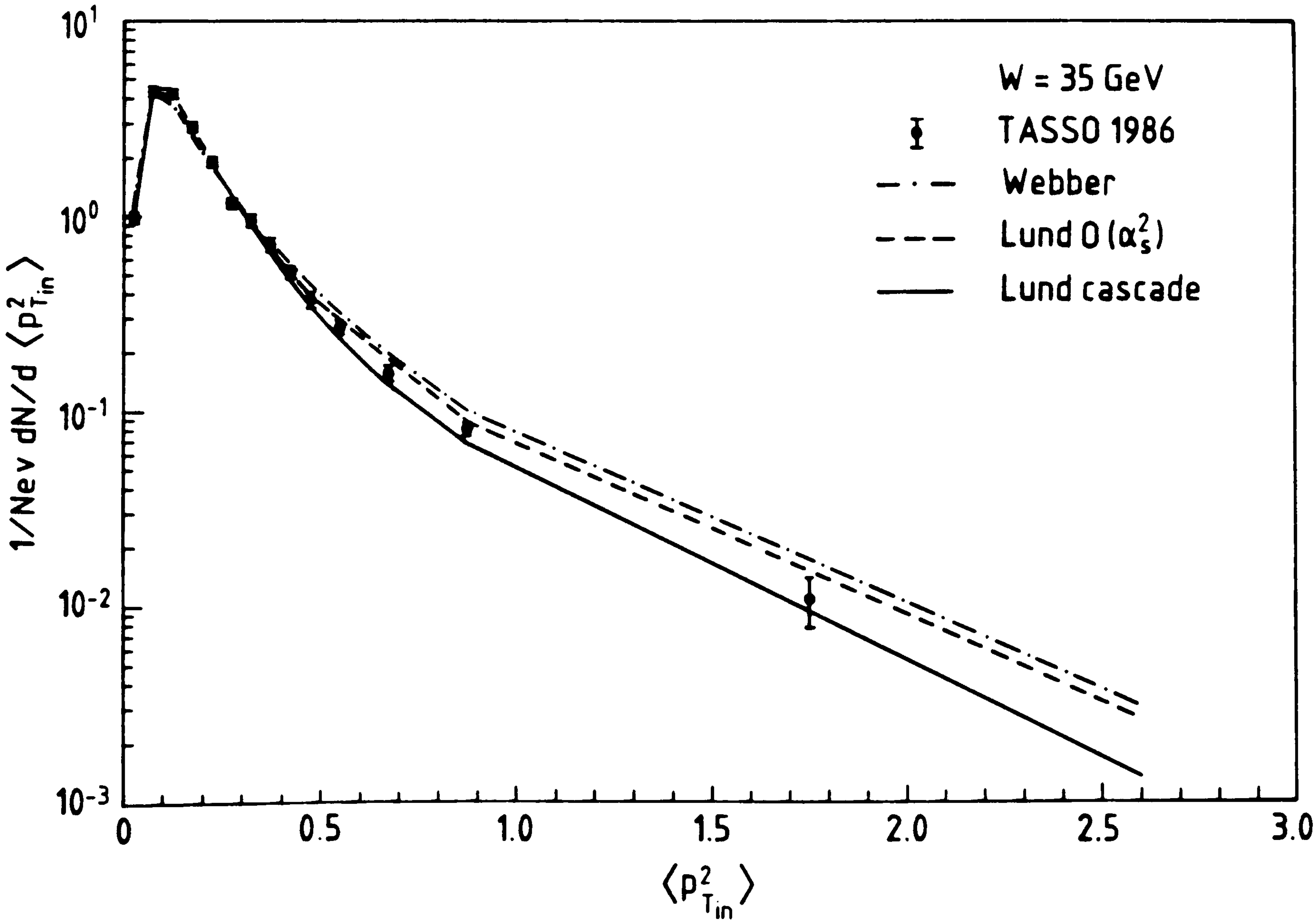

Figure 3.6: The $< p^2_{T_{in}} >$ distribution

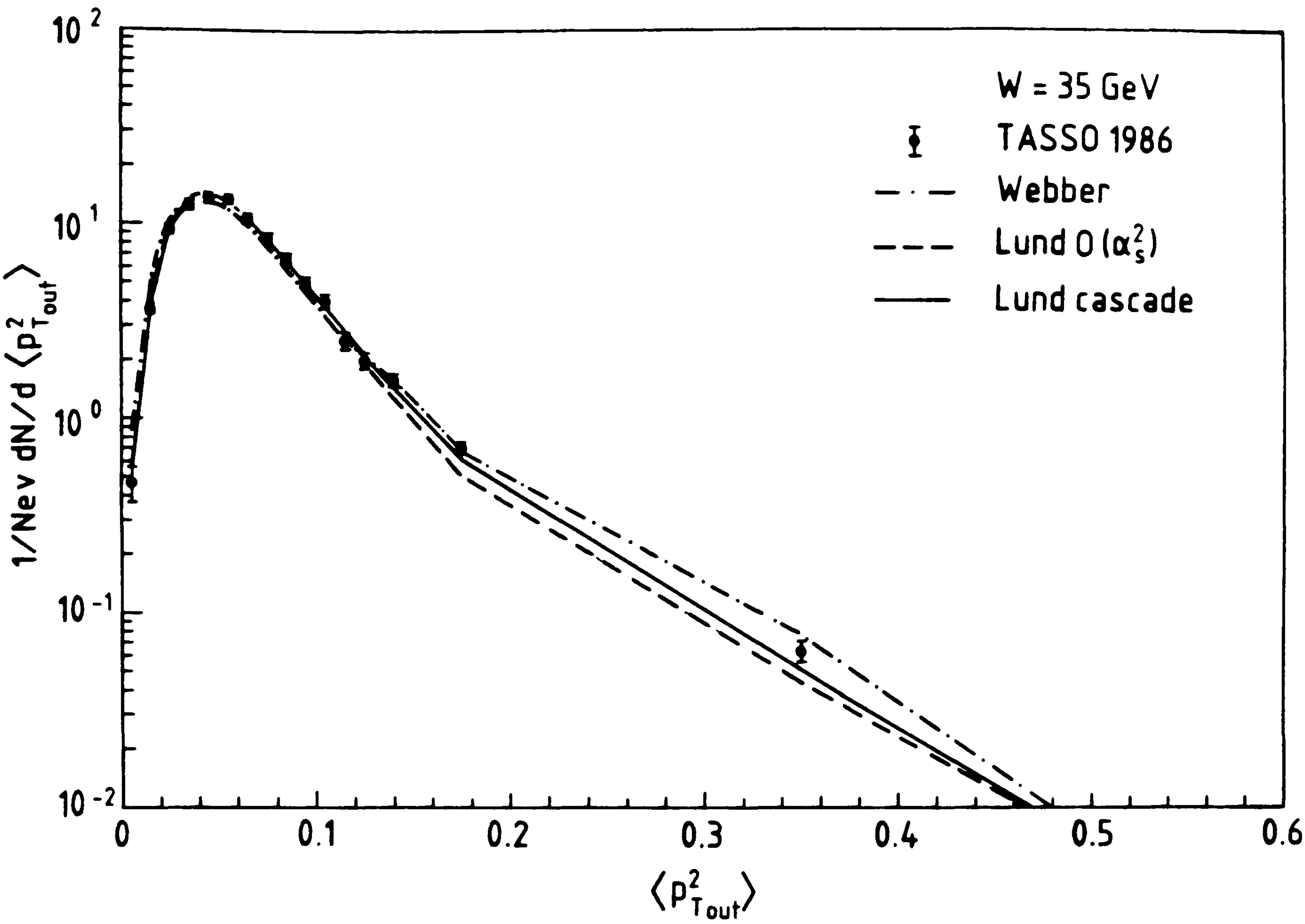

Figure 3.7: The $< p^2_{T_{out}} >$ distribution

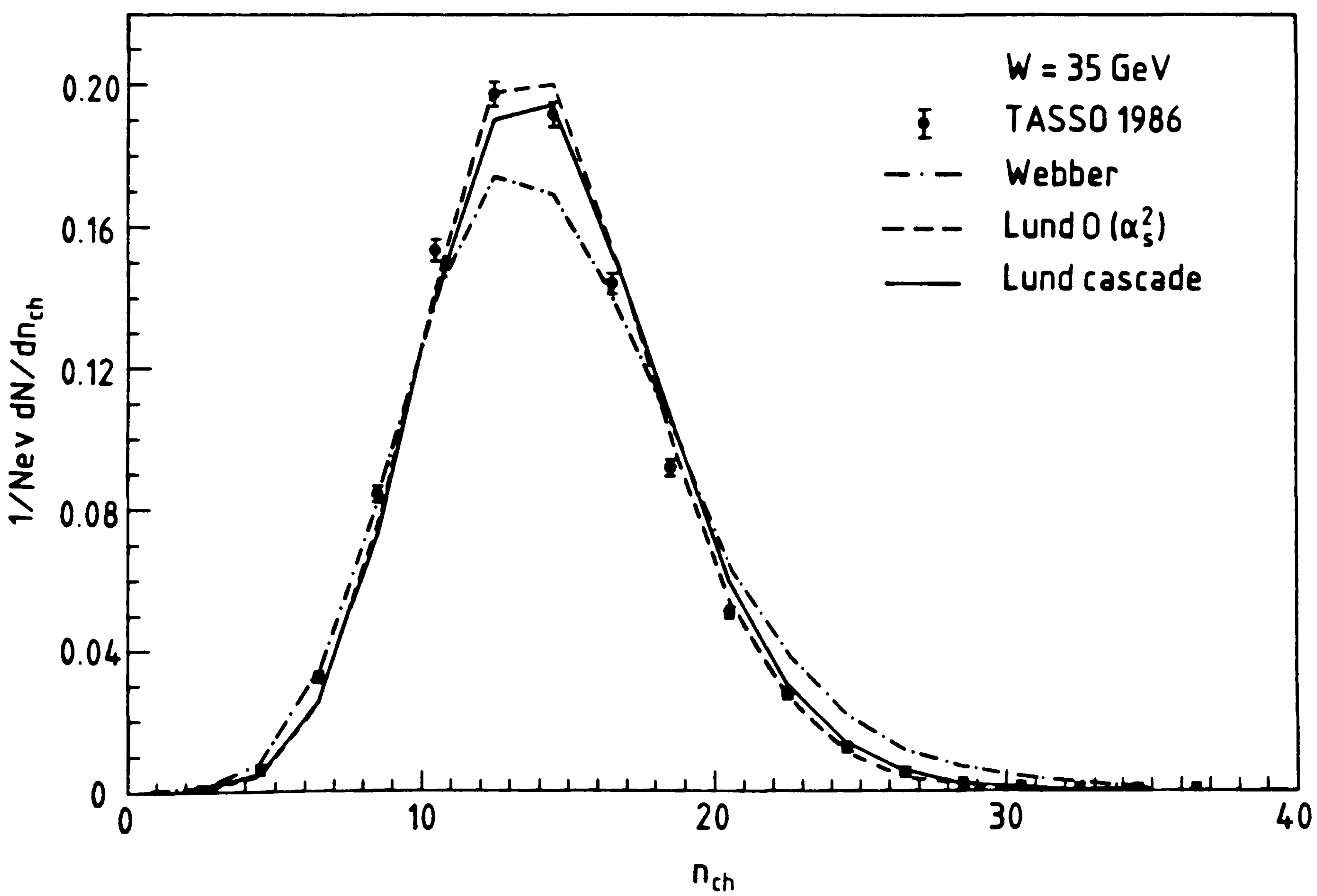

Figure 3.8: The charged particle multiplicity distribution

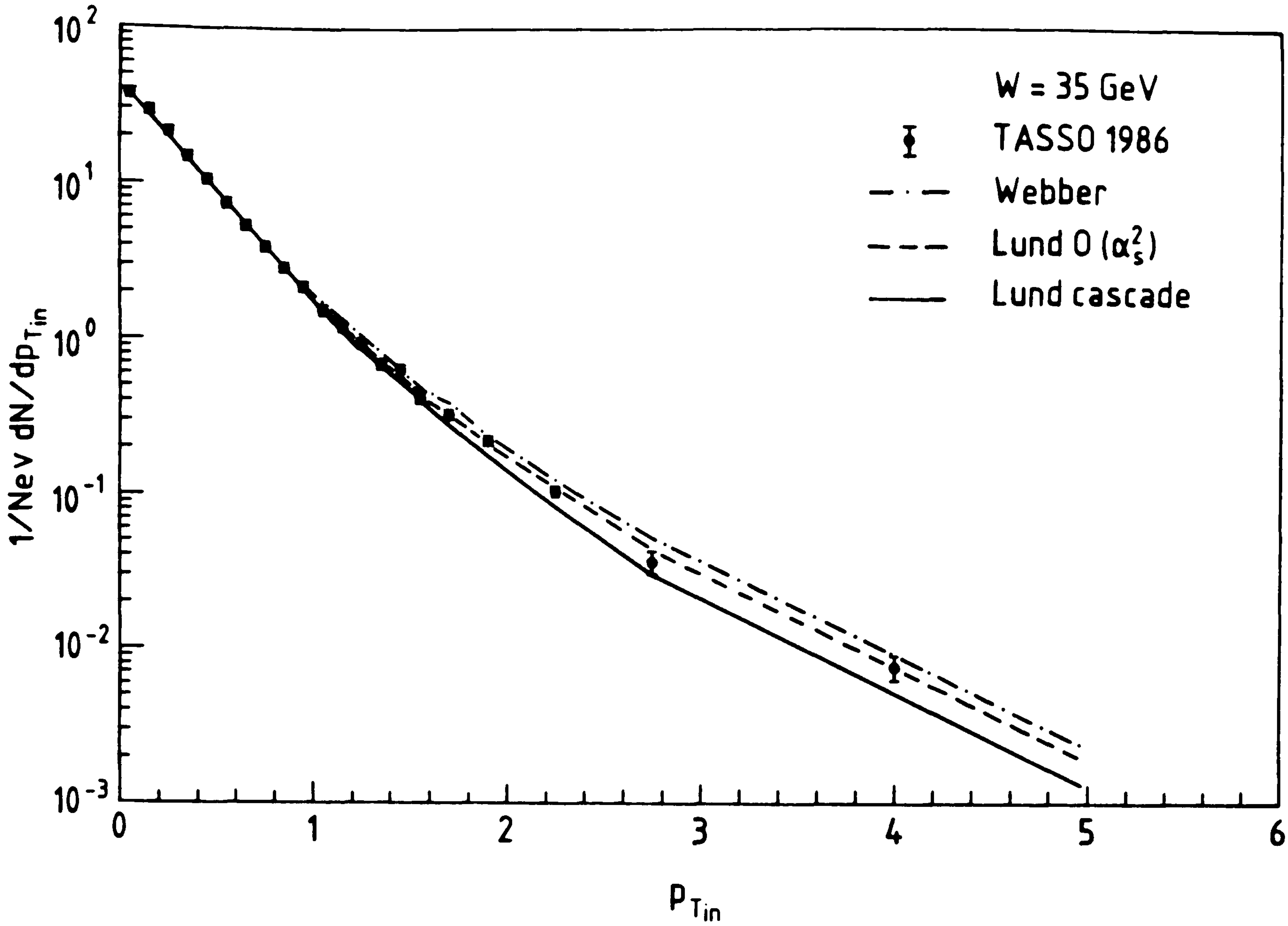

Figure 3.9: The $p_{T_{in}}$ distribution

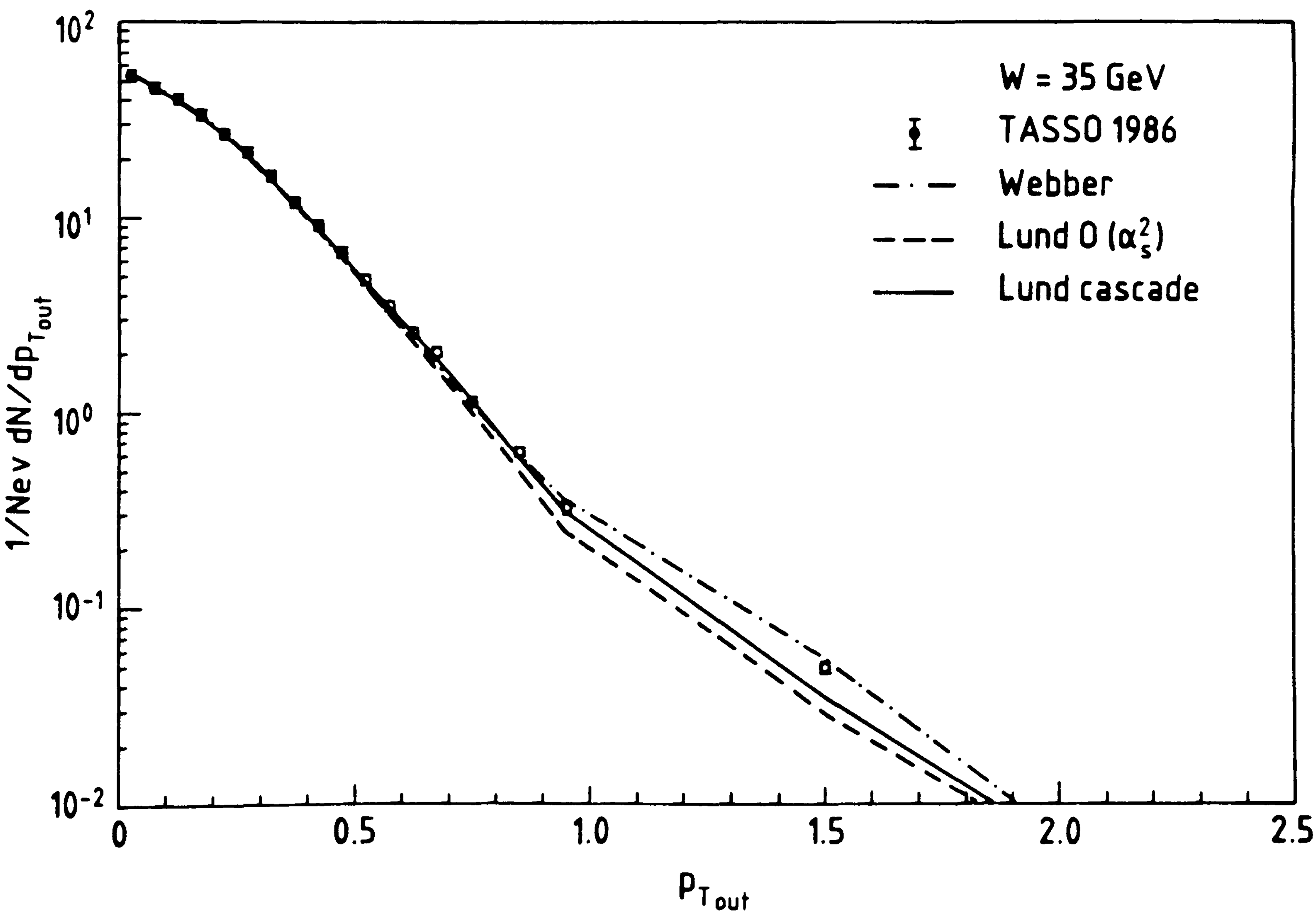

Figure 3.10: The $p_{T_{out}}$ distribution

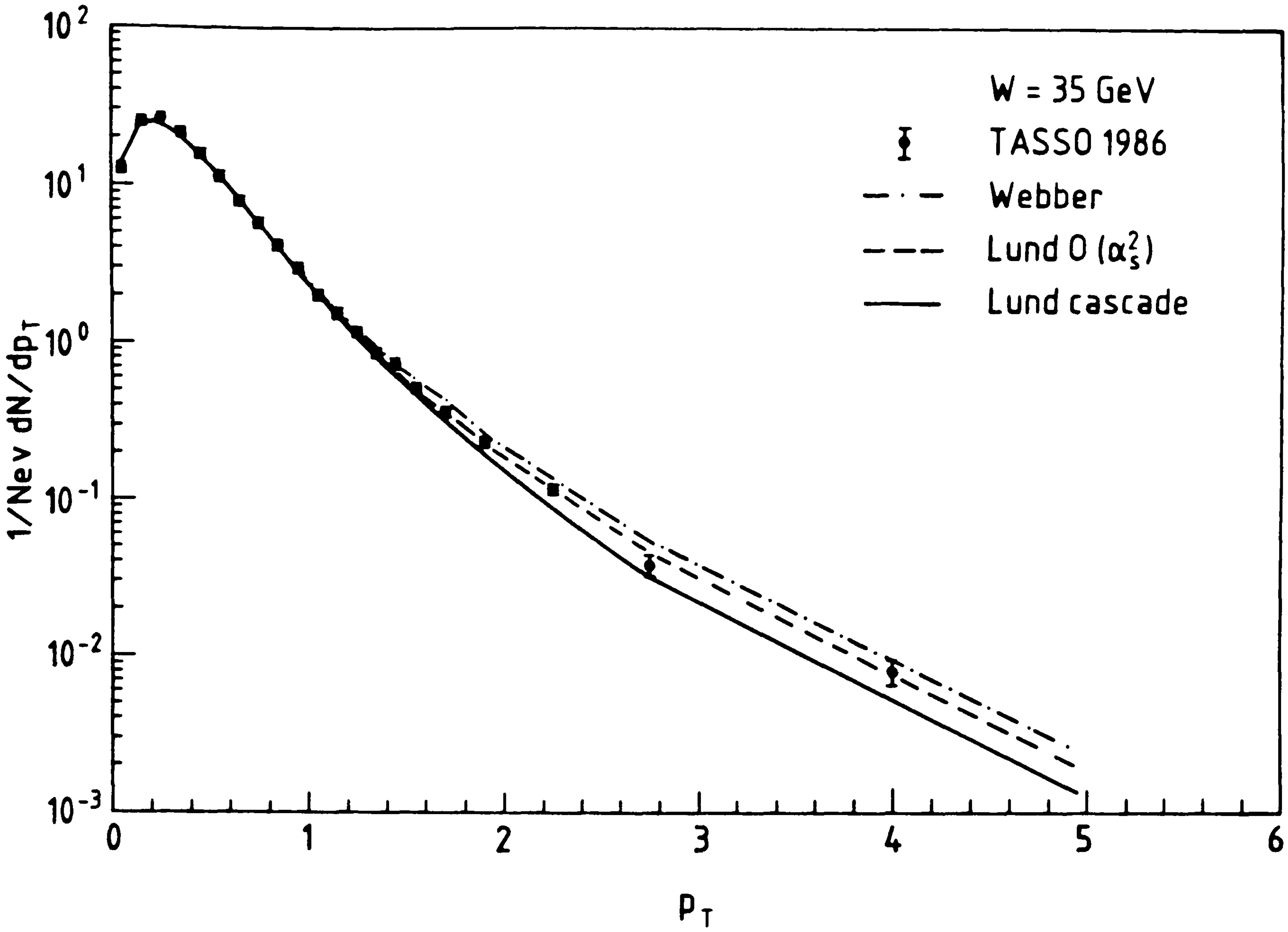

Figure 3.11: The p_T distribution

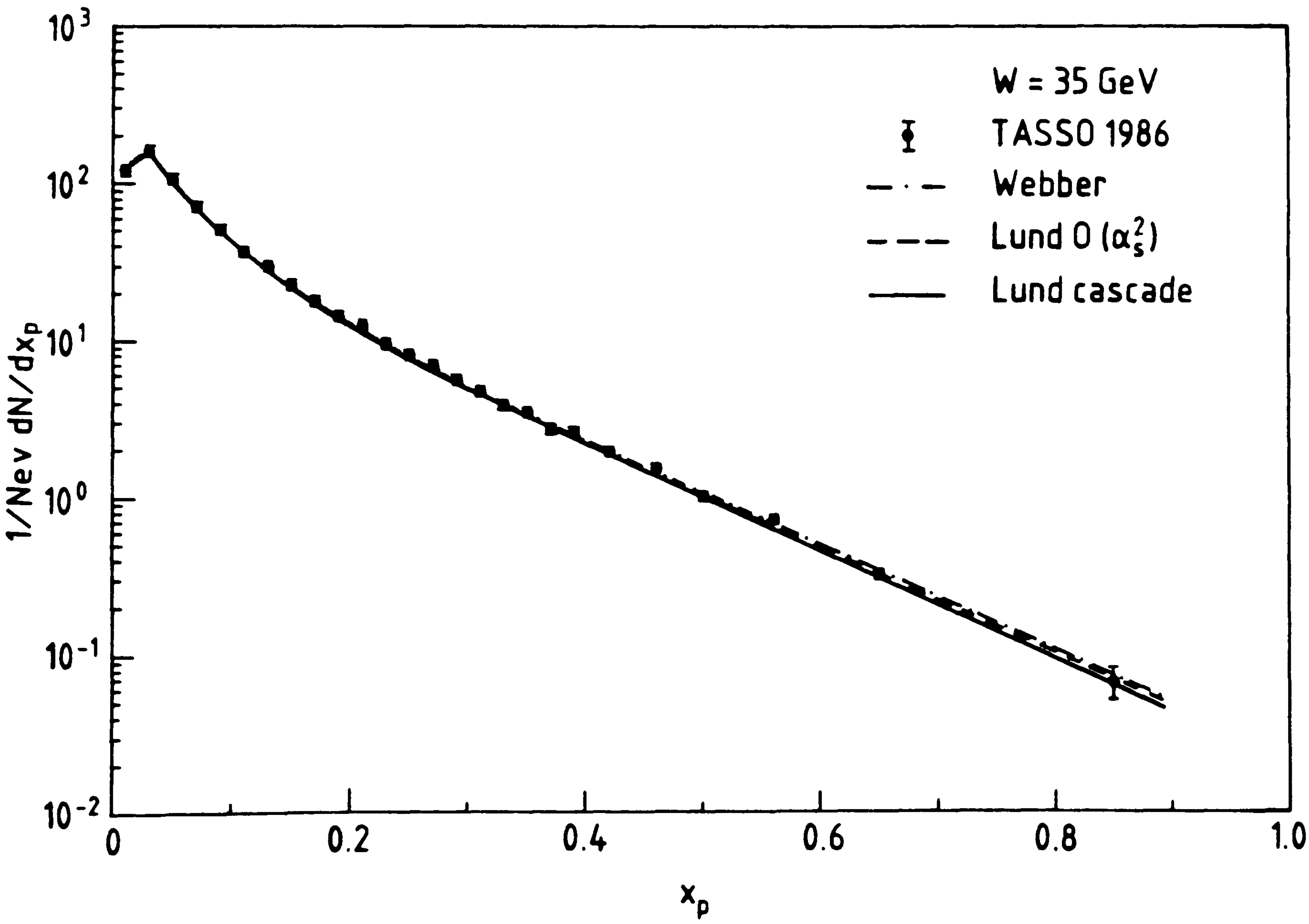

Figure 3.12: The x_p distribution

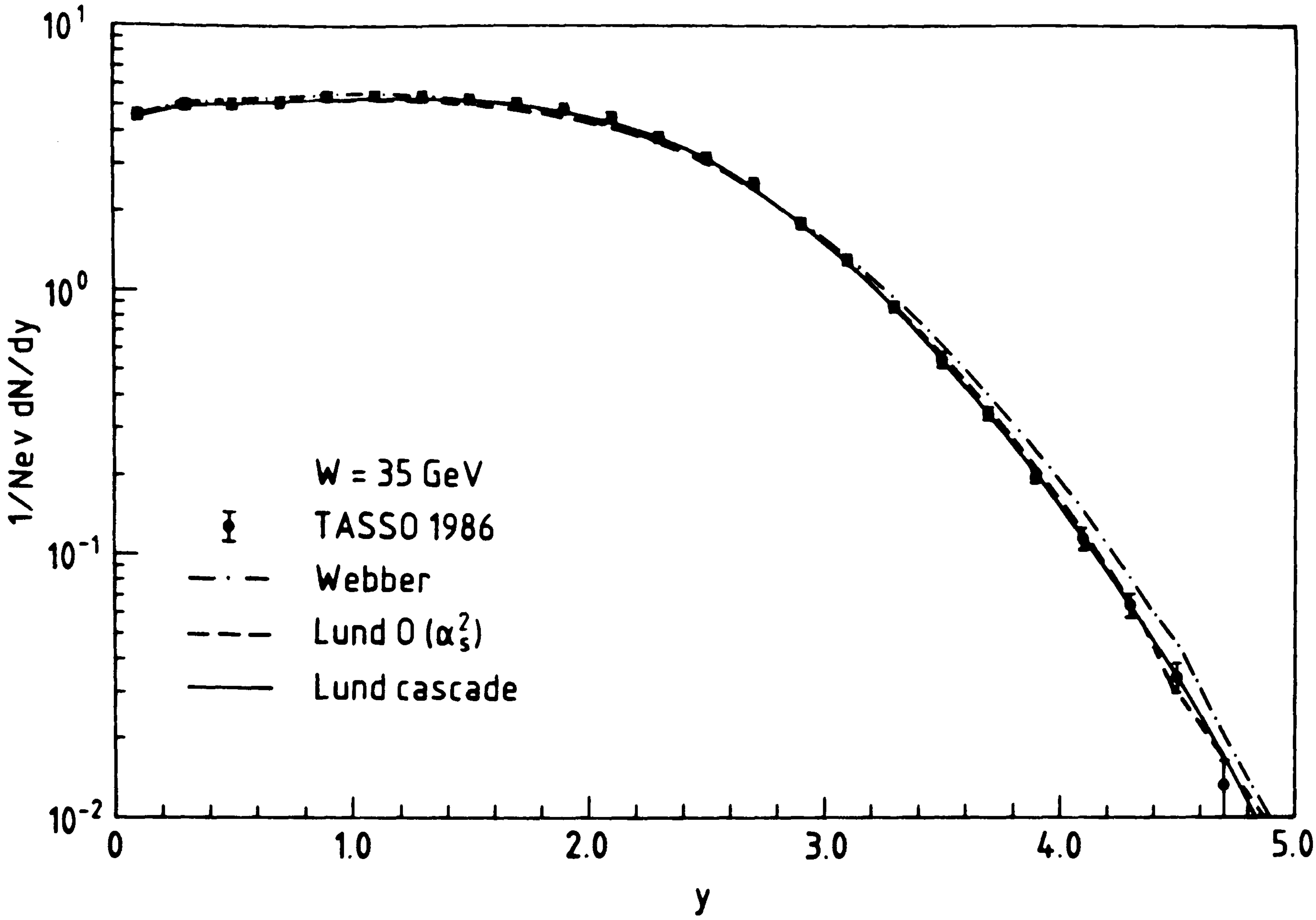

Figure 3.13: The rapidity distribution

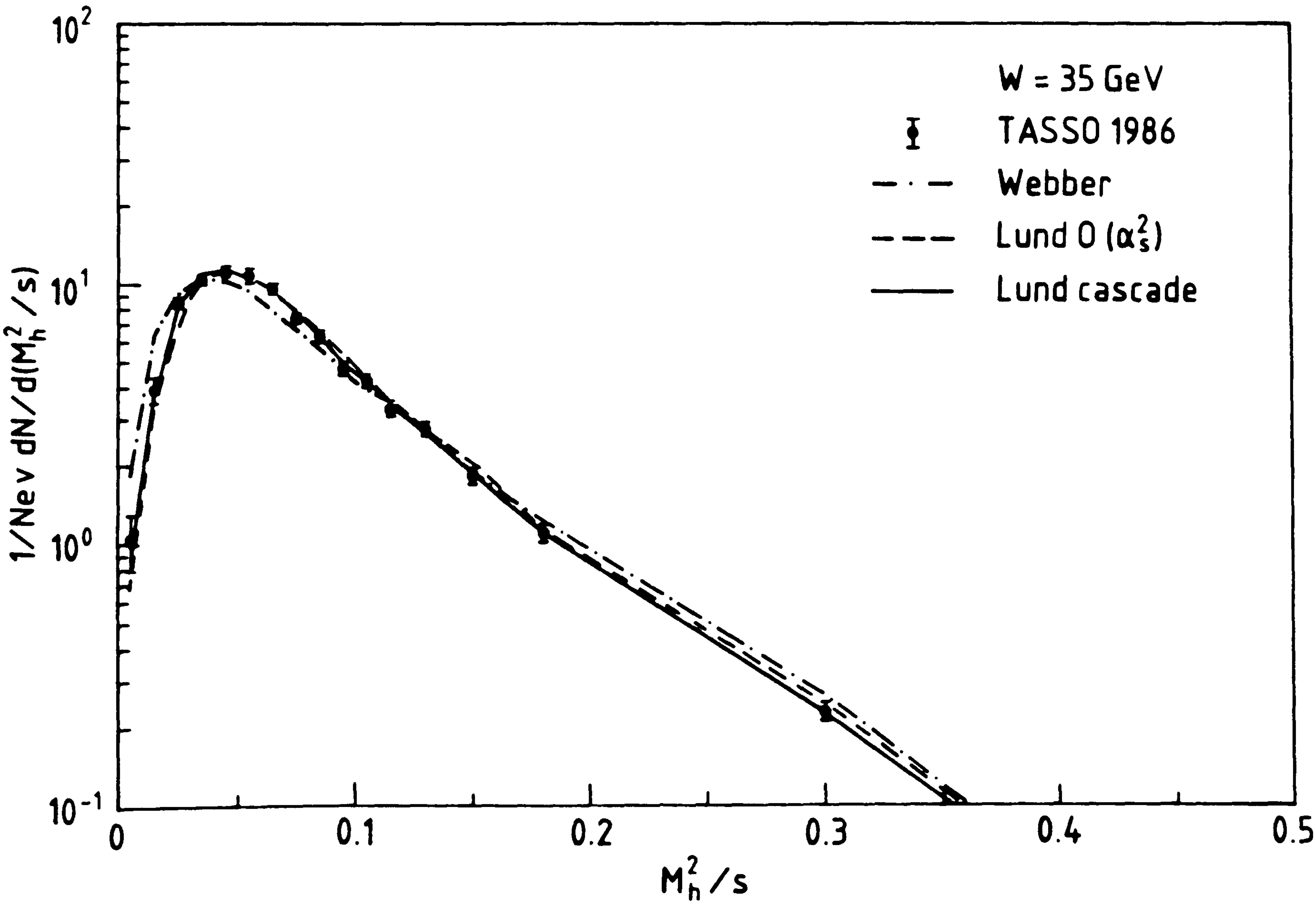

Figure 3.14: The M_h^2/s distribution

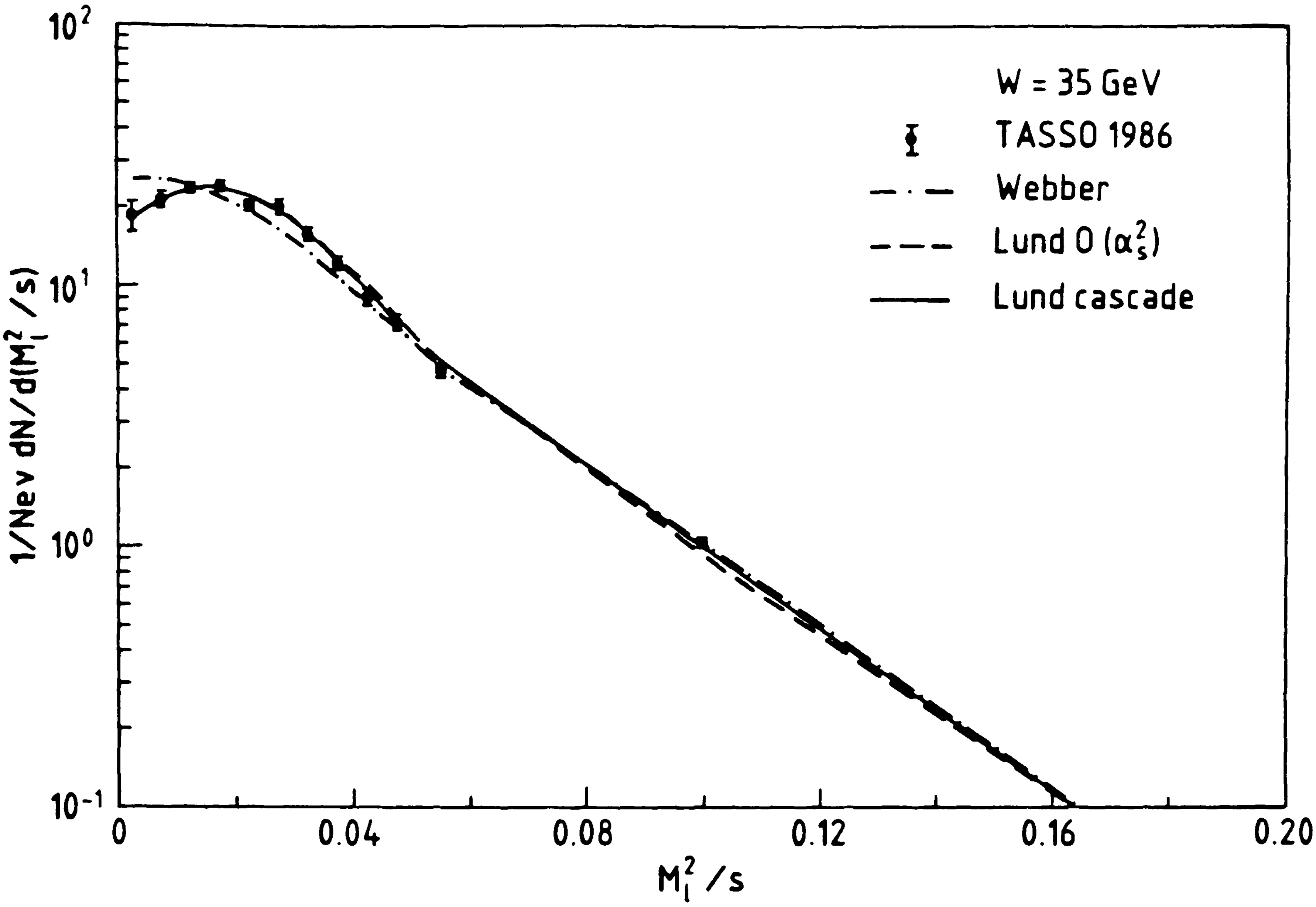

Figure 3.15: The M_l^2/s distribution

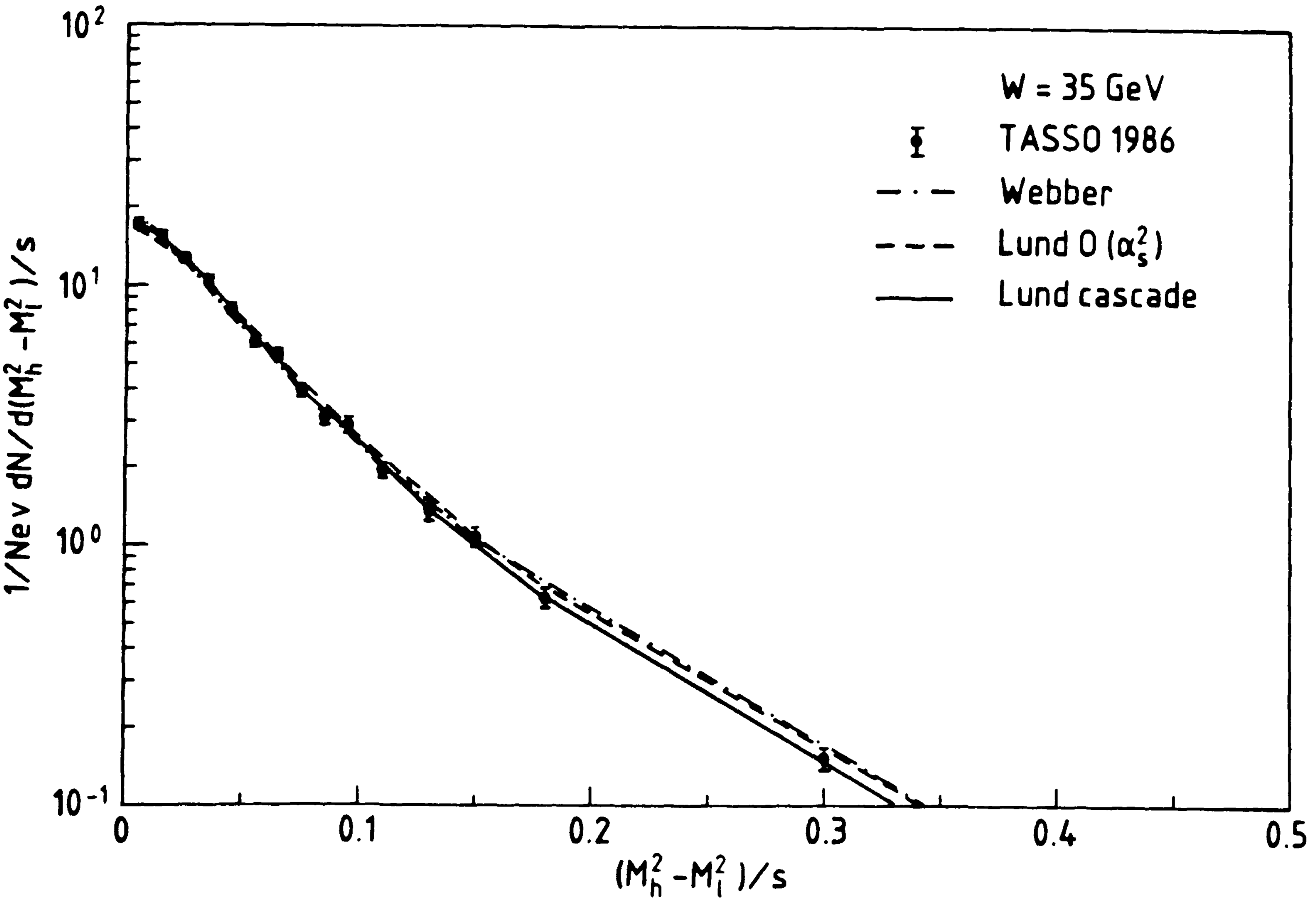

Figure 3.16: The $(M_h^2 - M_l^2)/s$ distribution

3.8.4 Summary

The $O(\alpha_s^2)$ model seems to do well with the observables related to hard gluon radiation in the event plane, namely S, $< p_{T_{in}}^2 >$, $p_{T_{in}}$, but is poorer for properties out of the event plane, which result from softer gluon radiation and hadronisation fluctuations: it does not give enough events of high A, $< p_{T_{out}}^2 >$ or tracks of high $p_{T_{out}}$, even though the transverse momentum parameter σ has a reasonable value. By contrast the LLA model (Webber cascade) is good for $p_{T_{out}}$-like observables, but overestimates $p_{T_{in}}$-like quantities. The LLA + $O(\alpha_s)$ ME model (Lund cascade) reproduces the $p_{T_{out}}$-like distributions very well but gives too few events/tracks of high $p_{T_{in}}$, though it is generally better for these than the LLA model, which overestimates.

Given that Mark II finds the same effects using rather different values of the fragmentation parameters, we feel justified in concluding that it is likely that many of these effects arise chiefly from the QCD parts of the models rather than the hadronisation, though of course these two processes cannot be isolated completely in interpreting the model results. Indeed, it was found in [72] that the combination of Webber LLA cascade + Lund string fragmentation gave somewhat better agreement with the data than the Webber cascade with cluster hadronisation.

3.9 A QUANTITATIVE COMPARISON

The best apparatus for comparing how well different models describe data is undoubtedly the human eye. Nevertheless, it is sometimes advantageous to have a more quantitative measure. For this purpose the χ^2 was invented and is often quoted, although great care must be exercised in the interpretation of its value and meaning.

3.9.1 What is χ^2?

Here, χ^2 will be defined as:

$$\chi^2 = \sum_i \frac{(x_i^{data} - x_i^{MC})^2}{({\sigma_i^{data}}^2 + {\sigma_i^{MC}}^2)}$$

where: the index i runs over all bins of some distribution in a quantity x, the distributions for data and MC have been normalized to the same quantity, eg. per event, and

x_i^{data} (x_i^{MC}) is the entry in bin i for the data (MC),
σ_i^{data} (σ_i^{MC}) is the error on the entry in bin i for the data (MC).

Suppose that the distributions have been normalized *per event.* Assume that the errors on x are statistical only for both data and MC and that they are Gaussian:

$$\sigma_i(x_i) \quad = \quad \sqrt{n_i}$$

where n_i is the number of entries in bin i. Now let the total number of events in the sample be N^{data} for the data and N^{MC} for the MC. The expression for χ^2 becomes:

$$\chi^2 \quad = \quad {N^{data}}^2 \sum_i \frac{(x_i^{data} - x_i^{MC})^2}{(n_i^{data} \; + \; f^2 \; n_i^{MC})}$$

where $f \quad = \quad N^{data}/N^{MC}$. For N^{data} constant, there is an explicit dependence in the denominator on the number of MC events, N^{MC}, generated for the comparison. Furthermore, there is also an implicit dependence in the numerator, for the scatter in the values of x^{MC} decreases as N^{MC} increases.

To illustrate the dependence of χ^2 on f, Monte Carlo data samples were produced using the Lund LLA + O(α_s) event generator (with default parameters) with SIMPLE detector simulation and TRKSEL and HADSEL cuts (Section 2.5). Distributions of physical quantities were generated using independent samples of 5000, 30000, 50000 and 100000 accepted events, and compared with the corresponding distributions for the 31176 PASS-4 events of 1986. The resulting χ^2/dof's (see below) are shown as a function of N^{MC} in Fig. 3.17; there is a clear and strong dependence: the larger the number of MC events used, the greater is the χ^2 between data and MC, though as $N^{MC} \to \infty$ (*i.e.* $f \to 0$) χ^2 tends to a constant value. Furthermore, the increase in χ^2 for a particular quantity as N^{MC} grows is much greater where there is a poor correspondence between data and MC than where the agreement is good: bad Monte Carlo's appear even worse when more events are generated, or alternatively, a good χ^2 can be obtained from a

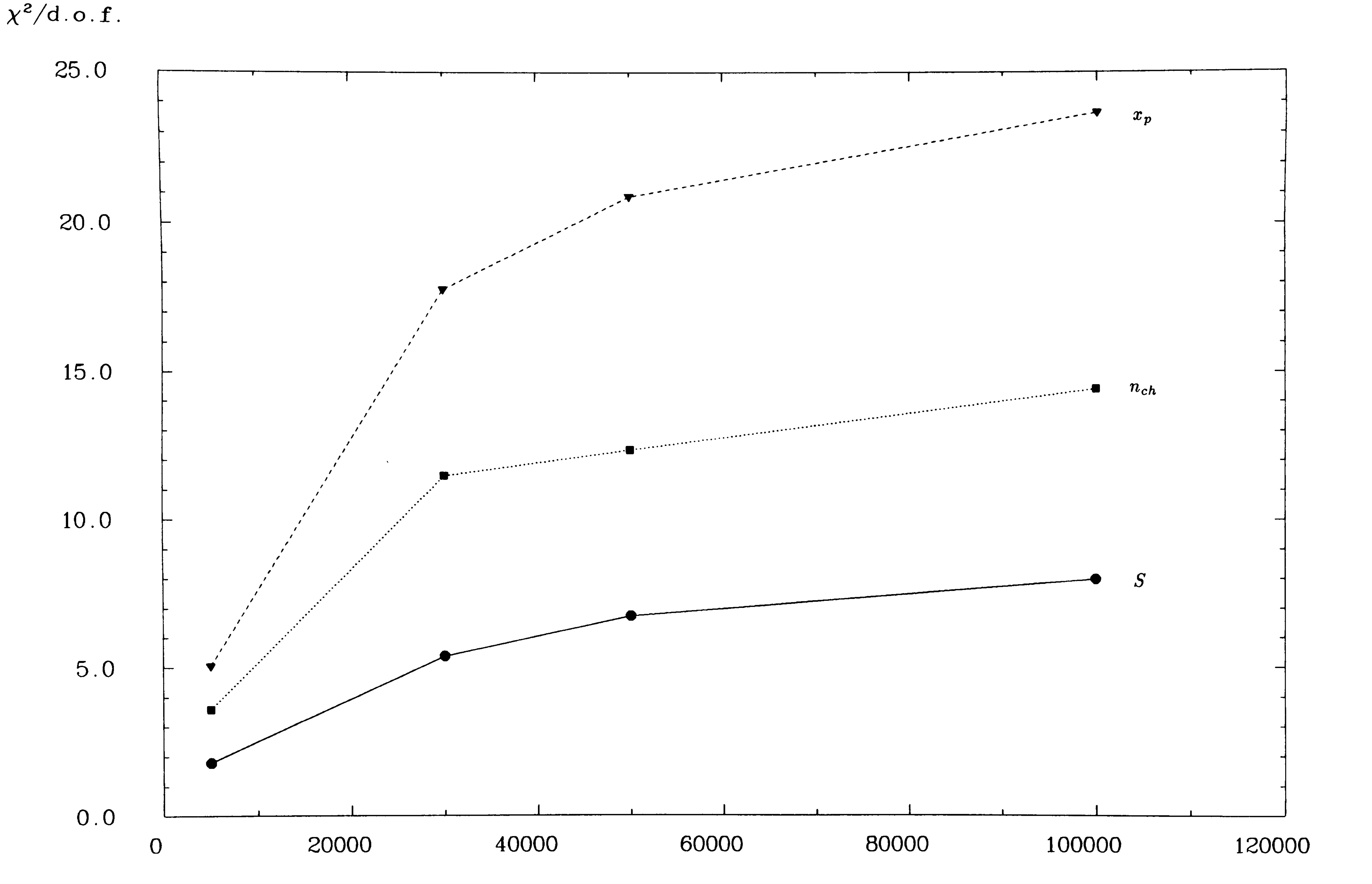

Figure 3.17: χ^2/d.o.f. between data and Monte Carlo as a function of the number of Monte Carlo events.

poor Monte Carlo by only using a small number of events in the comparison with the data.

One can conclude that it is meaningless to give a value of χ^2 for a comparison of any two event-normalized distributions without also giving the numbers of events used to produce each distribution. It is very difficult to compare the quality with which two or more models describe a data distribution unless the numbers of events in the data samples are the same *and* the numbers of events in the MC samples are the same: χ^2 is strongly dependent on N^{data} and N^{MC}.

For comparing the quality with which a model describes distributions of **different** physical quantities A, B, $C, \ldots$ it is conventional to divide χ^2 by the number of degrees of freedom and deal with χ^2/dof, where dof is usually the total number of bins, for each distribution A, B, $C, \ldots$ provided there are no correlations between the contents of different bins, which is not always the case, *eg.* for the energy-energy correlation distribution.

See [70] for a more complete discussion of χ^2.

3.9.2 Comparison of QCD Models with the Data in Terms of χ^2

18849 data events surviving the cuts described in Section 3.3 were corrected as described in Section 3.7 and compared with the samples of 50000 MC events mentioned in Section 3.8. The errors on the data were the sum in quadrature of the statistical errors and the errors on the background subtraction and data correction procedures; the errors on the MC were statistical only. The χ^2/dof's between MC and data corresponding to the distributions shown in Figs. 3.3 - 3.16 are given in Table 3.4, where the number of degrees of freedom was simply taken to be the number of bins.

For the Webber LLA model the total χ^2 is 942 for all 245 data points; for the Lund O($\alpha_s{}^2$) model it is 658 and for the Lund LLA + O(α_s) model it is 367. Note that correlations between the quantities compared make it impossible to interpret this number in absolute terms; one cannot say that the Lund LLA + O(α_s) model is three times better than the Webber LLA model. It is clear, however, that by far the best description of the data is provided by the Lund LLA + O(α_s) model and that the Lund O($\alpha_s{}^2$) model in turn gives a better description than the Webber LLA model, in agreement with the results of the visual comparison in the previous section.

Table 3.4: χ^2/dof between MC's and data

Distribution	N^0 of bins	Lund LLA + $O(\alpha_s)$	Lund $O({\alpha_s}^2)$	Webber LLA
S *	18	0.42	0.61	3.31
A	11	0.69	3.56	2.26
T	14	0.37	2.77	7.56
$< p^2_{T_{in}} >$	14	1.89	1.23	5.32
$< p^2_{T_{out}} >$	16	0.88	3.40	6.08
$p_{T_{in}}$	21	2.74	2.31	3.76
$p_{T_{out}}$ *	18	3.22	9.16	2.55
p_T	21	4.56	3.37	6.24
n_{ch} *	18	1.34	2.81	3.78
x_p *	25	1.23	1.80	0.81
y	25	0.63	1.63	3.97
M_h^2/s	16	0.55	2.21	4.88
M_l^2/s	13	0.77	1.40	3.01
$(M_h^2 - M_l^2)/s$	15	0.35	1.54	1.29

* indicates a quantity used in the tuning

3.10 CONCLUSION

The best description of the data at $W = 35$ GeV is provided by a model incorporating *both* LLA and $O(\alpha_s)$ ME QCD, thereby taking into account both hard and multiple soft gluon emission, rather than either LLA or $O(\alpha_s^2)$ QCD alone. (This $O(\alpha_s)$ ME feature could be implemented [122] in the new version of the Webber model [67].)

CHAPTER 4

ENERGY EVOLUTION OF OBSERVABLES AND MODEL PREDICTIONS AT HIGHER ENERGIES

4.1 INTRODUCTION

In the last chapter it was shown that all three tuned perturbative QCD + fragmentation models gave a generally good description of the data at W = 35 GeV. A further, more stringent test is to see if the models describe the data at energies other than that at which they were tuned. Unfortunately, there are only a few thousand events at each of the other main c.m. energies explored at PETRA (Table 2.1), namely $< W > \sim$ 14, 22 and $>$ 40 GeV, so that statistical errors are often large relative to differences between the models, especially in the tails of distributions of observables where there are relatively few events. Of the order of 60000 hadronic events have been collected by each of the detectors at the PEP storage ring at SLAC which operated at W = 29 GeV; large data samples hence exist at 29 and 35 GeV, though the energy difference is not great enough to provide a strong test of the energy evolution of the model calculations. In Section 4.2 the models are thus compared with the data across the energy range $12 \leq < W > \leq 41.5$ GeV in terms of the mean values of the physical observables, thereby making use of the full statistics at each energy.

Shortly after PETRA ceased operating as an e^+e^-collider in November 1986 the TRISTAN storage ring at KEK in Japan took on the role of the highest energy e^+e^- accelerator in the world. To date, the detectors at TRISTAN have obtained only a few hundred hadronic events above 50 GeV [12,13], though further results are expected as the data are accumulated. Meanwhile, the construction of the next generation of e^+e^- colliders is nearing completion; within the next few years SLC and LEP should provide data at the Z^0 pole, $W \sim 93$ GeV, and towards the mid 1990's LEP-2 could be supplying annihilation events up to W = 200 GeV. There will hence be e^+e^- data spanning an energy range of roughly 200 GeV, providing an opportunity for more stringent testing of the QCD + fragmentation models. Therefore the model predictions in terms of the mean values of observables are extended up to W = 200 GeV in Section 4.3, and differential distributions are presented at W = 93 and 200 GeV in Section 4.4. For the latter case results are shown with and without top quark production, where a top mass of 60 GeV/c^2 was taken to illustrate the general effects on the hadronic final state.

4.2 EVOLUTION BETWEEN $< W >$ = 12 AND 41.5 GeV

4.2.1 The Data

Between 1979 and 1983 the PETRA storage ring was operated at c.m. energies between 12.0 and 43.1 GeV. The numbers of hadronic events collected by the TASSO detector within each energy range are shown in Table 2.1 and a comprehensive study on jet fragmentation using these data was published in 1984 [16]. The data were conveniently divided into groups at mean c.m. energies of 12, 14, 22, 25, 30.5, 34.5 and 41.5 GeV. During 1984 and 1985 further data were collected in the range $35 \leq W \leq 46.8$ GeV, to bring the total number of events with $W > 40$ GeV to about 8600, the mean W being about 44 GeV. It has since been conventional to divide the data into groups at $< W >$ = 14, 22, 35 and 44 GeV, a situation which sometimes causes confusion as the latter energy includes all of the $W > 40$ GeV data, whilst the jet fragmentation publication contains only a subset of this data with $< W >$ = 41.5 GeV. Analyses of the full $W > 40$ GeV data sample in terms of jet fragmentation properties have been performed [115,116] but not published. Finally, during the stable low noise high luminosity runs of 1986, 31176 hadronic events were measured.

The mean values of some of the observables shown in Figs. 3.3 - 3.16 are presented in Figs. 4.1 - 4.7 as a function of the c.m. energy W. The data points at 35 GeV are from the present analysis using the 1986 data (labelled 'TASSO 1988'); the other data (labelled 'TASSO 1984') are taken from the previous TASSO publication [16], where the data were corrected using an O(α_s) QCD generator with independent jet fragmentation

[123]. Also shown are the MARK II [72] and HRS [99] results at $W = 29$ GeV. Unless otherwise stated, the errors on the TASSO measurements from this analysis at $W = 35$ GeV are the sum in quadrature of the statistical errors and the errors from the background subtraction and data correction; the errors on the previous TASSO data and the HRS data are statistical only; the Mark II errors are the sum in quadrature of the statistical errors and the uncertainty in the correction procedure.

4.2.2 Comparison between Models and Data

For the models, the event shape observables sphericity, thrust and aplanarity were determined using both charged and neutral particles which were either prompt or produced by the decay of particles with lifetimes less than 3×10^{-10}s. The TASSO measurements of these quantities used charged particles only, and were corrected for neutral particle effects (Section 3.7). All single track quantities are shown for charged particles only. The lines in the figures join the MC calculated points at $W = 12$, 14, 22, 35, 60, 93, 150 and 200 GeV.

The mean sphericity, $< S >$, is shown as a function of W in Fig. 4.1. The 'TASSO 1988' measurement is $< S > (W = 35) = 0.113 \pm 0.006$, which compares well with the 1984 value $< S > (W = 34.5) = 0.108 \pm 0.001$ (statistical error only). The apparently large error on the 1988 measurement reflects the systematic difference arising from using two different event generators to calculate the correction factors (Section 3.7). All three models describe the trend of the data quite well, though their overall normalisation appears to be too high: because of the tuning to the 35 GeV data point they overshoot most of the data below about 30 GeV. Mark II also found that the models tuned to their 29 GeV data point overshot the bulk of the 'TASSO 1984' data at lower energies [72].

However, a reanalysis of all of the pre-1986 TASSO data has recently been performed [115] which gave systematically higher values of $< S >$ than in the 1984 publication; for example, the recalculated $< S > (W = 34.5) = 0.117 \pm 0.001$ (statistical only) [115]. (Note that this is in excellent agreement with the 1988 value). Some of this systematic discrepancy between the two analyses of the old data may be understood in terms of the details of the computer calculation of the sphericity tensor [124], and implies that the $< S >$ data in the 1984 publication in fact all lie too low. The recalculated values [115][1] are shown in Fig. 4.2 together with the Mark II and HRS data, the 1988 35 GeV value from this analysis and the Monte Carlo results. It can be seen that the models describe the data much better: the Lund cascade is in excellent agreement; the Webber cascade still appears to be normalised too high whilst the $O({\alpha_s}^2)$ model gives too large $< S >$ below 30 GeV.

The mean thrust (Fig. 4.3) is reasonably described by all the models; the Lund cascade is probably the best. Webber is systematically lower than most of the data and the Lund $O(\alpha_s^2)$ seriously underestimates $< T >$ below 30 GeV. The apparently large error bars on the 'TASSO 1988' $W = 35$ GeV measurement reflect the uncertainty arising from using different Monte Carlo generators to determine the correction factors.

For $<< p^2_{T_{in}} >>$[2] (Fig. 4.4), both Webber and Lund $O(\alpha_s^2)$ are better than the Lund cascade, which lies systematically lower than most of the data. The HRS point at 29 GeV appears to be somewhat lower than the general trend of the TASSO data. The $<< p^2_{T_{out}} >>$ data (Fig. 4.4) are well described by all models, though again the HRS point lies below the TASSO data (the errors are rather smaller than the symbols used in the figures). $<< p^2_{T_{in}} >>$ increases more rapidly with energy than $<< p^2_{T_{out}} >>$, reflecting the growth of hard gluon emission in the event plane.

The $< p_T >$ evolution (Fig. 4.5) is well described by Webber; the Lund cascade is systematically low in the higher energy domain. The behaviour of the Lund $O(\alpha_s^2)$ model below 35 GeV seems to reflect that seen in sphericity and thrust: the generated events are basically too spherical at low energy. This appears to be a consequence of the value of $\Lambda_{\overline{MS}} = 0.62$ GeV used; the default value $\Lambda_{\overline{MS}} = 0.50$ GeV used in conjunction with either the tuned values or the default values of a, b and σ gives much better agreement with the $< p_T >$ data below 35 GeV. The value of σ used seems to be sufficient to generate $< p_T >$ in agreement with the data for the lower $\Lambda_{\overline{MS}}$ value,

[1] The errors shown are statistical only.

[2] The inner $<>$ denotes averaging over all particles in an event and the outer $<>$ denotes averaging over all events.

but the extra gluon emission resulting from the higher value causes an overestimation of $< p_T >$ at low energy.

Both the Lund models are in good agreement with the data for $< n_{ch} >$ (Fig. 4.6). Webber is systematically around ~ 0.5 - 1 unit above most of the data, though in excellent agreement with the 'TASSO 1988' and HRS measurements. For $< x_p >$ (Fig. 4.7), all models are in good agreement with the data.

4.2.3 Summary

The evolution of the mean values of the observables as a function of c.m. energy over the range $12.0 \leq < W > \leq 41.5$ GeV is generally well described by all the models using the parameters optimised at 35 GeV. The Lund LLA + O(α_s) model gives the best description of the $< S >$, $< T >$, $<< p^2_{T_{out}} >>$ $< n_{ch} >$ and $< x_p >$ evolution. For $<< p^2_{T_{in}} >>$ the O($\alpha_s{}^2$) model is most accurate; the Webber LLA model reproduces the $< p_T >$ evolution most accurately.

The general conclusion drawn from the study of the differential distributions at 35 GeV in Chapter 3 hence also applies to the evolution of the mean values across the whole PETRA energy range, namely: the LLA + O(α_s) model, including perturbative QCD calculations of both hard and multiple soft gluon emission processes, describes the data best *overall*. Note, however, that for any *particular* quantity the situation is usually quite complicated, in that one model may be better than another in some energy range but worse in a different range; careful study of Figs. 4.2 - 4.7 is necessary to discern the fine details discussed in the previous section.

4.3 PREDICTIONS OF THE MODELS UP TO W = 200 GeV

4.3.1 Motivation

There are several purposes to the high energy extrapolations presented here*.

(i) To give an idea of event characteristics at higher energies and the general physics

* See also [125].

environment within which detectors will operate. Good estimates of quantities such as particle multiplicity and momentum spectra are clearly of relevance to the design of detectors, online data processing and analysis programs. For this purpose, the differences between the model predictions in the high energy extrapolation may be taken to represent the theoretical uncertainty.

(ii) Most of the events described here involve continuum production of the five known quark flavours, and hence represent backgrounds to any new physics processes. Significant deviations from the event properties shown will be evidence for new physics.

(iii) The differences between the model results are interesting in their own right and reflect the underlying physics. In some cases the differences are so large that the data should have no difficulty in showing a preference, in contrast to the energies so far explored where all three models considered are quite successful.

4.3.2 The Model Results

The model calculations of the mean values of the observables are shown as extensions of the lower energy curves in Figs. 4.1 - 4.7. Interestingly the Webber cascade gives systematically more spherical events (Fig. 4.2) than the Lund cascade, which generates hard gluon emission according to the exact $O(\alpha_s)$ matrix element. This may well be a consequence of the cluster hadronisation mechanism employed by Webber, in which colourless clusters of mass larger than M_c are split into two before they are allowed to decay by phase space. From the tuning to TASSO data at 35 GeV c.m. energy, a low value $M_c = 2.3$ GeV/c^2 was obtained, which would have less effect at low W, where few clusters with mass above M_c are produced anyway, and also at high W, where the hadronic final state is dominated by the parton cascading rather than by hadronisation effects. The convergence of the Lund and Webber cascades around 12 and 200 GeV is consistent with this hypothesis, though other differences in the way the cascades are initialised and evolved [55,70] may also contribute. Generally closer agreement between these two cascade models was obtained by Mark II in their extrapolation up to $W =$ 93 GeV [72], using $M_c = 3.0$ GeV, though the values of other parameters were different from those used here (see Section 3.6.3). Above 60 GeV the Lund $O(\alpha_s^2)$ model gives fewer spherical events (Fig. 4.2), also reflected in higher mean thrust values (Fig. 4.3). Again in Fig. 4.3 the Lund and Webber cascades agree at low and high W, though Webber gives fewer high thrust events in between. $< S >$ at $W = 200$ GeV is predicted to be about half of the 35 GeV value, whilst $< T >$ rises gradually from 0.9 (35 GeV) to 0.95 (200 GeV).

Though the $<< p_{T_{in}}^2 >>$ and $<< p_{T_{out}}^2 >>$ data are reasonably well described by all three models (Fig. 4.4), large differences between them emerge in the high energy extrapolation: the Lund $O(\alpha_s^2)$ model gives significantly higher $<< p_{T_{in}}^2 >>$ than the two cascades, whilst the multiple soft gluon emission in the LLA formalism shows itself as greater $<< p_{T_{out}}^2 >>$ relative to the $O(\alpha_s^2)$ calculation. The high energy results for single particle $< p_T >$ (relative to the sphericity axis) are similar (Fig. 4.5) for all three models. $< p_T > \sim 0.6, 0.8$ GeV/c at $W = 100, 200$ GeV respectively, compared to $\sim$ 0.4 GeV/c around $W = 30$ GeV.

The good agreement between the two cascade models in terms of $< n_{ch} >$ (Fig. 4.6), for $W > 40$ GeV, is remarkable. The data are described quite well by all models, but above 50 GeV c.m. energy the LLA cascades give a higher multiplicity which increases faster with W: they predict about 21 charged particles per event at $W = 93$ GeV, 3 units above $O(\alpha_s^2)$, and about 28 charged particles at 200 GeV, 7 units higher than $O(\alpha_s^2)$. This discrepancy becomes even larger as TeV energies are approached [63]. It is interesting that the average n_{ch} from the cascade Monte Carlos agrees well, to within roughly 10%, with the expected multiplicity evolution formula derived analytically from leading and next-to-leading order QCD [126] and normalised at low energies to take the incalculable non-perturbative effects into account.

Differences between the cascade models and the $O(\alpha_s^2)$ model are further evident in the behaviour of mean particle $x_p = 2p/W$ (Fig. 4.7), where the hard tail at high W for the latter is a consequence of the fragmentation of a small number of hard partons, whereas the emission of many soft partons in the LLA cascades has an overall softening effect on the particle momentum spectrum of the hadronic final state. At $W = 93$ GeV the typical charged particle momentum is $\sim$ 2.7, 3.1 GeV/c for the LLA cascades and $O(\alpha_s^2)$ models respectively.

4.4 DIFFERENTIAL DISTRIBUTIONS AT HIGHER ENERGIES

From Figs. 4.2 - 4.7 it can be seen that although the energy evolution of the mean values of the observables in the data is reasonably well described by all the models, differences between them subsequently appear at higher energies. The predicted differential distributions are shown in Figs. 4.8 - 4.18 at the Z^0 energy, $W = 93$ GeV, for u,d,s,c,b events generated with all three models, as well as for comparison the 'TASSO 1988' 35 GeV data to illustrate how the distributions change with energy. For the sake of clarity, only the Lund cascade prediction is shown at 200 GeV as an additional curve; this model was found (Chapter 3) to give the best overall description of the 35 GeV data, as well as a good representation of the energy evolution of the mean values in the range $12.0 \leq < W > \leq 41.5$ GeV (Section 4.3). The effect of top quark production on the global properties of the hadronic final state at $W = 200$ GeV is illustrated for several quantities for the case $m_{top} = 60$ GeV/c^2, where u,d,s,c,b+t production was simulated using the Lund cascade*. For the models the lines in the figures join the MC calculated points.

Similar sphericity distributions at 93 GeV (Fig. 4.8) are given by all models; the decrease in the number of spherical events as W increases is apparent. Including top quark production does give more spherical events, though for the sake of clarity this is not shown in the figure. The difference in aplanarity between the Lund O(α_s^2) and the Lund cascade is huge at 93 GeV (Fig. 4.9), though the Lund cascade itself gives fewer events than Webber at high A. Because of the inherent high transverse momentum of top hadron decay products, top quark production gives rise to many aplanar events, illustrated dramatically in Fig. 4.9. Similar differences in thrust are observed at 93 GeV (Fig. 4.10) as at 35 GeV; low thrust events are somewhat suppressed in the Lund

* After string fragmentation of the parton state, weak decays of top hadrons are treated according to the spectator model. The decay products are distributed according to the standard V-A matrix elements. In most cases the spectator quark system and the q$\bar{\text{q}}$ system from the W are each fragmented separately by connecting a Lund string beween the two quarks, although the other possibility of a rearrangement of the colour singlet systems via a soft gluon exchange is also taken into account [53].

$O(\alpha_s^2)$ model whilst Webber gives more of these events than the Lund cascade and correspondingly fewer in the peak around $T = 0.96$. Top quark production gives rise to an excess of events around $T \sim 0.8$ and a suppressed rate of collimated events ($T \sim 1$) compared to u,d,s,c,b only (Fig. 4.10).

At $W = 93$ GeV the Lund $O(\alpha_s^2)$ model gives more very low $< p_{T_{in}}^2 >$ events than the cascades (Fig. 4.11), though fewer around 0.2 - 0.6 $(\mathrm{GeV/c})^2$. The main differences are hence in the low $< p_{T_{in}}^2 >$ region rather than the high $< p_{T_{in}}^2 >$ tail. The large discrepancies between models seen in aplanarity are reflected in $< p_{T_{out}}^2 >$ (Fig. 4.12) where the $O(\alpha_s^2)$ distribution is shifted towards low $< p_{T_{out}}^2 >$, and $p_{T_{out}}$ (Fig. 4.14); the differences between Lund and Webber cascades are large at 93 GeV. Both $< p_{T_{in}}^2 >$ and $< p_{T_{out}}^2 >$ are not as sensitive to top production (not shown) as the aplanarity. The $p_{T_{in}}$ and p_T distributions (Figs. 4.13,4.15 respectively) are rather similar for all models at 93 GeV; a significant high momentum tail develops at 200 GeV, further emphasised by the higher particle multiplicity. Greater numbers of tracks of high $p_{T_{in}}$ and $p_{T_{out}}$ are evident for top production in Figs. 4.13,4.14.

Bearing in mind that at 93 GeV the Lund $O(\alpha_s^2)$ model has a lower charged multiplicity by three units, its very hard x_p spectrum (Fig. 4.16) relative to the cascades is a striking consequence of the absence of multiple gluon bremsstrahlung. This smaller multiplicity is reflected in a lower rapidity plateau (Fig. 4.18), though this model gives more particles at high y, in comparison to the rather similar distributions for the two cascades. Inclusion of top production is illustrated in Fig. 4.18, where a $\sim 20\%$ excess of tracks around $y \sim 1$ reflects the intrinsic high p_T of top hadron decay products. There is no appreciable change in particle multiplicity or momentum (x_p) distributions at $W = 200$ GeV with the top quark included (not shown).

4.4.1 MULTIPLICITY DISTRIBUTIONS AND KNO SCALING

In 1972 it was predicted [127] that under certain general assumptions the function $< n > P_n(\frac{n}{<n>})$, where P_n is the probability of obtaining n particles when the mean is $< n >$, is independent of s or $< n >$; this is the so-called KNO scaling law. An equivalent statement is that the dispersion, $D = \sqrt{< n^2 > - < n >^2}$, is directly proportional to $< n >$. It is currently fashionable to discuss multiplicity distributions within this context.

Charged particle multiplicity distributions are shown in Fig. 4.17, where in addition to higher mean values the cascade models also have larger dispersions at 93 GeV than the O(α_s^2) model. The Lund cascade distribution at 200 GeV is very broad, with a long tail extending beyond 50 charged particles per event.

It has already been shown [16] that the e^+e^-annihilation data between $\sim$ 5 and 45 GeV exhibit approximate KNO scaling to within about 20%. Taking the Lund cascade model as an example, the predicted multiplicity distributions at W = 35 GeV (Fig. 3.8) and 93, 200 GeV (Fig. 4.17) obey this law to about the same degree of accuracy. However, to the extent that the scaling law does hold, the origin is likely to be a complicated coincidence, arising from effects which violate the initial assumptions, and is of no fundamental significance [128].

4.5 SUMMARY

The three most successful perturbative QCD + fragmentation models have been analysed at c.m. energies between 12 and 200 GeV using parameters optimised at 35 GeV. All the models reproduce reasonably well the evolution of the mean values of observables in the data as a function of c.m. energy in the range $12 \leq < W > \leq 41.5$ GeV, though differences between model predictions subsequently appear at higher energies. For some quantities, *eg.* $<< p_{T_{in}}^2 >>$, $<< p_{T_{out}}^2 >>$, $< n_{ch} >$ and $< x_p >$, the differences are extremely large above about 60 GeV, so that the data to be collected at the forthcoming e^+e^- colliders in the 100 GeV energy range should easily be able to discriminate between models.

Large differences between models at W = 93 GeV are also seen in the differential distributions of quantities such as aplanarity, thrust, $<< p_{T_{out}}^2 >>$ and $p_{T_{out}}$, though for other variables, such as sphericity and $p_{T_{in}}$, the differences are smaller, providing a less sensitive test of the models. The Lund cascade was generally the most successful at representing the PETRA/PEP data (see Chapter 3 and [72]) so that results were also shown for this model at W = 200 GeV in order to get some idea of the hadronic final state properties, though clearly an extrapolation to 200 GeV using model parameters extracted at 35 GeV should not be regarded as anything other than a reasonable estimate.

The inclusion of top quark production at $W = 200$ GeV was simulated using the Lund cascade for $m_{top} = 60$ GeV/c^2. Of the event shape observables, the aplanarity and thrust distributions appear to be particularly sensitive to the presence of the top quark events. Kinematic effects in top hadron decay appear as an excess of particles at high $p_{T_{in}}$ and $p_{T_{out}}$ and around a rapidity of 1.

From experience of comparing the models with data at PETRA and PEP, where no one model accurately describes every quantity presented here at a single centre of mass energy, eg. 29 GeV [72] or 35 GeV (Chapter 3), let alone across the full energy range already explored (Section 4.2), it is clear that to describe additionally data around 100 GeV or higher, with parameters which are fixed for all energies, will prove a challenging test of the QCD + fragmentation models.

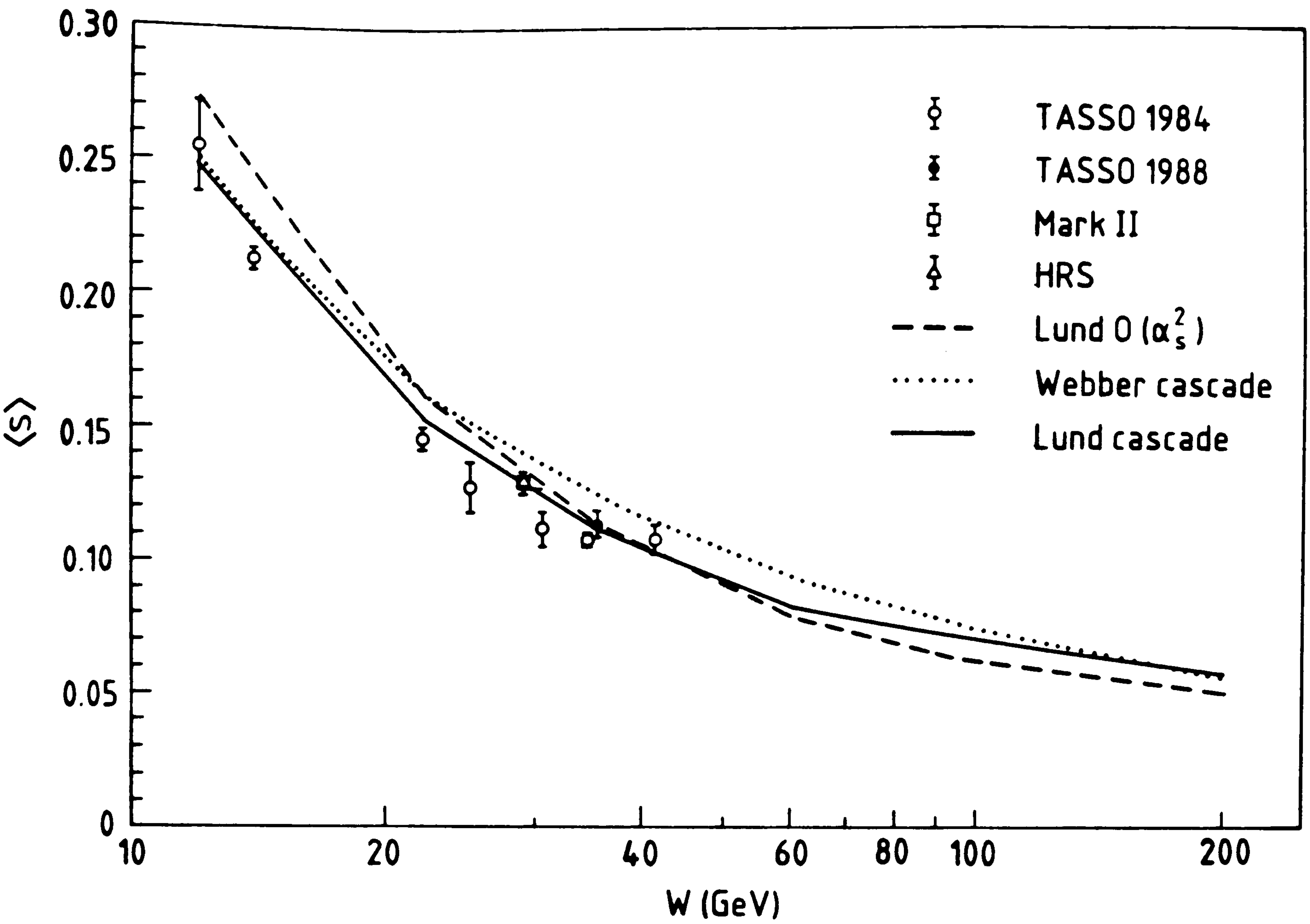

Figure 4.1: The mean sphericity as a function of W including the original 1984 calculations for the TASSO data.

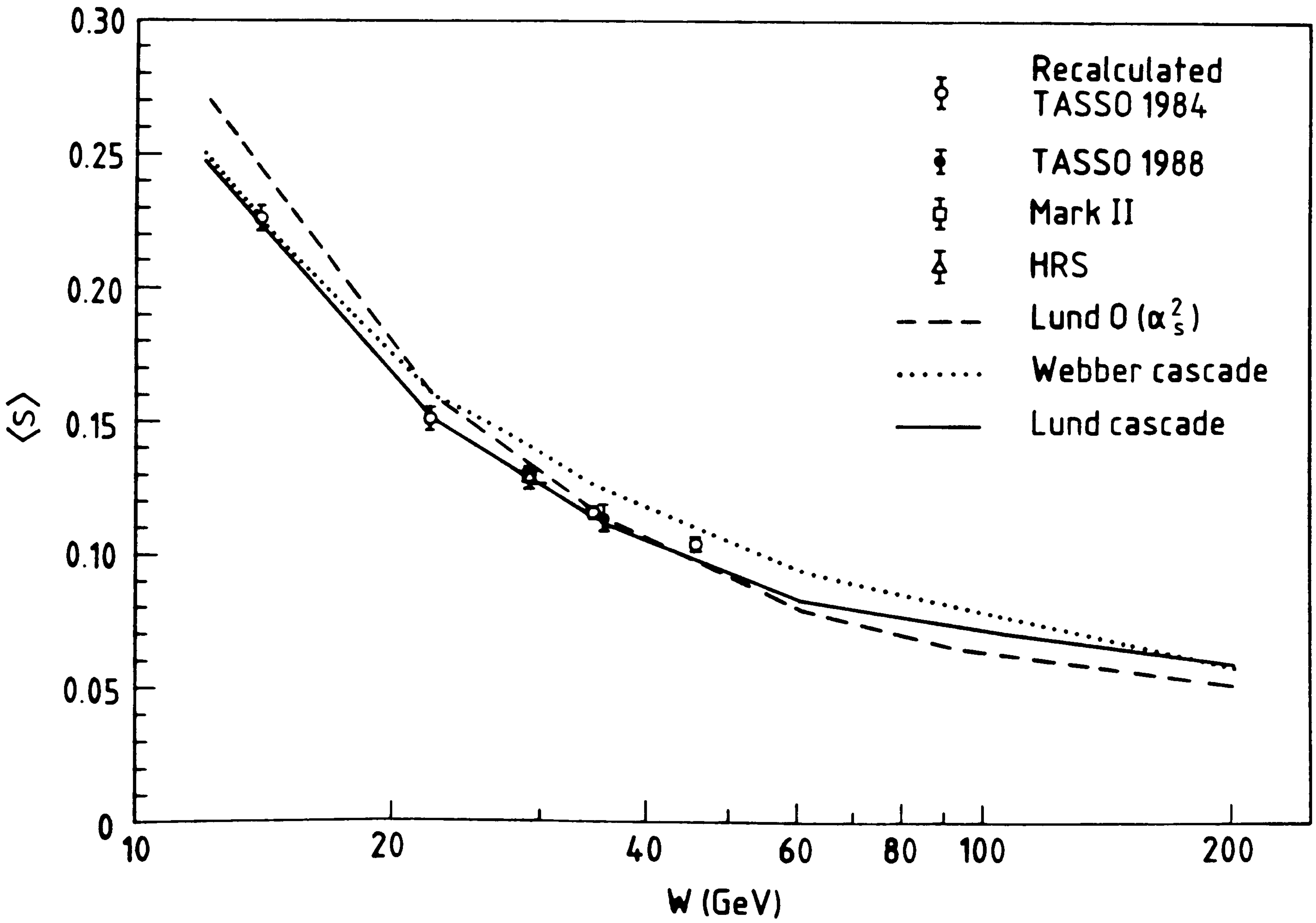

Figure 4.2: The mean sphericity as a function of W including the recalculated values for the 1984 TASSO data.

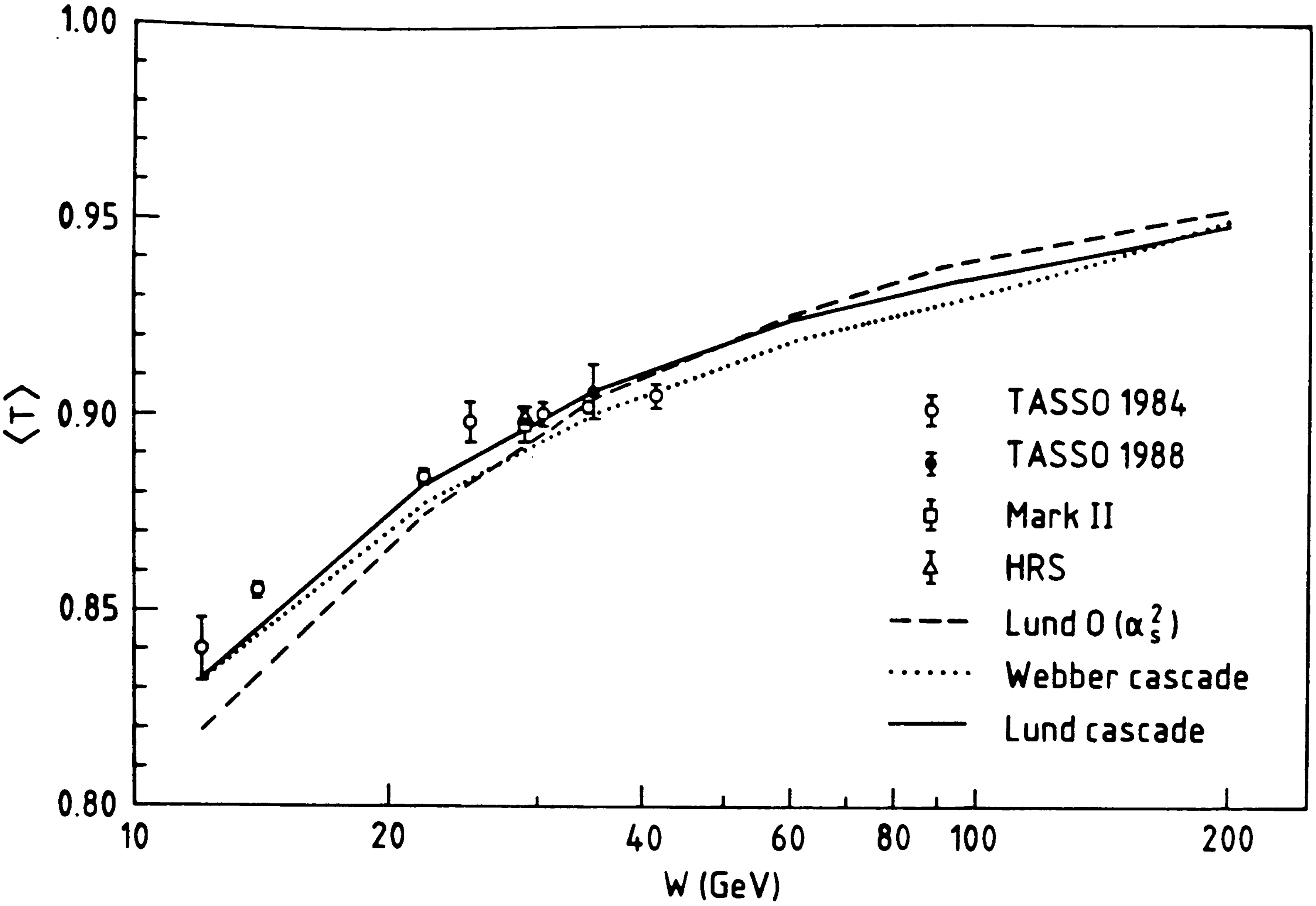

Figure 4.3: The mean thrust as a function of W.

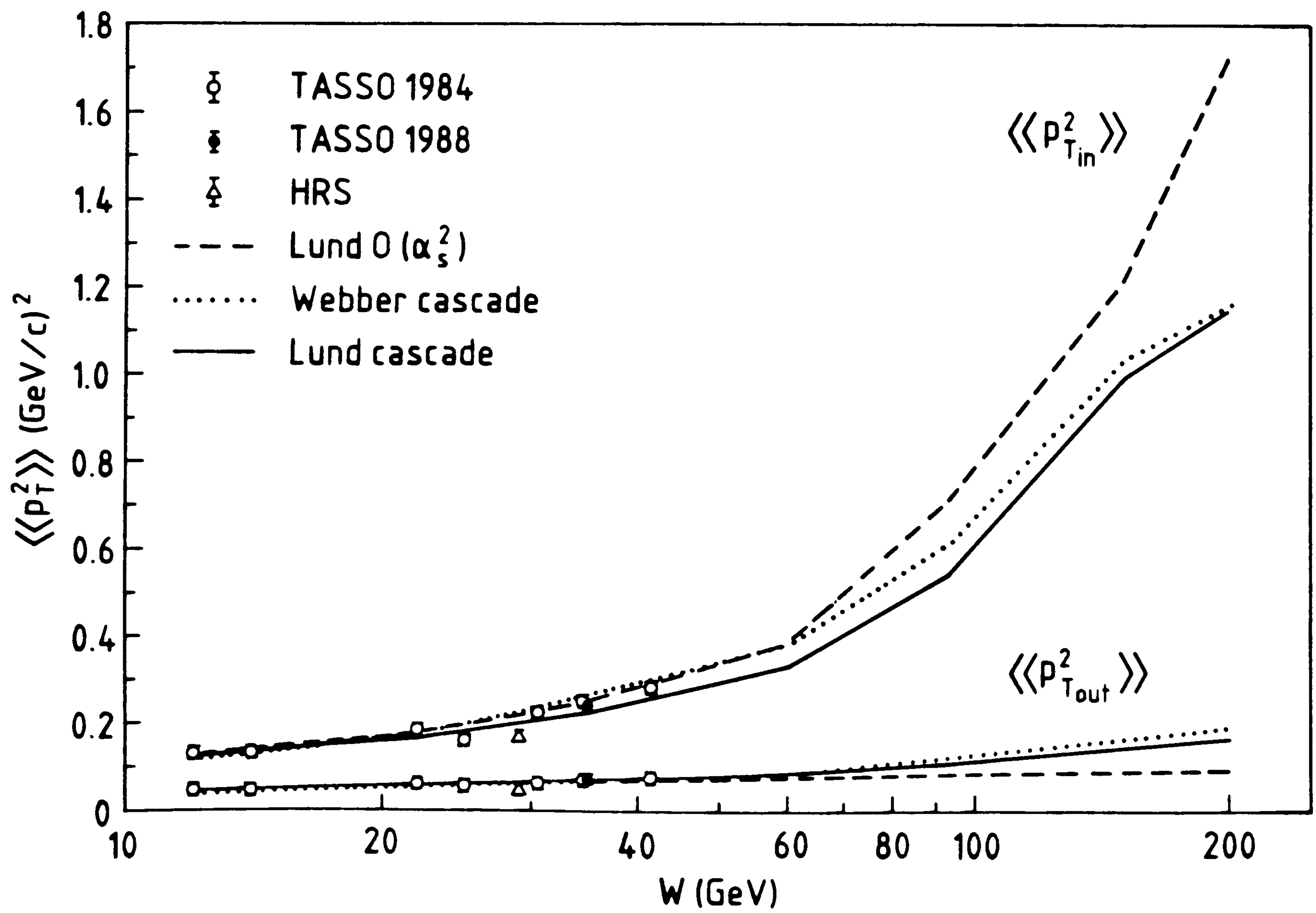

Figure 4.4: The mean $< p_{T_{in}}^2 >$ and $< p_{T_{out}}^2 >$ as a function of W.

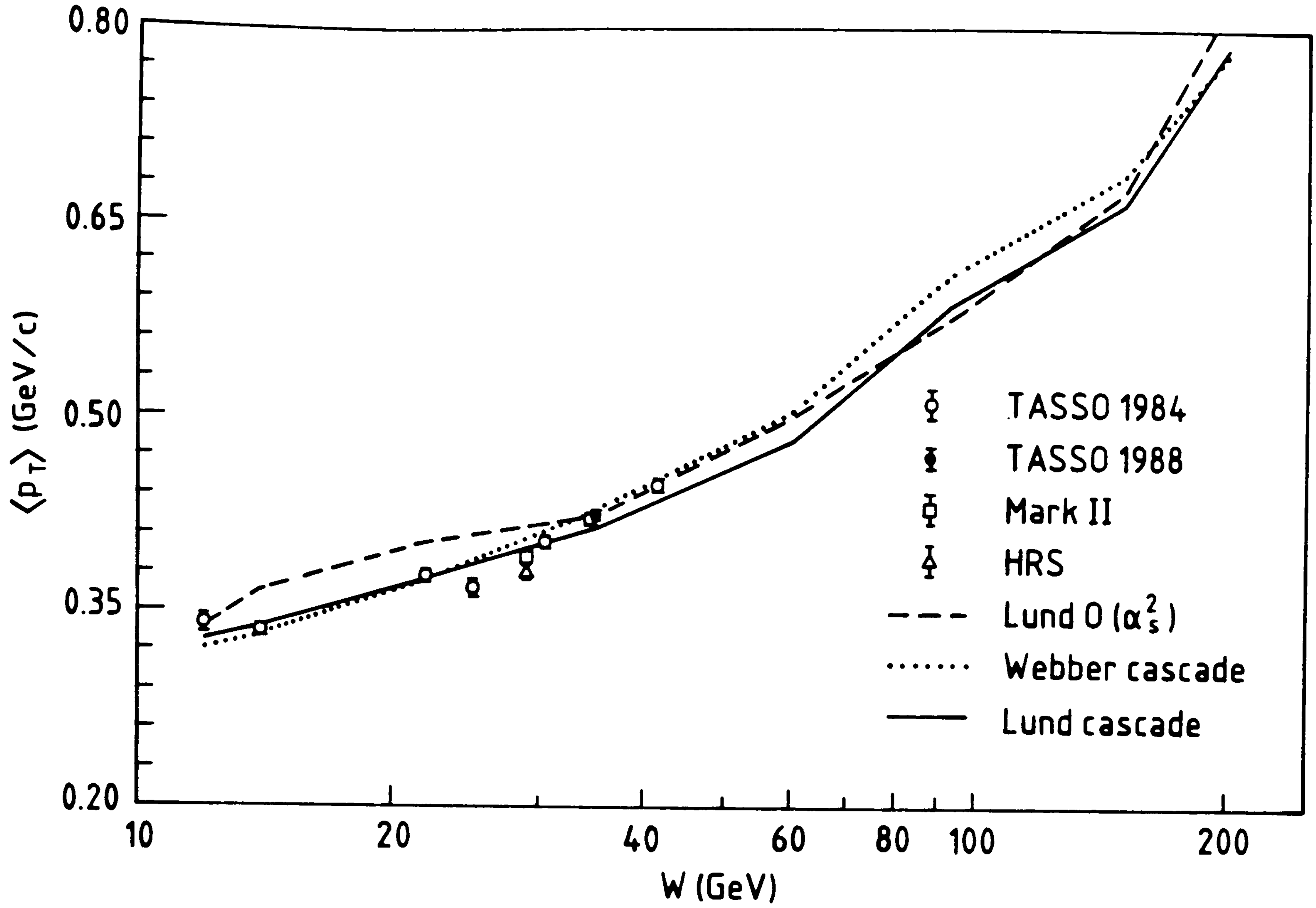

Figure 4.5: The mean charged particle p_T as a function of W.

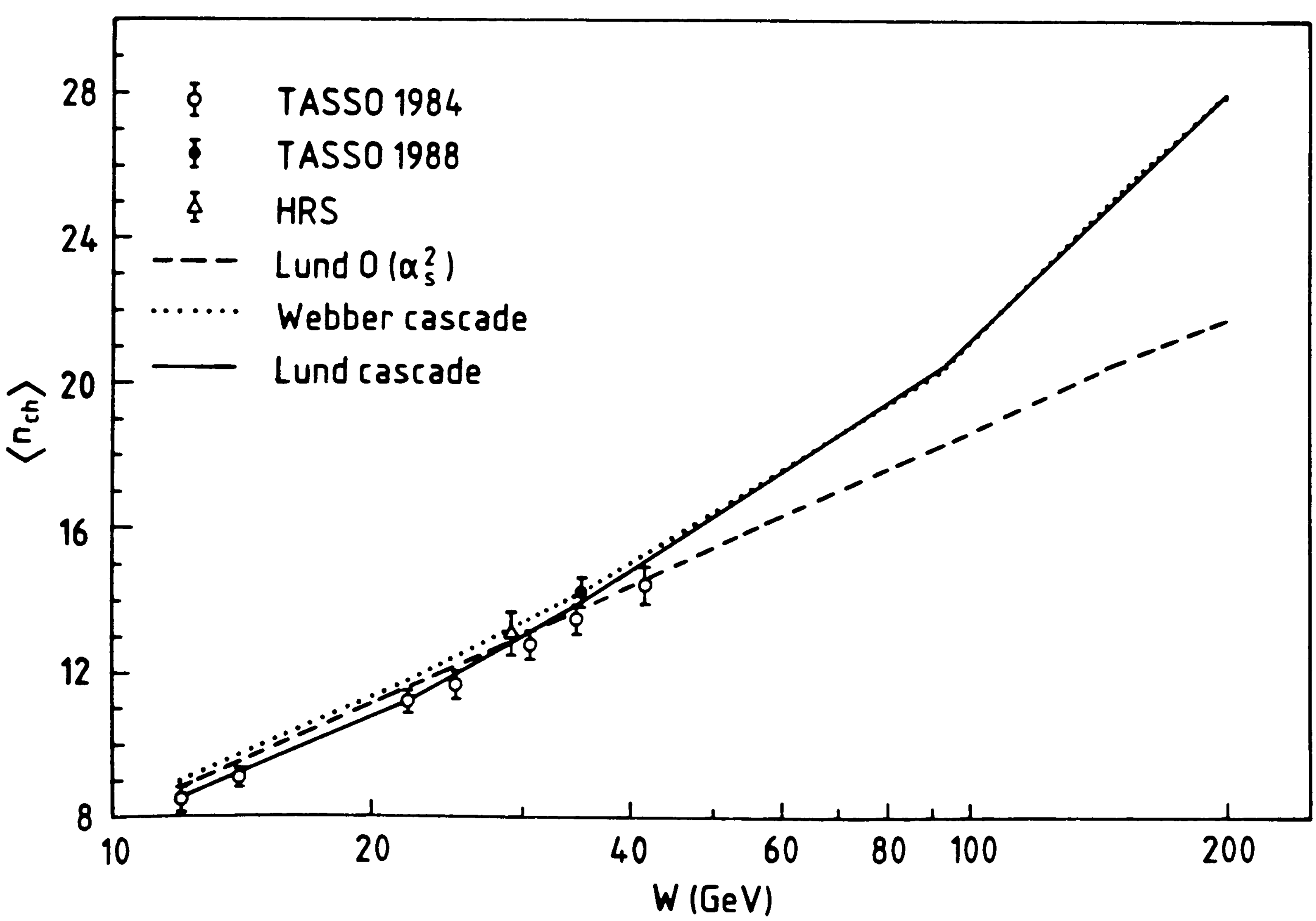

Figure 4.6: The mean charged particle multiplicity as a function of W.

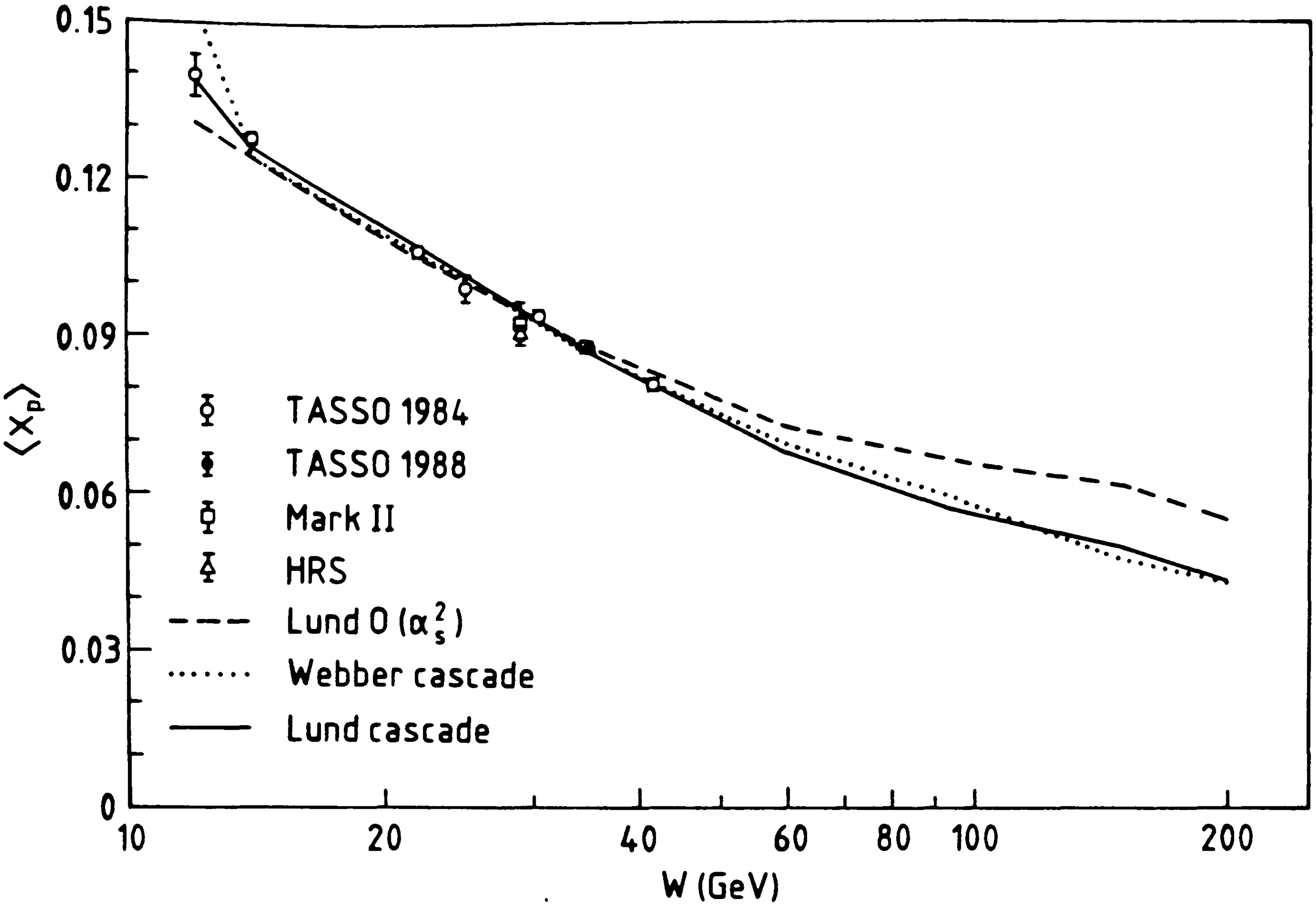

Figure 4.7: The mean charged particle x_p as a function of W.

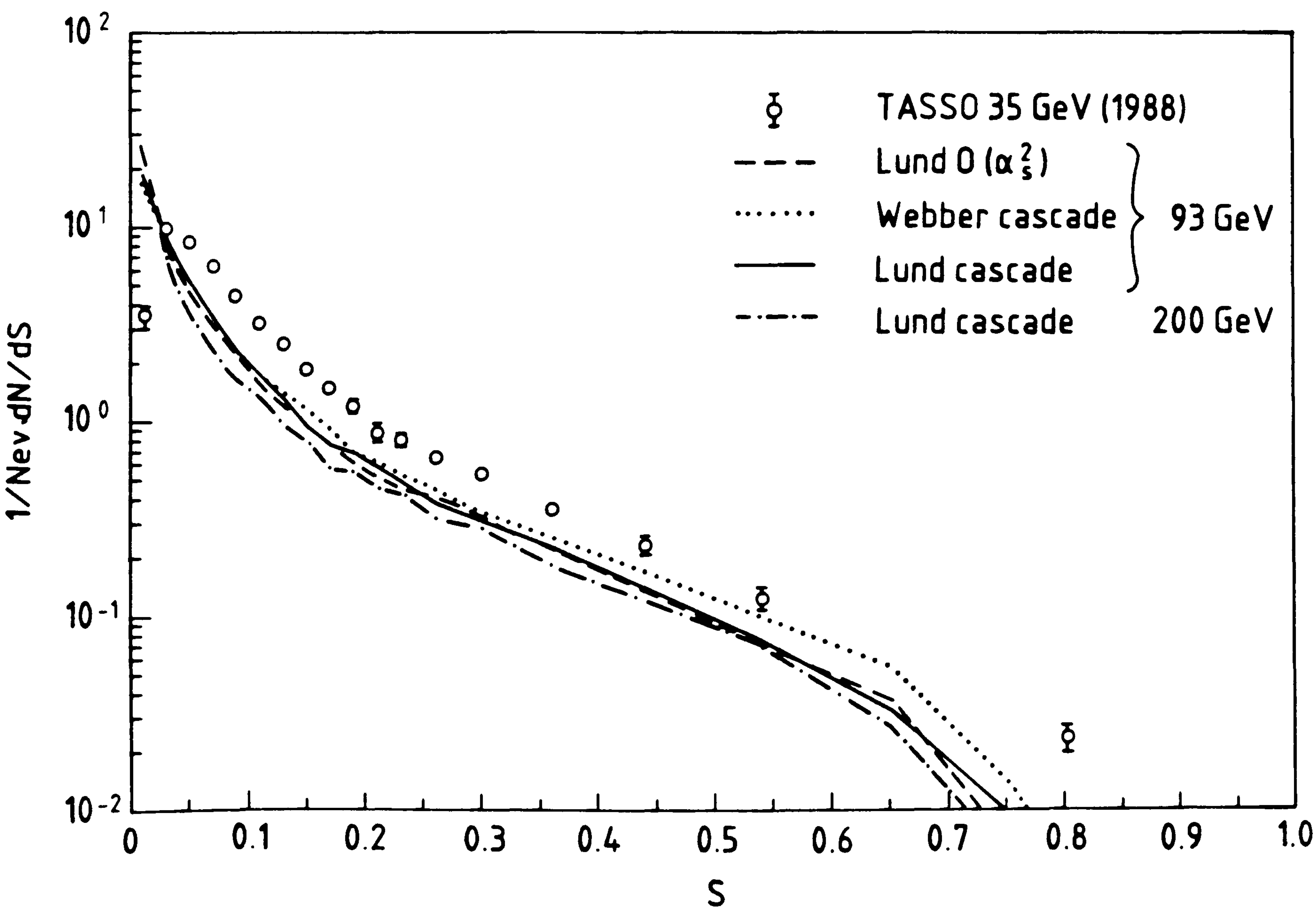

Figure 4.8: The sphericity distribution

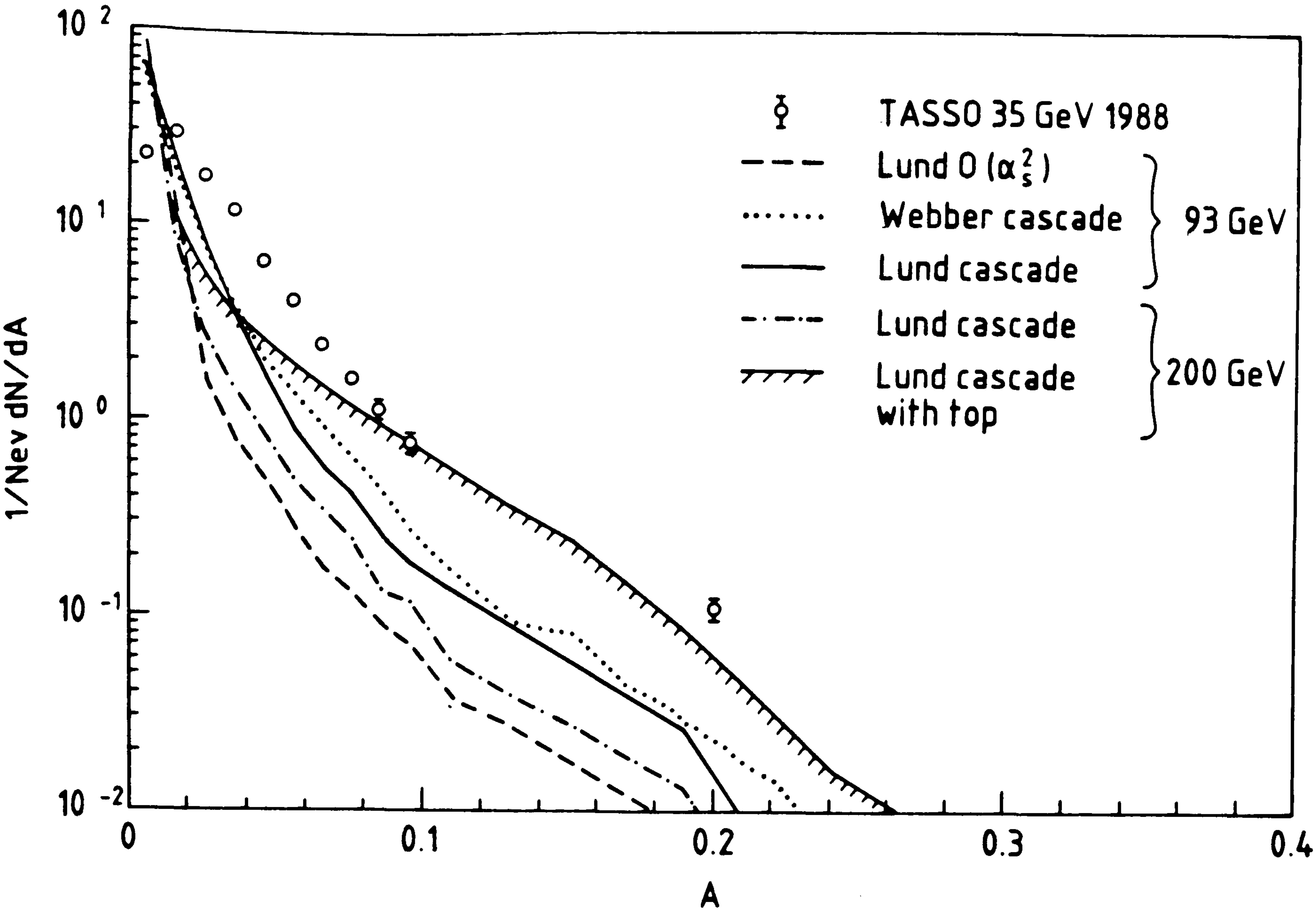

Figure 4.9: The aplanarity distribution

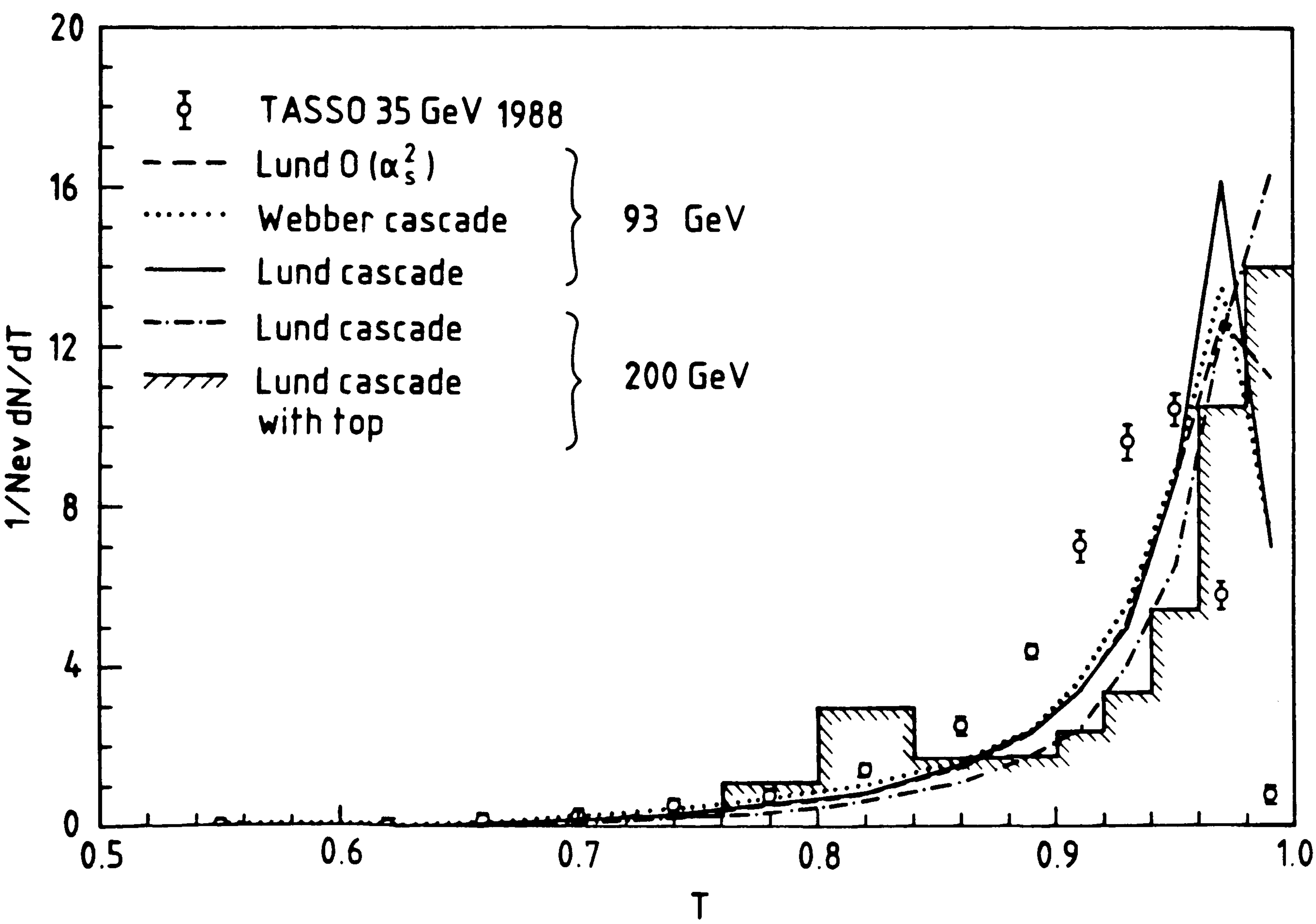

Figure 4.10: The thrust distribution

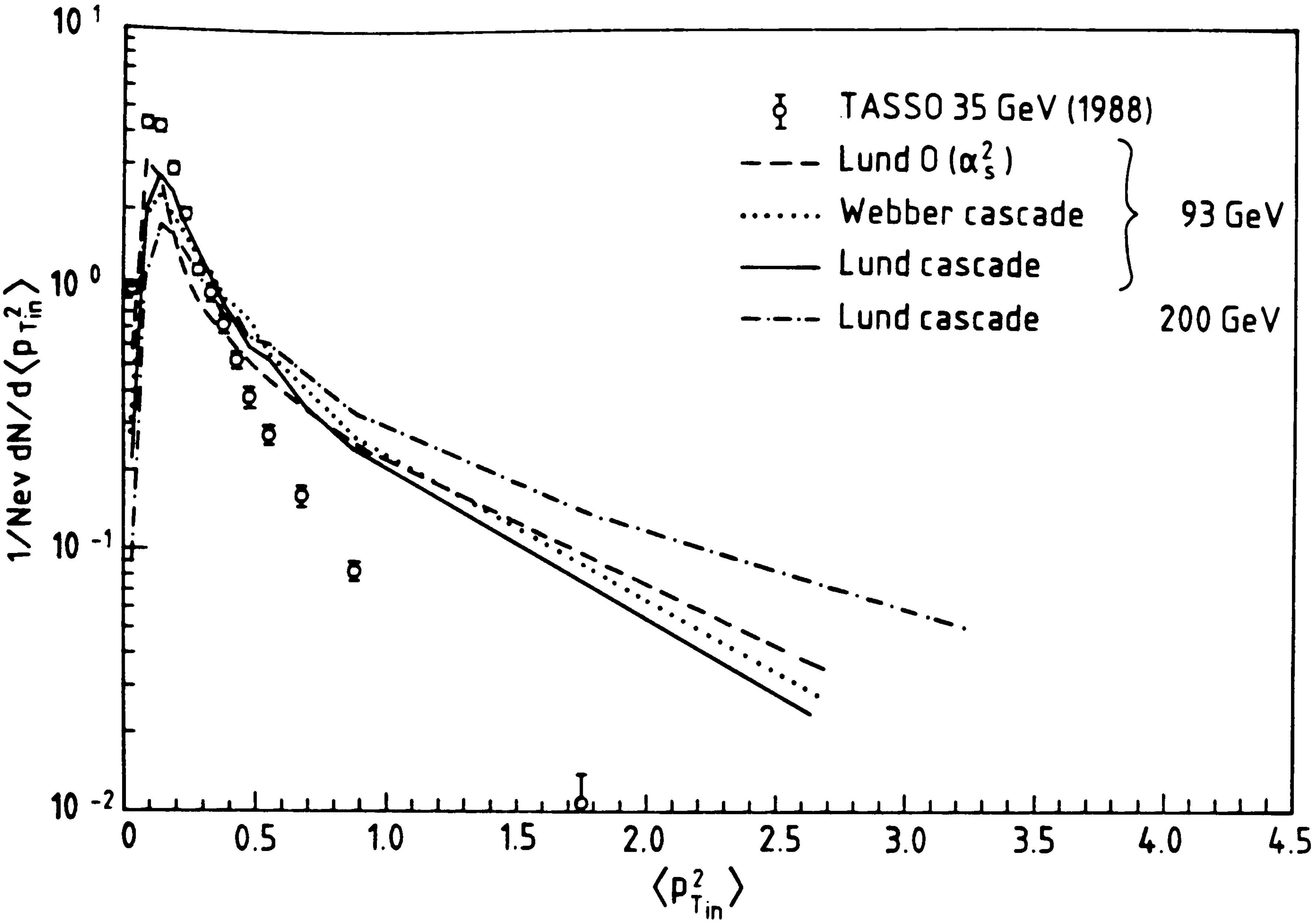

Figure 4.11: The $< p^2_{T_{in}} >$ distribution

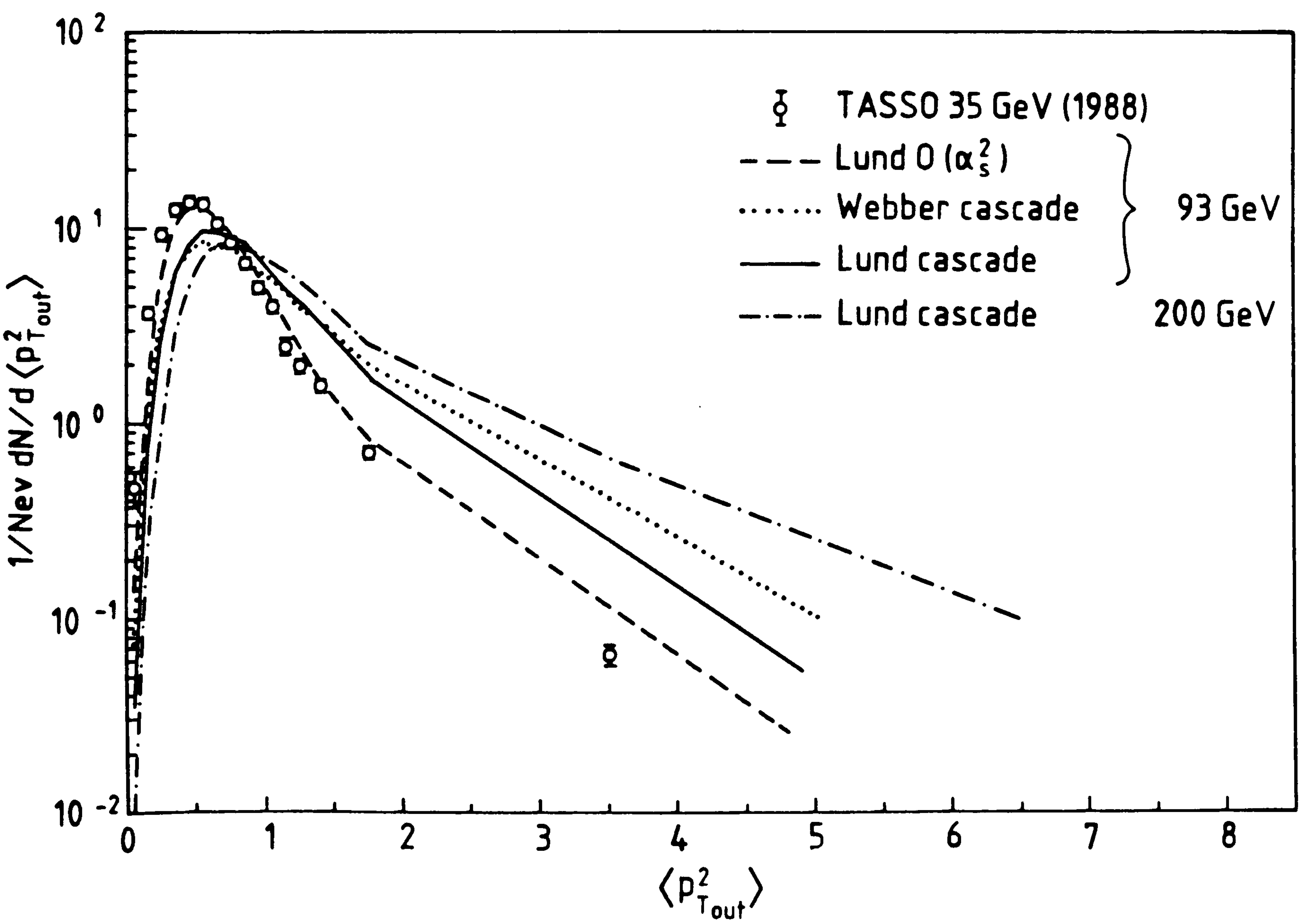

Figure 4.12: The $< p^2_{T_{out}} >$ distribution

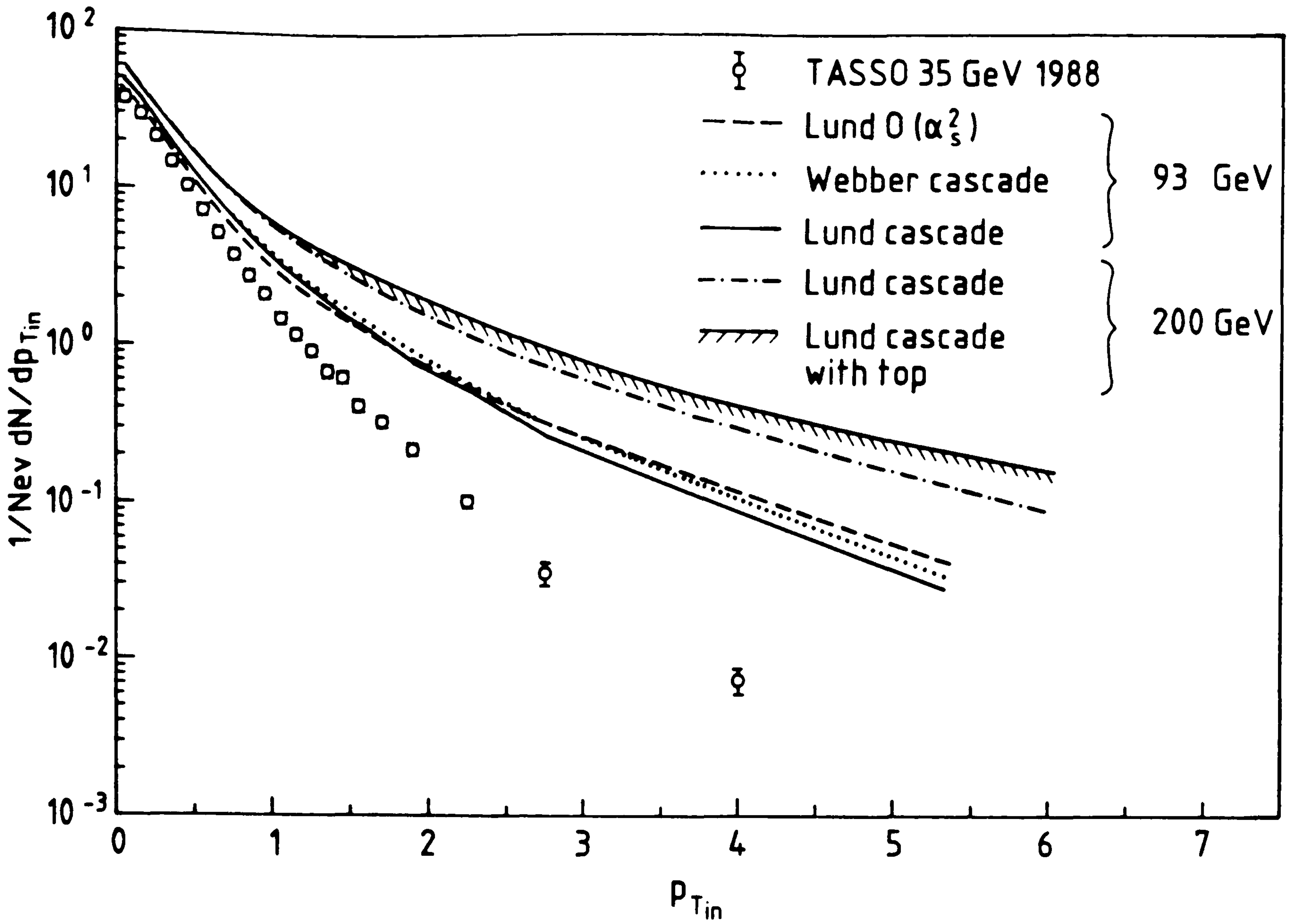

Figure 4.13: The charged particle $p_{T_{in}}$ distribution

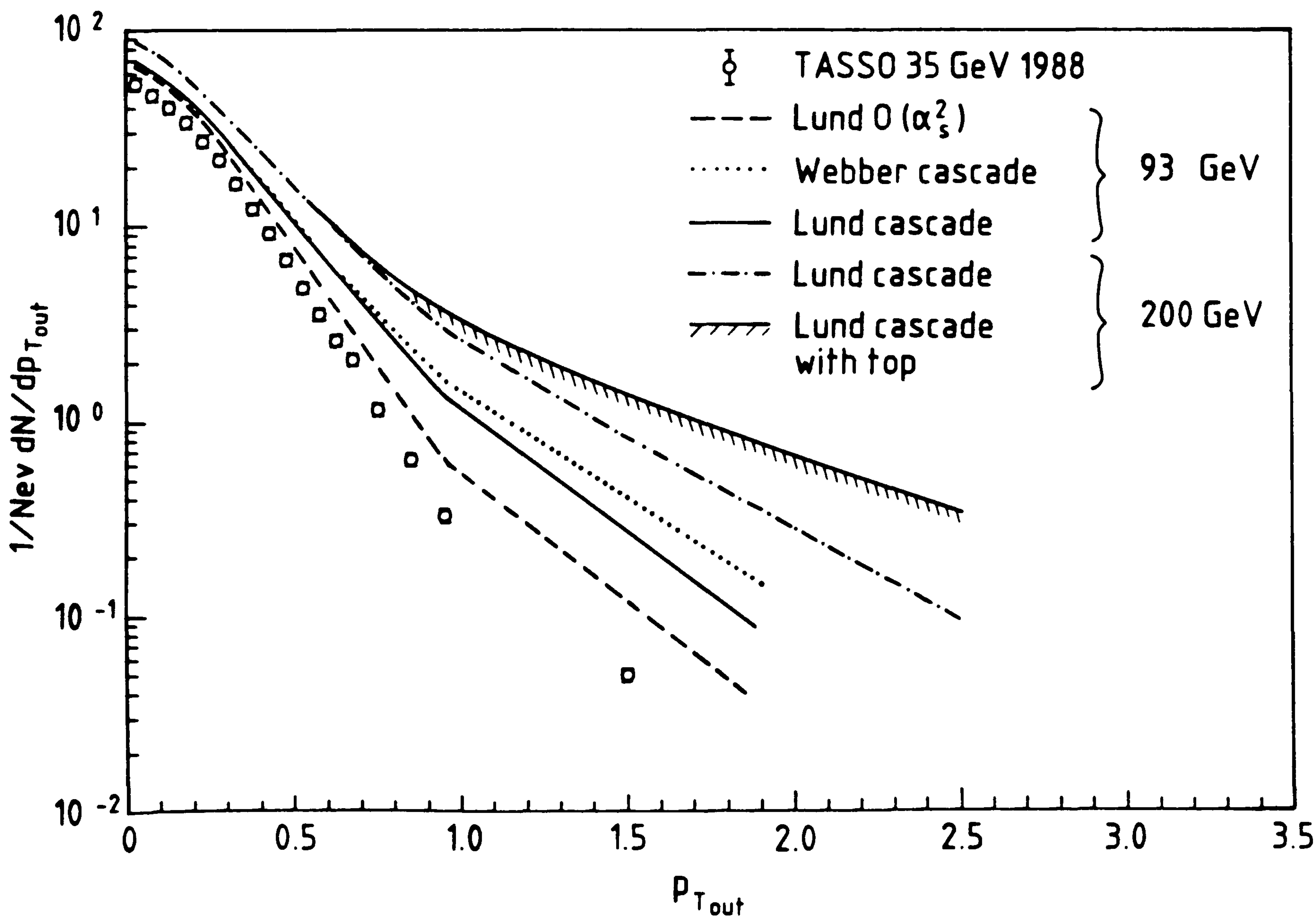

Figure 4.14: The charged particle $p_{T_{out}}$ distribution

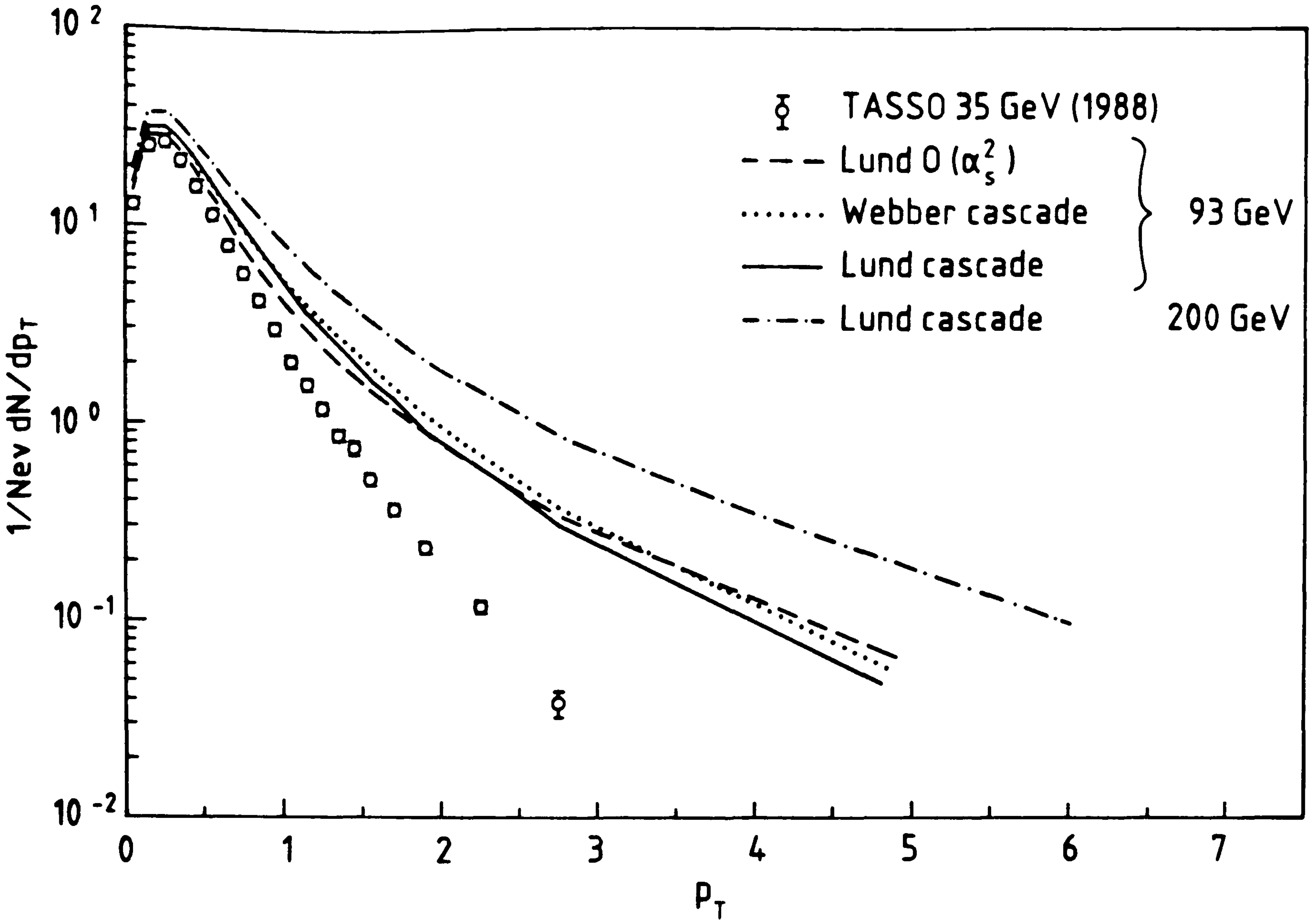

Figure 4.15: The charged particle p_T distribution

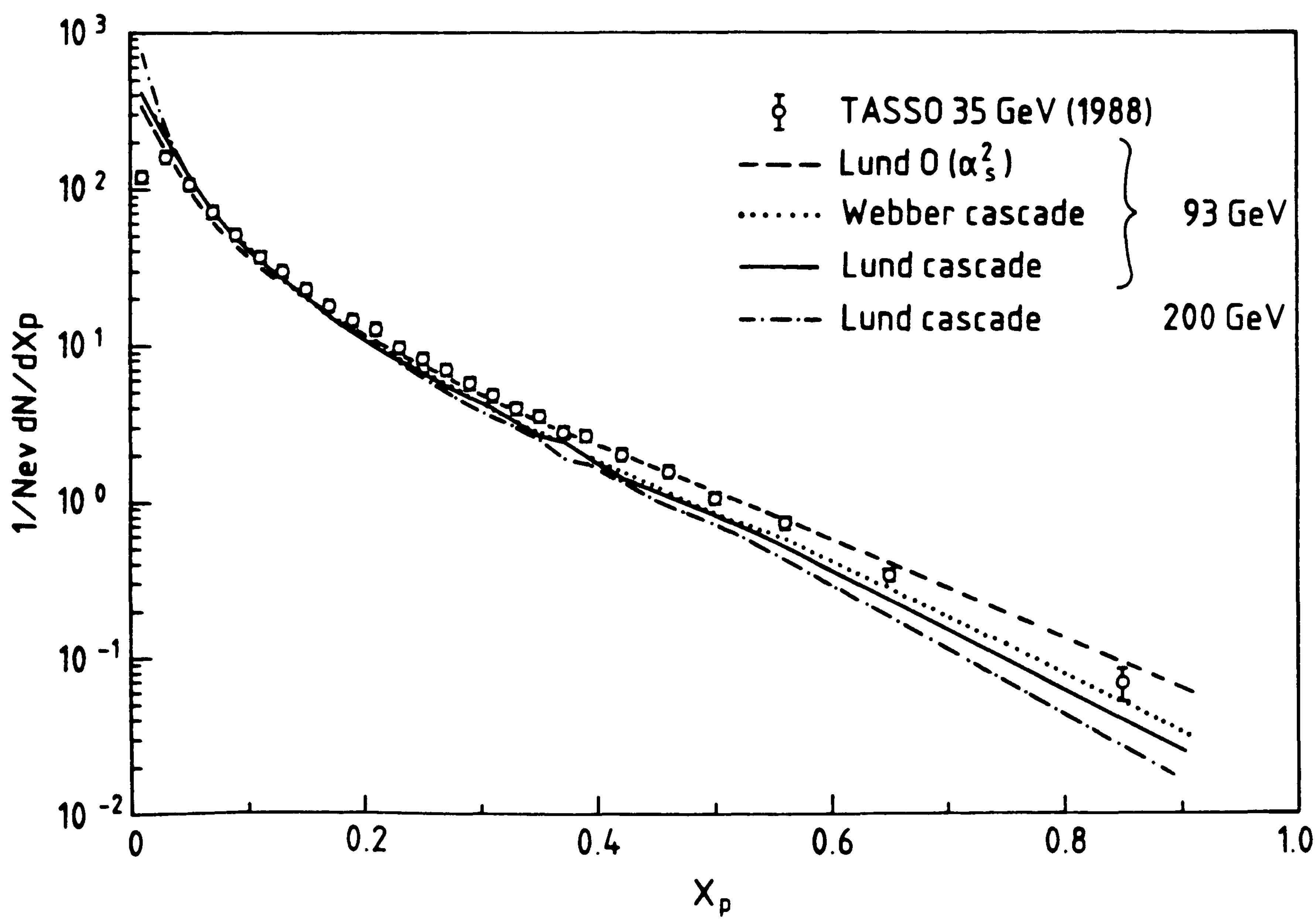

Figure 4.16: The charged particle x_p distribution

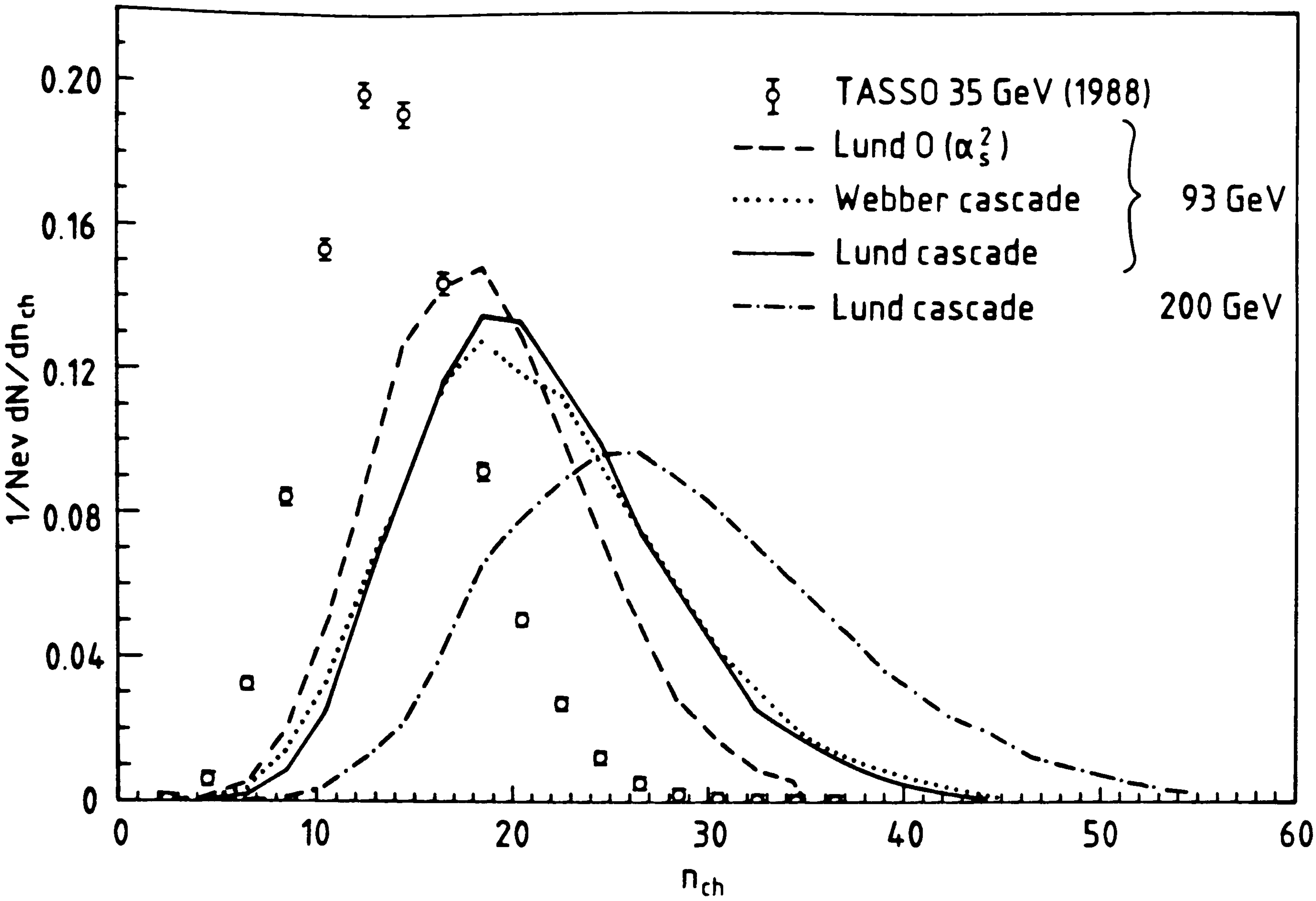

Figure 4.17: The charged particle multiplicity distribution

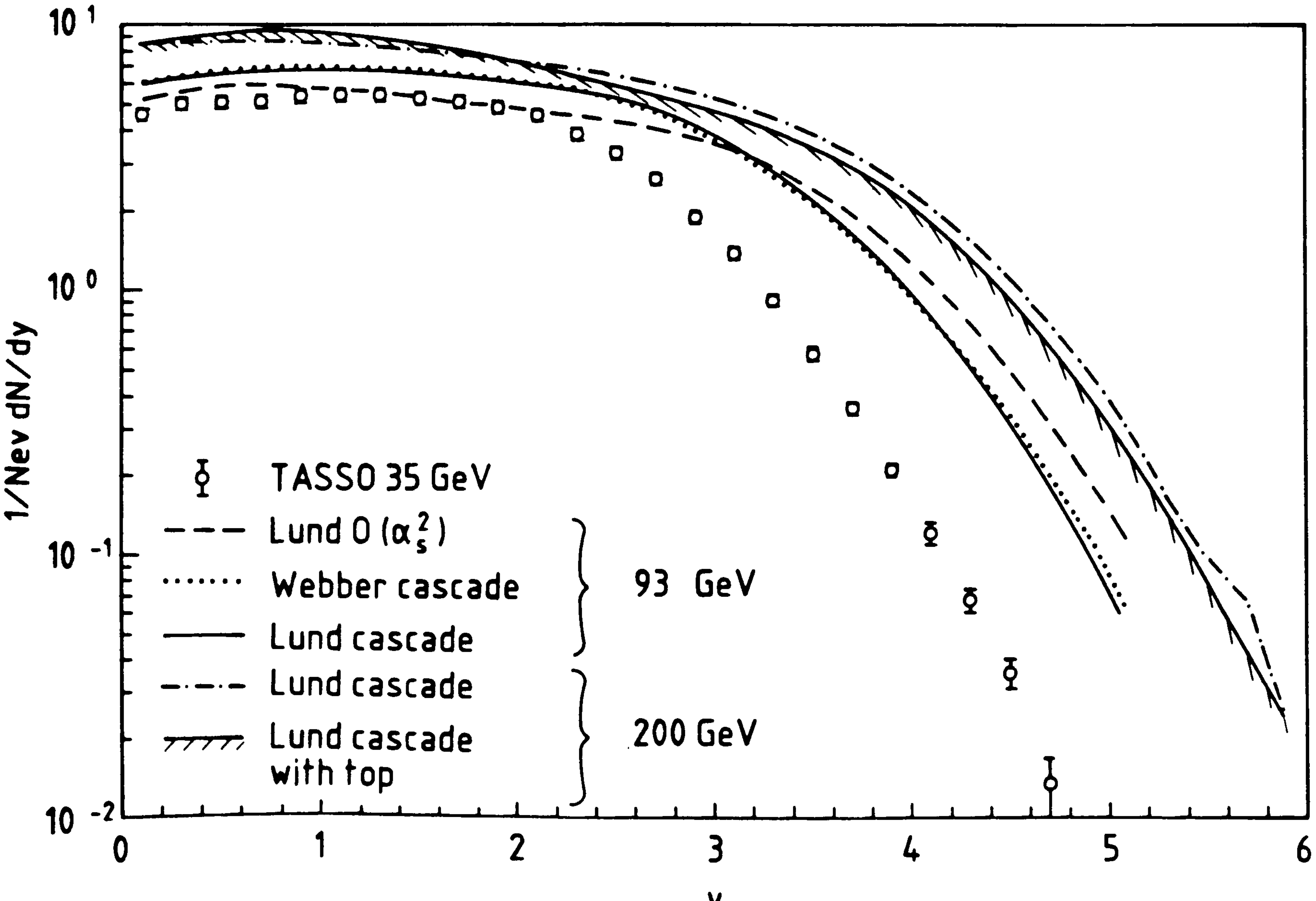

Figure 4.18: The rapidity distribution

CHAPTER 5

MULTIJET FINAL STATES IN e^+e^- ANNIHILATION

5.1 INTRODUCTION

Hadronic final states comprising two, three and four jets have been observed at PETRA (Fig. 1.2) and interpreted in terms of the production and fragmentation of up to four partons as discussed in Chapter 1, the parton-level processes being described by perturbative QCD calculations. Unfortunately there is no clear boundary between these different classes of multijet events, both from a theoretical and an experimental point of view.

Theoretically the spectrum of gluon bremsstrahlung is a continuous one ranging from hard gluons emitted at wide angles to the parent quark (or antiquark) to vanishingly soft gluons emitted collinearly with the parent quark. However, as described in Chapter 1, divergences in the finite order QCD parton-level calculations of cross sections are removed by cutoffs (*eg.* y_c) which affect the number of partons counted in the final state; the parton multiplicity in an event is therefore well-defined, but depends on the cutoff value chosen. In practice this does not matter too much, provided the cutoff is chosen to be reasonably small; the addition of one or two very soft and/or collinear partons to the final state will not affect the number of observed hadron jets, for such partons will not be resolved experimentally as separate jets because of the smearing introduced by fluctuations in the hadronisation process. Even in the language of exact finite order QCD calculations, therefore, the relationship between parton multiplicity and hadron jet multiplicity is not straightforward, as an observed hadron jet may actually correspond to a 'cluster' of a few partons which are near neighbours in phase space, and there is certainly no one-to-one correspondence between the two multiplicities.

The situation is even more confused when considering the infinite order approximate QCD calculations in the LLA, where in each event a few hard partons are accompanied by several softer ones; *eg.* at $W = 35$ GeV the mean number of partons per event is about six for the Webber LLA and Lund LLA + $O(\alpha_s)$ models[1] though ten is not uncommon. Furthermore, the number of such soft radiated partons in an event increases with W. Each hadron jet will therefore typically comprise the fragmentation products of several near-neighbour partons. It is apparent that the only meaningful way to relate the hadron jet properties to the underlying parton structure of an event is to choose some jet-defining algorithm which can be applied to both phases and then to compare the resulting parton jets and hadron jets.

It had been reported some time ago [129] that QCD calculations to $O({\alpha_s}^2)$ were unable to account for the rate of 4-jet events observed in the data, the theoretical predictions being much too low. In the only detailed study of multijet events published to date [130], it was confirmed that an $O(\alpha_s^2)$ QCD model[2] produces too few $\geq$ 4-jet-like events, whereas a LLA model[3] gives a satisfactory description of these rates. This suggests that 3^{rd} (and higher) order terms in perturbative QCD already make a significant contribution to the 4-jet cross-section at PETRA energies[4]. However, the LLA model was not able to account for the observed rate of hard 3-jet events, presumably because of the inherent approximations in the LLA formalism discussed in Section 1.5.

These issues are further investigated here[5]. The data are analysed in terms of

---

[1] This number is for the parameter values given in Tables 3.3b and 3.3c; the exact number clearly depends on the values of Λ and Q_0.

[2] The GKS parton-level calculations with Lund string fragmentation included in JETSET version 5.2 [131].

[3] The Webber LLA model with cluster hadronisation, BIGWIG version 4.2 [54].

[4] The recent calculation of the total hadronic cross section to $O({\alpha_s}^3)$ [26] suggests that the $O({\alpha_s}^3)$ terms themselves are larger than the terms of $O({\alpha_s}^2)$ (Section 1.2).

[5] See also [132].

explicit multijet states rather than the global event characteristics discussed earlier, and compared with the predictions of the three latest and most successful perturbative QCD + fragmentation models described in Chapter 1:

(i) The 2^{nd} order perturbative QCD calculations of Gutbrod, Kramer and Schierholz (GKS) [41] incorporated into the Lund Monte Carlo, version 6.3 [49]. This is referred to as the '$O(\alpha_s^2)$ model'.

(ii) The LLA cascade model [54], which includes soft gluon interference effects, incorporated into the Monte Carlo program BIGWIG version 4.2. This is referred to as the 'LLA model'.

(iii) The LLA cascade model (with soft gluon interference) containing the $O(\alpha_s)$ matrix element factor [69], also incorporated into version 6.3 of the Lund Monte Carlo. This is referred to as the 'LLA + $O(\alpha_s)$ model'.

In cases (i),(iii) hadronisation according to the Lund string model [50] is employed, whereas in (ii) hadronisation is via the formation and decay of colourless clusters [54].

The event selection criteria are given in Section 5.2 and the choice of jet algorithm is discussed in Section 5.3. The jet rates in the data are compared with the model calculations at $W = 35$ GeV in Sections 5.4 and 5.5, with the relationship between the jets and the underlying parton structure being discussed in Section 5.6. The energy evolution of the jet rates is given in section 5.7 and the Q^2 dependence of α_s is investigated in Section 5.8. Section 5.9 forms a summary and conclusions of the results presented in this chapter.

5.2 EVENT SELECTION

In addition to the usual hadronic selection criteria (Section 2.5) for e^+e^-annihilation events based upon the information on charged particle momenta measured in the central detector, for the multijet analysis three further cuts [97] were made: (a) events were removed for which the sum of the particle momenta $\sum|\mathbf{p}|$ exceeded $2W$; this excluded events containing spurious high momentum tracks (see Section 3.5); (b) in order to ensure that events were well-contained within the acceptance of the detector the angle θ_s between the sphericity axis and the beam direction was required to satisfy $|\cos\theta_s| < 0.85$;

(c) the angle θ_N between the normal to the event plane and the beam direction had to satisfy $|\cos\theta_N| > 0.1$ in order to reject badly reconstructed events and events with a hard photon radiated from the e^+ or e^-. The numbers of hadronic events before and after these cuts are shown in Table 5.1.

Table 5.1: Number of hadronic events used in jet analysis

$< W >$ (GeV)	N^0 of hadronic events	N^0 used in jet analysis
14.0	2999	2757
22.0	1914	1730
35.0	31176	27178
43.8	6380	5261

All the QCD model Monte Carlo events, generated with the tuned parameter sets of Section 3.6 and with initial state radiative effects included, were put through the TASSO detector simulation program and underwent the same hadronic selection and analysis cuts as applied to the data.

5.3 THE JET ALGORITHM

There are various procedures and algorithms available for reconstructing jets from hadronic events (see [23] for a comprehensive discussion). In many cases the number of jets required must first be specified, then the event division proceeds by optimising a chosen event variable, *eg.* minimising transverse, or maximising longitudinal, momentum (or various powers thereof) relative to jet axes to be determined.

5.3.1 The Lund Algorithm 'LUCLUS'

A popular algorithm is the routine LUCLUS [131] available in the Lund JETSET program. The 'distance' d_{ij}:

$$d_{ij}^2 = \frac{1}{2}(p_i p_j - \mathbf{p_i} \cdot \mathbf{p_j}) \frac{4 p_i p_j}{(p_i + p_j)^2}$$

$$i.e. \qquad d_{ij}^2 = \frac{4p_i^2\, p_j^2 \sin^2(\theta_{ij}/2)}{(p_i + p_j)^2}$$

is formed for every pair of particles in an event, the pair with the smallest d_{ij} being combined into a 'pseudoparticle' by adding their momentum 4-vectors. The procedure is repeated, the pair with the lowest d_{ij} being combined each time, until all remaining pairs of particles/pseudoparticles have distances which satisfy:

$$d_{ij} > d_{join}$$

where d_{join} is a jet resolution parameter. The resulting number of particles or pseudoparticles is called the jet multiplicity of the event. Note that there is no *a priori* specification of the number of jets to be found*, and that every charged particle belongs to a single jet.

This algorithm was applied to the 1986 $W = 35$ GeV data and to samples of 70000 Monte Carlo events. The resulting rates of n-jet events are shown in Fig. 5.1 as a function of the jet resolution parameter d_{join}. None of the models describes the 2,3 or 4-jet rates, but they seem to do very well with the 1-jet rate! Note however that at the Lund recommended value of $d_{join} = 2.50$, the 1-jet rate is roughly 3%. This value is astonishingly high, given that 1-jet events should not occur at all, except where there has been a hard photon radiated by the e^+ or e^-, or there have been substantial particle losses in 2-jet events due to undetected neutral particles, the limited detector acceptance or inefficiency in detecting charged particles. The only possible source of *bona fide* 1-jet hadronic events is the background from two-photon events, which has not been subtracted here. At most such events should account for 0.9% of the total (Table 3.1), though the cuts described in Section 5.2 reduce the percentage contamination. It is inconceivable, therefore, that two-photon events could account for a 3% rate of 1-jet events, and the model calculations, which agree with the data, do not include this source anyway.

One relevant factor to bear in mind is that the event visible energy E_{vis} for the

---

* The *minimum* number of jets to be found can be specified, though this option is not used here.

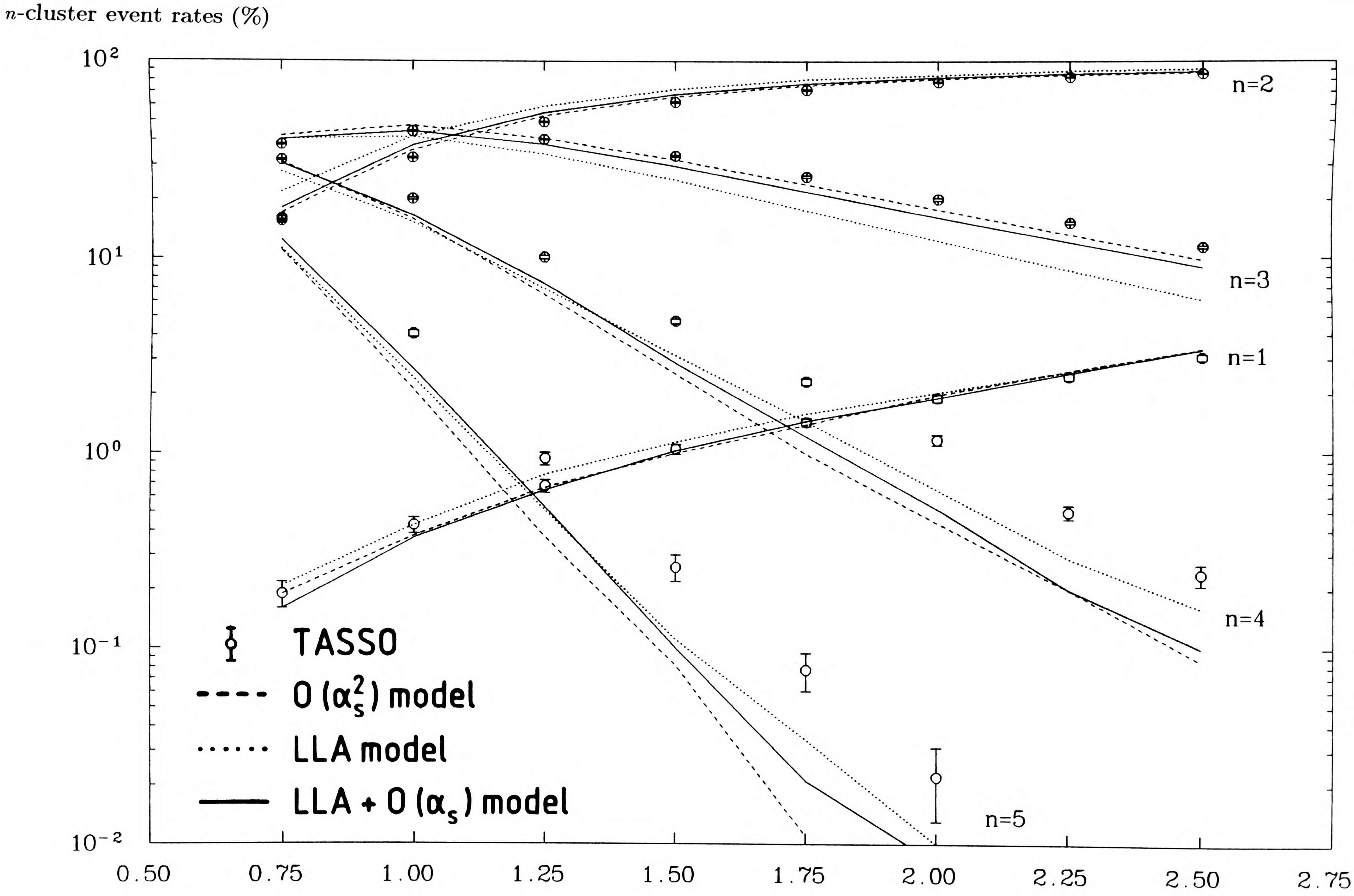

Figure 5.1: The n-jet event rates (%), defined using the LUCLUS algorithm, as a function of the jet resolution parameter d_{join}.

Monte Carlo calculations seems to be underestimated compared with that for the real data (Table 5.2).

Table 5.2: Mean event visible energy for data and Monte carlo

	$< E_{vis} >$ (GeV)
Data	19.1 ± 0.1
$O(\alpha_s{}^2)$ MC	17.5 ± 0.1
LLA MC	17.4 ± 0.1
LLA + $O(\alpha_s)$ MC	17.7 ± 0.1

In principle this could be due to the event generators themselves, though the fact that all three generators agree with one another suggests that the problem lies with the simulation of the detector effects. One obvious possibility to account for the discrepancy is that the data have been MILLed, whereas the model calculations are for SIMPLE simulation of charged tracks, the amount of computer processing time needed to MILL the events generated for all three models being prohibitive. It is known (Section 3.5) that MILL tends to increase artificially the population of high x_p tracks, thereby increasing the visible energy. This effect was investigated using the sample of MILLed LLA + $O(\alpha_s)$ model events generated for the data correction (Section 3.7) and the results are shown in Table 5.3 for the 'middle of the range' value $d_{join} = 1.5$.

Table 5.3: Rate of n-jet events (%): LUCLUS, $d_{join} = 1.5$

	$< E_{vis} >$ (GeV)	1	2	3	4	≥ 5
SIMPLE	17.7 ± 0.1	1.03 ± 0.05	67.0 ± 0.4	29.0 ± 0.3	2.88 ± 0.08	0.10 ± 0.02
MILLed SIMPLE	18.8	0.95	64.4	31.0	3.66	0.18

Note that the generated events are the **same** for both cases. The visible energy is clearly increased by MILLing to be in agreement with that for the data; the normalisation of all the jet rates is also brought into much closer agreement with the data.

It is clear that the LUCLUS algorithm is rather sensitive to the fine details of the tracking simulation. This is perhaps not surprising, as it works directly with particle momenta, measured by the track curvature. Furthermore, the resolution criterion d_{join} is not scaled to take into account the large event-by-event fluctuations in the visible energy due to initial state bremsstrahlung and undetected particles, which therefore affect the reconstructed jet multiplicity on an event-by-event basis. Because of these problems a second algorithm was investigated.

5.3.2 The JADE Algorithm 'JCLUST'

An appealing jet-finding algorithm has been used by the JADE collaboration in a similar analysis of their hadronic data [22,130]. We used an algorithm which operates under the same principles:

The invariant mass-squared m^2_{ij} is calculated for all pairs of charged particles i, j in an event according to the formula:

$$m^2_{ij} \quad = \quad 2E_iE_j(1 - \cos\theta_{ij})$$

where in calculating the energy all particles are assumed to have the charged pion mass. The pair with the lowest m^2 are combined into a 'pseudoparticle' by adding their momentum 4-vectors. The procedure is repeated, the pair with the lowest m^2 being combined each time, until all remaining pairs of particles/pseudoparticles have invariant masses which satisfy:

$$m^2_{ij} \quad > \quad m^{cut\,2}_{ij} \quad = \quad y_cE^2$$

where y_c is a jet resolution parameter. For our analysis using only charged particles E = E_{vis} was used, E_{vis} being the visible energy of the event. The resulting number of particles/pseudoparticles is called the cluster or jet multiplicity of the event.

This algorithm is clearly very similar to LUCLUS in its basic idea of forming clusters of particles, except that the 'distance' between particle pairs, d_{ij}, is replaced by the invariant mass of particle pairs, m_{ij}, but scaled so as to take into account the event-by-event fluctuations in the visible energy; the parameter y_c therefore corresponds to d_{join}. Again, there is no *a priori* specification of the number of clusters to be found, and every charged particle belongs to a single cluster.

The 'correct' definition of m_{ij}^2, taking explicit particle mass terms into account, is impossible to use here because of the limited particle identification capability of the TASSO detector. One can use this definition by assigning all particles the pion mass, but this tends to increase the value of m_{ij}^2 relative to the massless case, so that more low energy jets are separately resolved, which are essentially spurious and arise from hadronisation fluctuations. In Monte Carlo studies using the $O(\alpha_s^2)$ model, the above expression for m_{ij}^2 neglecting all particle masses was found to provide the best agreement between the cluster multiplicity reconstructed from final state charged particles and the initial parton multiplicity for the *same* values of y_c and y_{min}, the experimental jet-resolution parameter and the QCD (massless) parton resolution parameter used in the matrix element calculations*, respectively.

The jet rates were produced for $y_c = 0.04$ using both SIMPLE and MILLed SIMPLE tracks and are shown in Table 5.4. ($y_c = 0.04$ is the 'middle of the range' value and gives roughly similar jet rates to $d_{join} = 1.5$).

Table 5.4: Rate of n-jet events (%): JCLUST, $y_c = 0.04$

	$< E_{vis} >$ (GeV)	1	2	3	4	≥ 5
SIMPLE	17.7 ± 0.1	0.16 ± 0.02	55.6 ± 0.4	40.6 ± 0.3	3.64 ± 0.09	0.025 ± 0.008
MILLed SIMPLE	18.8	0.17	55.4	40.6	3.77	0.030

There is essentially no change in the jet rates for the two cases; any differences are well within the statistical errors for the sample of events used. Furthermore, the rate of 1-jet events is much more in line with what is expected. JCLUST is hence relatively robust with respect to the details of the tracking simulation, and is therefore a much safer algorithm to use.

* Unless stated otherwise, the value of y_{min} used throughout this analysis was 0.02.

5.4 JET RATES AT $\sqrt{s} = 35$ GeV

Shown in Figure 5.2 are the rates of 2, 3, 4, ≥ 5 * -jet events for the data and QCD models, as reproduced by JCLUST, at 35 GeV c.m. energy as a function of the jet resolution parameter y_c; the data are also given in Table 5.5; the errors are statistical only. SIMPLE tracks were used for the model calculations.

Table 5.5: Rates of n-jet events (%) for the data at W = 35 GeV

y_c	2	3	4	≥ 5
0.02	29.7 ± 0.3	51.2 ± 0.4	17.3 ± 0.3	1.65 ± 0.09
0.03	44.0 ± 0.4	47.4 ± 0.4	8.14 ± 0.17	0.27 ± 0.03
0.04	54.7 ± 0.5	41.1 ± 0.4	3.96 ± 0.12	0.04 ± 0.01
0.05	62.8 ± 0.5	35.0 ± 0.4	1.86 ± 0.08	0.011 ± 0.006
0.06	69.4 ± 0.5	29.4 ± 0.3	0.91 ± 0.06	-
0.07	74.6 ± 0.5	24.5 ± 0.3	0.46 ± 0.04	-
0.08	78.8 ± 0.5	20.5 ± 0.3	0.24 ± 0.03	-

Taking E = 35 GeV, the cluster-pair-mass cutoff range spanned by $0.02 \leq y_c \leq 0.08$ is $4.9 \leq m_{ij}^{cut} \leq 9.9$ GeV/c^2.

The O(α_s^2) model gives a satisfactory description of the 2- and 3-jet rates, though at low y_c it slightly underestimates the rate of 2-, and overestimates the rate of 3-, jets seen in the data. The LLA model gives too many 2-, and too few 3-, jets for all y_c. The LLA + O(α_s) model matches the 2- and 3-jet rates of the data extremely well; it gives a comparable or better description than the O(α_s^2) model across the whole y_c range. This model also describes the rates of 4- and 5-jets well, as does the LLA model, whilst the O(α_s^2) model shows a serious deficiency.

Such is the large number of events in the data sample that for many of the data points the statistical errors are smaller than the size of the symbols used in Figure 5.2; together with the logarithmic scale this masks discrepancies between the data and MC at the level of a few per cent for the 2- and 3-jet cases. As an illustration, we show in

* The largest rate of > 5-jets in the data, at y_c=0.02, is about 5% of that of 5-jets; hence the > 5- is always added to the 5-jet rate

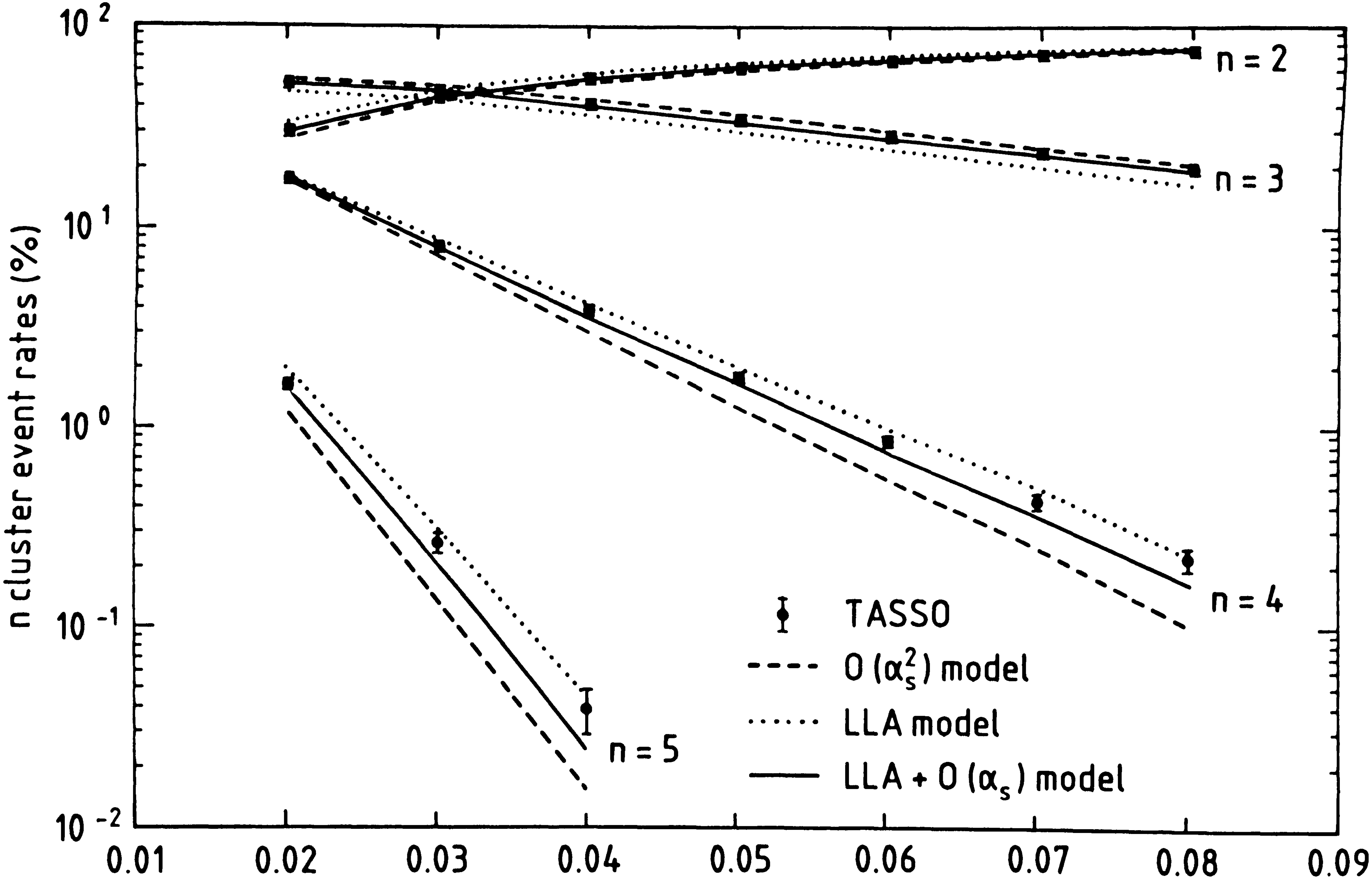

Figure 5.2: The n-jet event rates (%), defined using the JCLUST algorithm, as a function of the jet resolution parameter y_c.

Table 5.6 the jet rates at y_c=0.04, which corresponds to a cluster-pair-mass cutoff value of 7 GeV/c^2 taking E = 35 GeV.

Table 5.6: The jet rates (%) observed in the data and for the three QCD models at W = 35 GeV and y_c = 0.04

	Data	LLA + O(α_s) model	LLA model	O(α_s^2) model
2-jet	54.7 $\pm$ 0.5	55.6 $\pm$ 0.4	58.6 $\pm$ 0.4	53.1 $\pm$ 0.4
3-jet	41.1 $\pm$ 0.4	40.6 $\pm$ 0.3	36.9 $\pm$ 0.3	43.6 $\pm$ 0.3
$\geq$ 4-jet	4.00 $\pm$ 0.12	3.67 $\pm$ 0.09	4.34 $\pm$ 0.10	3.11 $\pm$ 0.08
$\frac{\geq 4-\text{jet}}{3-\text{jet}}$	0.097 $\pm$ 0.003	0.090 $\pm$ 0.002	0.118 $\pm$ 0.003	0.071 $\pm$ 0.002

The good numerical agreement between the LLA + O(α_s) model and the data for all jet rates is remarkable.

5.5 SYSTEMATIC CHECKS

5.5.1 Different Jet Algorithms

These results have been checked using different jet-finding algorithms [133]. As an example, the jet rates are shown in Fig. 5.3 for an algorithm which finds jets by minimising particle transverse momenta with respect to a specified number of axes. As this algorithm contains no variable jet resolution parameter the following procedure was adopted: The number of axes was set to five, and when the five jets had been found all jet pairs were required to satisfy the JCLUST criterion $m_{ij}^2 \quad > \quad y_c E_{vis}^2$, otherwise the pair with the smallest invariant mass were combined by adding four-vectors, until all pairs were resolvable. The jet rates are thus shown in Fig. 5.3 as a function of y_c; for a given y_c they do not correspond exactly with those shown in Fig. 5.2, because the actual jet reconstruction criteria were different. It is clear that the model calculations show exactly the same trends as those seen in Fig. 5.2 and discussed in Section 5.4 for the JCLUST algorithm.

Thus, whilst the absolute jet rates differ between different algorithms, so that it is impossible to compare results numerically, it is found that the O(α_s^2) model is always

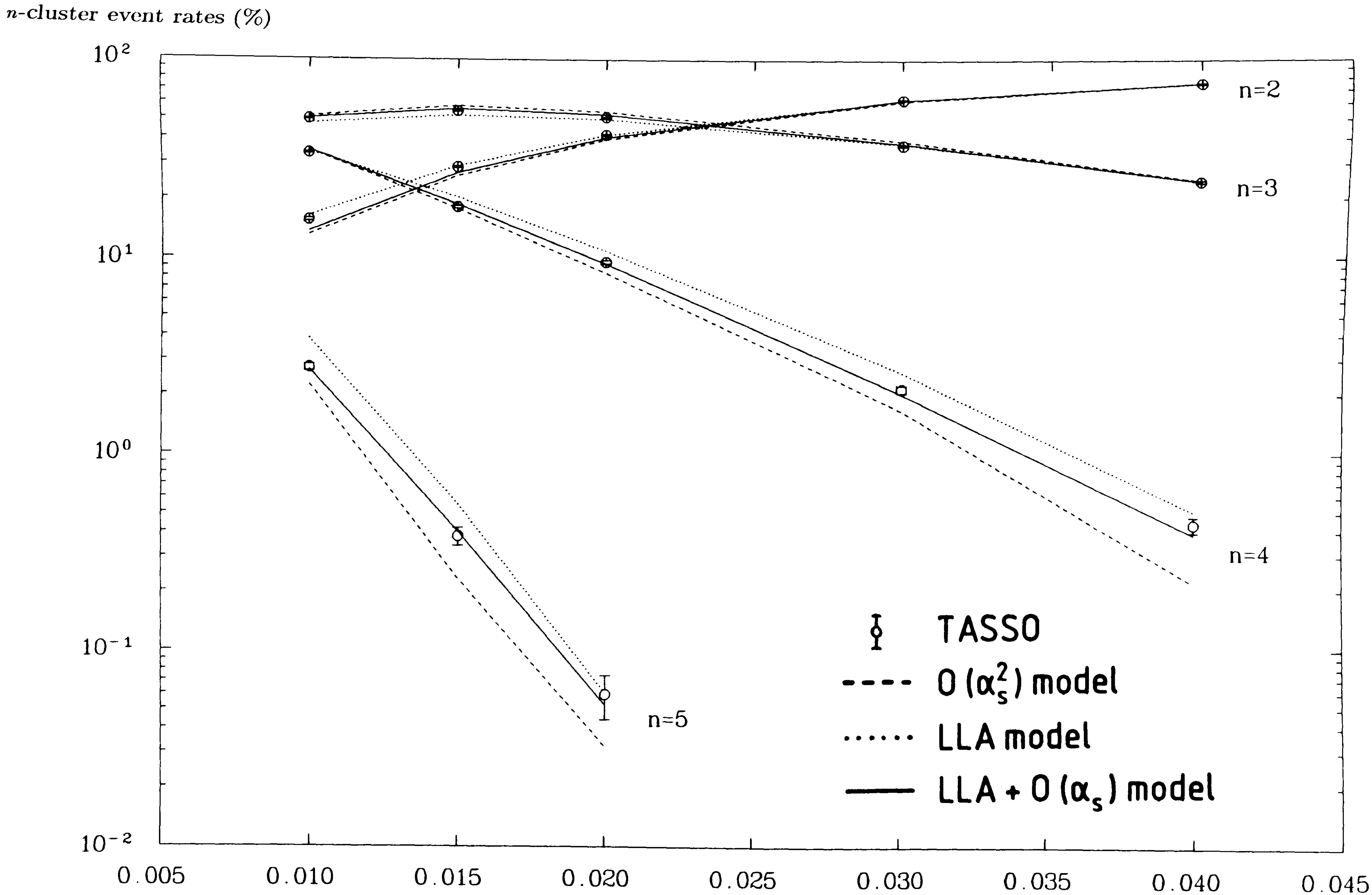

Figure 5.3: The n-jet event rates (%), defined using a transverse momentum algorithm and the JCLUST jet resolution criterion, as a function of the jet resolution parameter y_c.

seriously deficient in the rates of 4- and 5-jets, whilst the LLA and LLA + $O(\alpha_s)$ models are in good agreement with the data. Furthermore, the LLA + $O(\alpha_s)$ model gives comparable or better agreement with the 2- and 3-jet rates than does the $O(\alpha_s^2)$ model, which tends to underestimate and overestimate respectively these rates, whereas the LLA model overestimates and underestimates respectively.

5.5.2 Change of Model Parameters

The results were also found to be insensitive to reasonable changes of the model parameters from the values given in Section 3.6.3. The parameters were varied so as to preserve a reasonable overall description of the global features of the data: one parameter was fixed to a value different from the tuned one and a new fit was performed allowing the remaining parameters to vary as described in Section 3.6.2. In particular for the LLA model decreasing the QCD scale parameter Λ_{LL} gave lower rates of $\geq$4 clusters, in better agreement with the data, but also a reduced 3-jet rate falling even further beneath the data than previously. Similarly for the $O(\alpha_s^2)$ model increasing $\Lambda_{\overline{MS}}$ from 0.62 to 1.1 GeV, a change in α_s from 0.17 to 0.20, gave 4, $\geq$5-jet rates in much better agreement with the data, at the expense of a seriously underestimated 2-jet rate and overestimated 3-jet rate across the whole range of y_c. We note that the $O(\alpha_s^2)$ model employs the 2^{nd} order perturbative calculations of Gutbrod, Kramer and Schierholz [41], where certain 2^{nd} order correction terms are known to have been neglected [36,134]. It was found in [130] that the effect of including the more detailed 2^{nd} order matrix elements of Gottschalk and Shatz (see references in [130]) resulted in an even greater discrepancy in the 4-jet rate between the $O(\alpha_s^2)$ model and the data. This detail does not affect our conclusion and will not be considered further here.

5.6 RELATIONSHIP BETWEEN HADRON JETS AND PARTONS

By definition, the $O(\alpha_s^2)$ model can produce only 2, 3 or 4 partons, whereas around 6 partons are typically produced by the two cascade models, though as many as 10 is not uncommon. For the latter it is hence difficult to relate partons to the hadronic jets directly, and also to compare parton-level results with the $O(\alpha_s^2)$ model. Therefore, in order to check that the differences between the models shown in Figs. 5.2 and 5.3 arise from the different perturbative QCD treatments, and not from fragmentation effects, the cluster algorithm was applied directly to the partons before hadronization. The resulting 'parton-cluster' rates are shown as a function of y_c, for $W = 35$ GeV, in Figure 5.4. Note that the cluster-pair mass criterion used was

$$m_{ij}^2 \quad > \quad y_c E_{rad}^2$$

where E_{rad} is the hadronic c.m. energy after initial state photon radiation from the e^+ or e^-.

The differences between the models already exist at the parton level, though are considerably reduced by hadronisation, and we conclude that the observed hadronic cluster rates essentially reflect the underlying QCD processes.

5.7 ENERGY EVOLUTION OF THE JET RATES

We present the jet rates for data and models at c.m. energies in the PETRA range and also show the model predictions for W up to 200 GeV. The data were therefore corrected for acceptance, neutral particles, detector effects, initial state radiation and the cuts described in Section 5.3 using a LLA + $O(\alpha_s)$ model Monte Carlo simulation as described in Section 3.7. The model calculations are for both charged and neutral particles with no initial state radiation, cuts or detector simulation.

To make a comparison at different c.m. energies there are two possibilities: one can fix either m_{ij}^{cut} or y_c. For the latter case the jet resolution decreases as the c.m. energy increases, which is unphysical from an experimental point of view in that the ability to resolve jets is determined by the detector configuration and is more or less energy independent. The more physical choice is therefore to keep the mass-cutoff constant. m_{ij}^{cut} was fixed at 7 GeV/c^2, a reasonable value which corresponds to $y_c = 0.04$ at $E = W = 35$ GeV; the corresponding values of y_c at $E = 14$, 22 and 43.8 GeV are 0.25, 0.10 and 0.025 respectively. The energy dependence of the cluster rates is shown in Fig. 5.5 and Table 5.7. In the figure the lines join the model calculations at the same energies as the data.

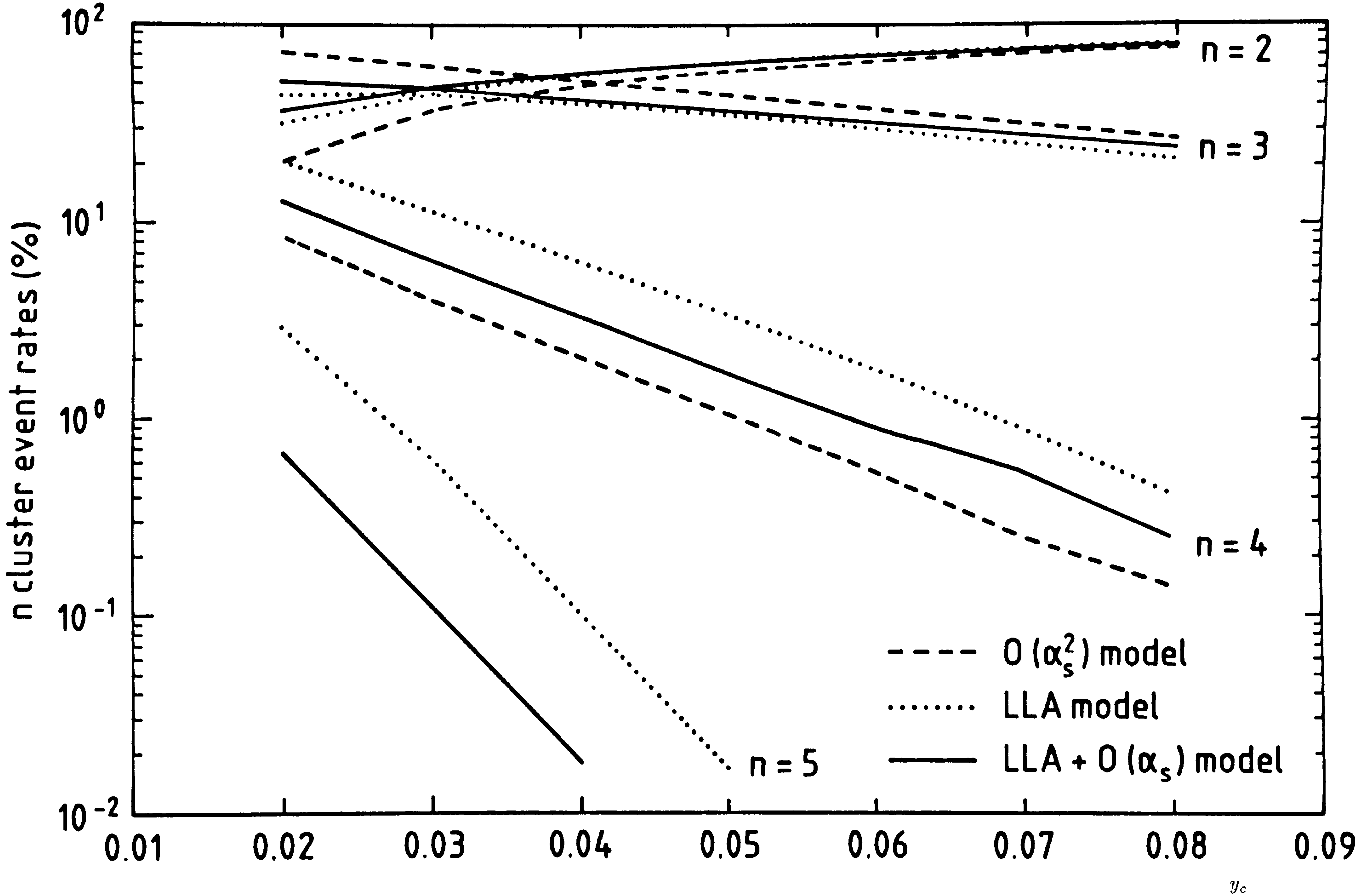

Figure 5.4: The parton-level n-jet event rates (%), defined using the JCLUST algorithm, as a function of the jet resolution parameter y_c.

Table 5.7: The cluster rates observed in the data, corrected for acceptance, neutral particles, detector and radiative effects, at the four mean c.m. energy values used in the study, for fixed cluster-pair-mass cutoff $m_{ij}^{cut} = 7$ GeV/c^2.

$< W >$ (GeV)	2-cluster	3-cluster	4-cluster	$\geq$5-cluster
14.0	97.1 ± 2.1	2.9 ± 0.5	-	-
22.0	80.3 ± 2.3	19.7 ± 1.2	-	-
35.0	55.2 ± 0.7	41.1 ± 0.6	3.60 ± 0.16	0.04 ± 0.02
43.8	41.0 ± 1.2	49.6 ± 1.1	8.7 ± 0.5	0.38 ± 0.11

It is notable that using parameters extracted from a fit to data at $W = 35$ GeV, where jet rates were not considered in the tuning, all models reproduce the trend of the jet rates data across the whole energy range spanned. The LLA + O(α_s) model is in good numerical agreement with the data for all jet rates, whilst the O(α_s^2) model shows a similar deficiency of $\geq$ 4 jets at 44 GeV as at 35 GeV and the LLA model underestimates the 3-jet rate at all energies.

In addition, the jet rates are shown in Fig. 5.6, where the model calculations are also shown at $W = 60$,93 and 200 GeV. For the O(${\alpha_s}^2$) model (Fig. 5.6a), above 60 GeV the 2,3-jet rates decrease only very slowly with energy, implying both that the parton jet structure is fully resolved after hadronisation and that hadronisation fluctuations do not give rise to many spurious jets. The 5-jet events in Fig. 5.6a must be due to such fluctuations and represent about 2% (5%) of all events at $W = 93$ (200) GeV. The two cascade model calculations should be taken more seriously at higher W (Fig. 5.6b), where an O(${\alpha_s}^2$) calculation of up to four-parton states is expected to be unrealistic; the difference between the Webber and Lund predictions provides an estimate of the theoretical uncertainty in the extrapolation. From Fig. 5.6b, the total jet cross section at $W = 200$ GeV is dominated by $\geq$ 4-jet final states, which will form a background to events containing heavy states which decay into hadron jets. In particular events of the type $e^+e^- \rightarrow W^+W^-$, where each W decays to two quarks, may be difficult to isolate as gluon bremsstrahlung from the quarks disrupts the simple four jet event topology. It is estimated [135] that 43% (40%) of W^+W^- events will give rise to 5 ($\geq$ 6) resolvable partons, and hence in principle up to 5 or 6 hadron jets.

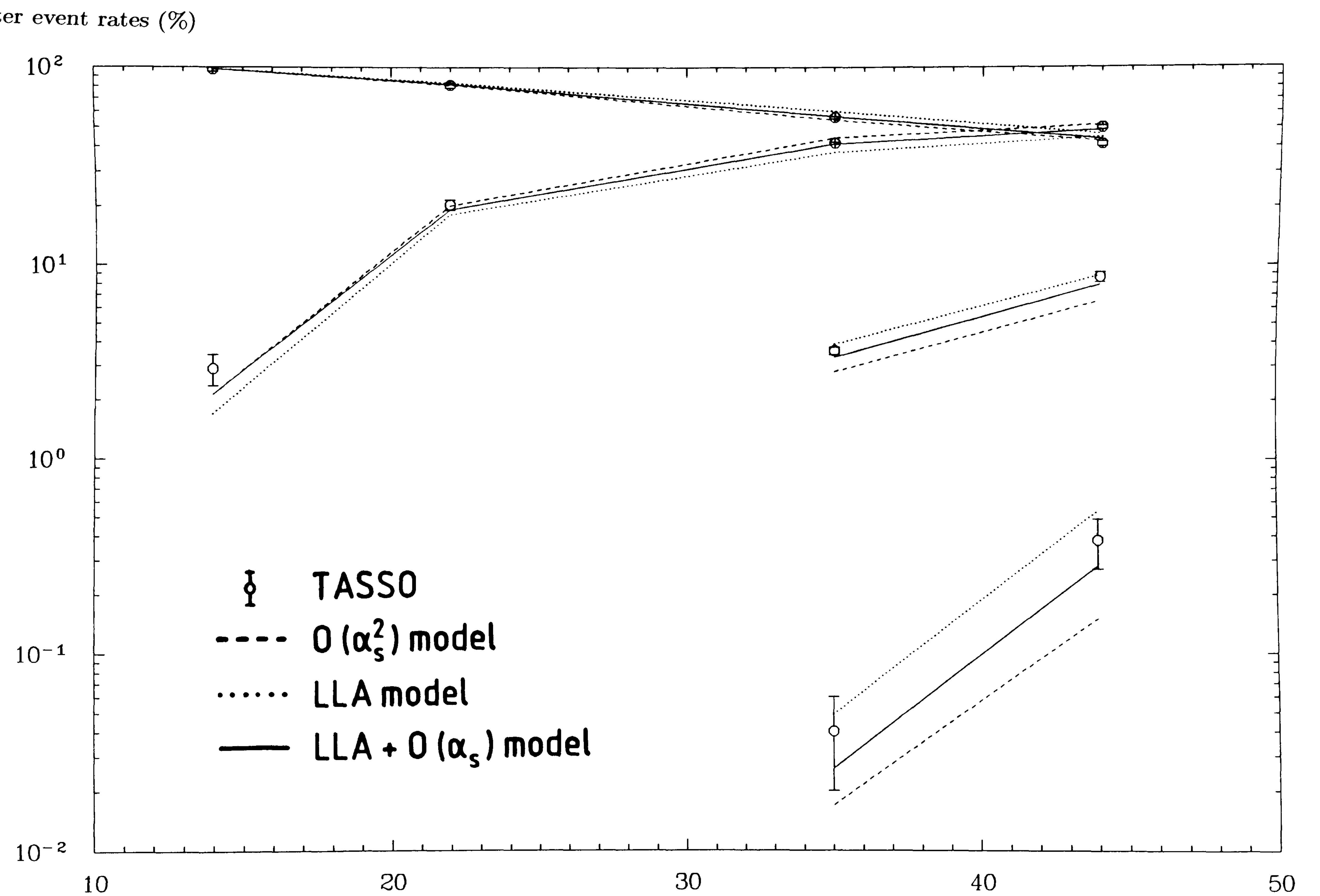

Figure 5.5: The n-jet event rates (%), defined using the JCLUST algorithm for fixed jet-jet mass resolution 7 GeV/c^2, as a function of W.

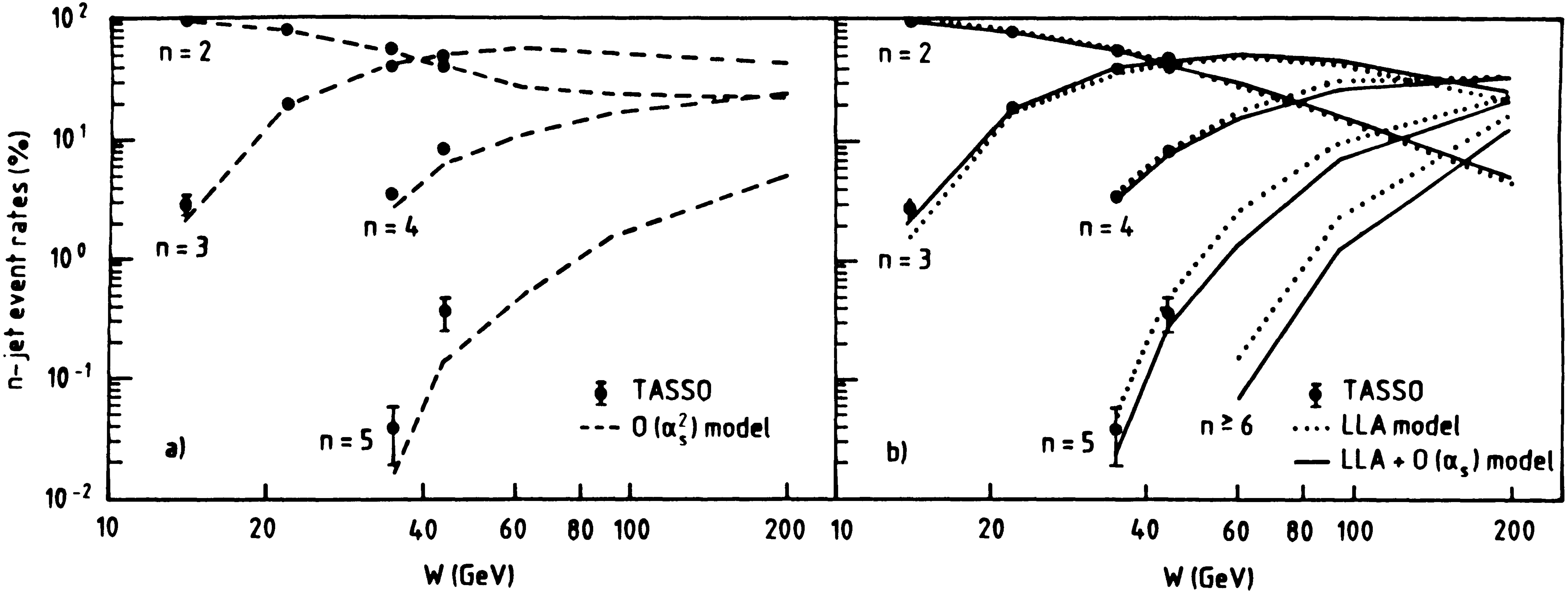

Figure 5.6: The n-jet event rates (%), defined using the JCLUST algorithm for fixed jet-jet mass resolution 7 GeV/c^2, as a function of W.

5.8 THE Q^2 DEPENDENCE OF α_s

In the language of exact matrix elements the 3-jet cross section in e^+e^- annihilation is proportional to α_s. One way to investigate the Q^2 dependence of α_s is hence to measure the 3-jet rate, R_3, as a function of Q^2. We have followed the procedure of [22] and used the JCLUST cluster algorithm to define the jet multiplicity in events. This is only meaningful provided the reconstructed jets reflect the underlying parton structure and are not strongly influenced by fluctuations due to hadronisation.

In general $R_3 = R_3(W, y_c)$. If the ratio $R_3(W_1, y_c)/R_3(W_2, y_c)$ is independent of y_c then hadronisation fluctuations are small at c.m. energies W_1, W_2. We show in Figure 5.7 the ratios $R_3(14)/R_3(35)$, $R_3(22)/R_3(35)$, $R_3(43.8)/R_3(35)$ as functions of y_c. At $W = 14$ GeV the ratio depends strongly on y_c, implying that the fluctuations are large. This is unfortunate, for it means that the 14 GeV data cannot be safely used for these purposes. At $W = 22$ GeV the ratio becomes independent of y_c above $y_c \sim 0.06$, whilst there is virtually no dependence at all on y_c at $W = 43.8$ GeV. Therefore, provided y_c is chosen sufficiently large R_3 is insensitive to hadronisation fluctuations for $W \geq 22$ GeV.

We show in Figure 5.8 and Table 5.8 R_3 for the data, corrected for acceptance, detector and radiative effects, for fixed $y_c = 0.08$. Also shown in the figure are curves for the LLA + $O(\alpha_s)$ model for the two cases: (i) running α_s with $\Lambda_{LL} = 0.26$ GeV, determined from the parameter optimisation at $W = 35$ GeV (Section 3.6.3); and (ii) fixed $\alpha_s = 0.265$; this value being chosen to be in good agreement with R_3 for the data at $W = 35$ GeV.

Table 5.8: The corrected rate of 3-jet events, defined with $y_c = 0.08$, for the data.

$< W >$ (GeV)	R_3 (%)
14.0	41.4 ± 1.7
22.0	26.5 ± 1.8
35.0	22.0 ± 0.5
43.8	19.5 ± 0.8

For the data R_3 clearly decreases as W increases: $R_3(22)/R_3(43.8) = 1.36 \pm 0.11$. Note

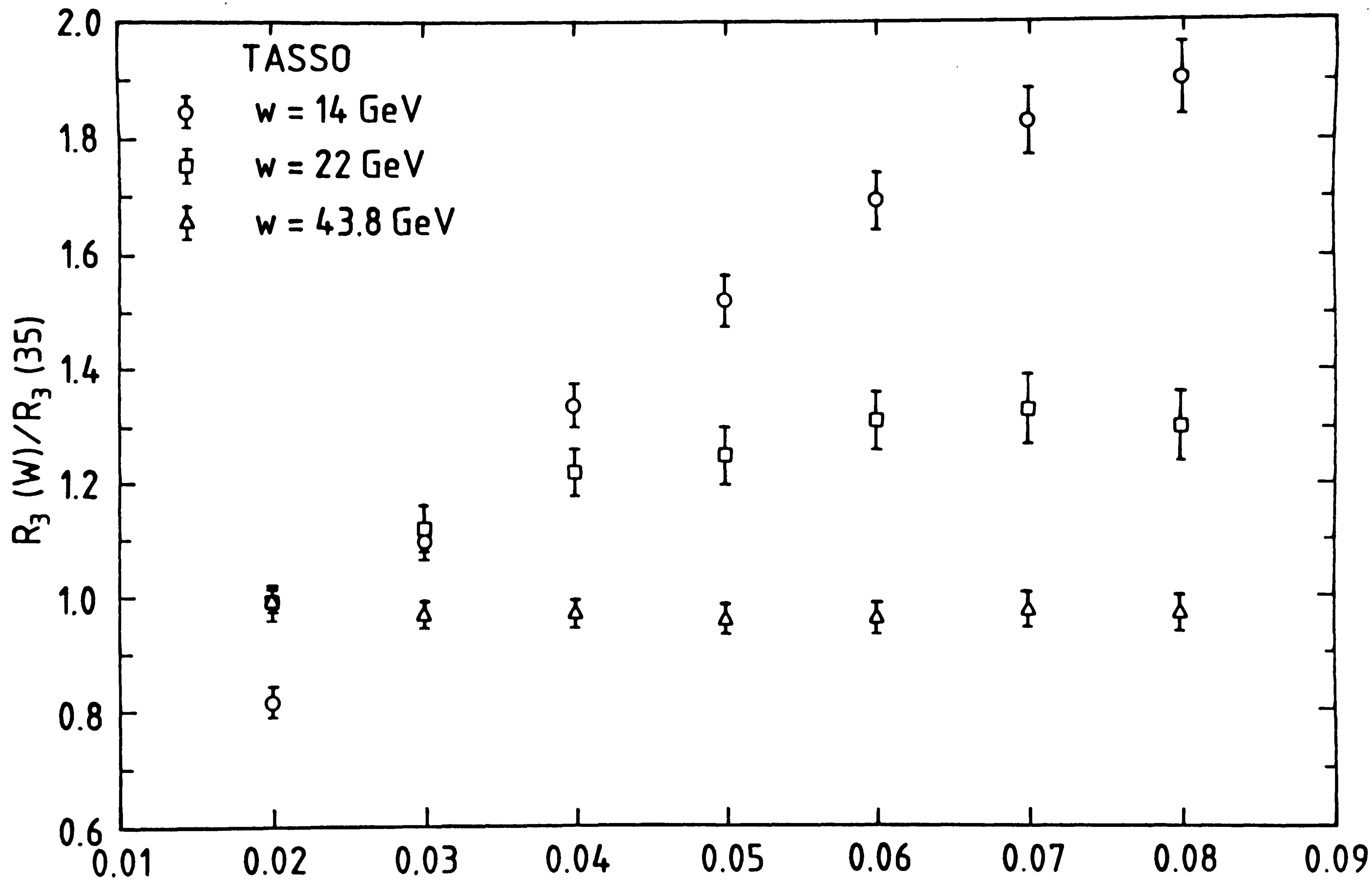

Figure 5.7: The ratios $R_3(14)/R_3(35)$, $R_3(22)/R_3(35)$, $R_3(44)/R_3(35)$ for the TASSO data, where the 3-jet rate R_3 was defined using the JCLUST algorithm, as a function of the jet resolution parameter y_c.

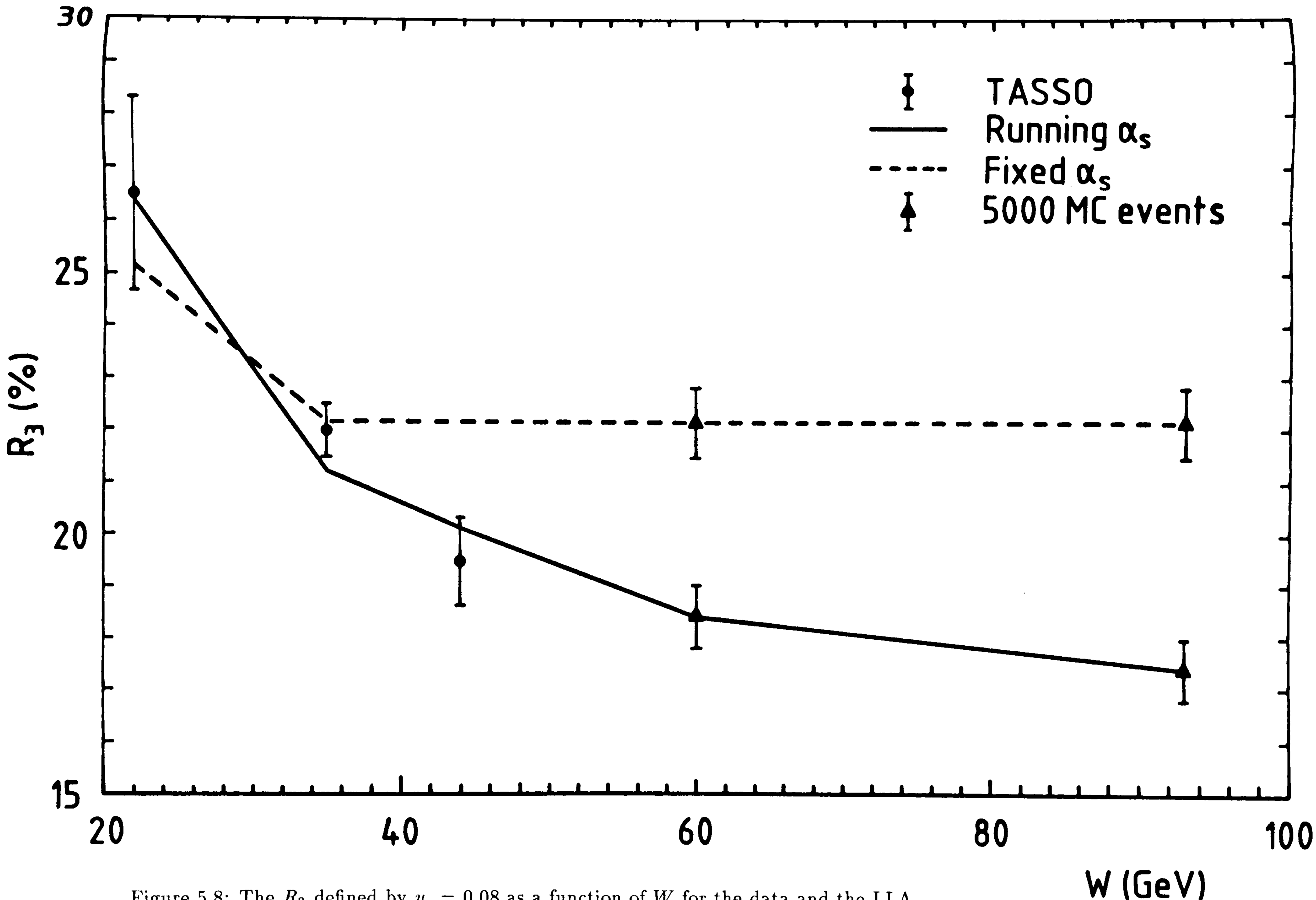

Figure 5.8: The R_3 defined by $y_c = 0.08$ as a function of W for the data and the LLA + $O(\alpha_s)$ model with both a running coupling constant and a fixed coupling constant. The error bars at $W = 60$, 93 GeV represent the statistical error if R_3 were determined from only 5000 events.

however that a slight decrease is also shown by the LLA + O(α_s) model with fixed α_s. though the data prefer the model with running α_s. The model results are also shown at W = 60 and 93 GeV. In addition, error bars are shown at these higher energies corresponding to the statistical errors on a measurement of R_3 using only 5000 events. Such measurements would demonstrate conclusively whether α_s runs with Q^2.

5.9 SUMMARY AND CONCLUSIONS

This analysis of multijet rates has shown that O(α_s^2) QCD cannot reproduce the rates of spherical and 4-jet like events observed in the data. A high value of $\Lambda_{\overline{MS}}$ is required to give sufficient rates of $\geq$ 4-jets, but such a value causes a severe underestimation of the 2-, and an overestimation of the 3-, jet rates. For a $\Lambda_{\overline{MS}}$ determined from a best fit to a few global properties of hadronic final states, which are dominated by 2- and 3- jet-like events, this QCD model shows a serious deficiency of $\geq$ 4-jets. Conversely LLA QCD gives a more satisfactory description of $\geq$4- jet rates at the expense of 2,3-jet rates which are overestimated and underestimated respectively. These results are in agreement with previous studies [22,130].

We find that the LLA + O(α_s) QCD model is in very good agreement with the data for *all* cluster rates and conclude the following:

(i) Contributions from higher order, eg O(α_s^3), QCD are observable at the highest e^+e^- c.m. energies analysed to date, and can be expected to be considerable at colliders operating in the 100 GeV range. QCD models accurate only to O(α_s^2) are already inadequate to describe multijet rates, and the discrepancy will increase as the amount of gluon bremsstrahlung increases with energy.

(ii) LLA QCD models incorporating many orders in perturbation theory are, because of the approximations used in the formalism, unable to account for *both* the 3- and $\geq$ 4-jet rates *simultaneously*. When the $\geq$ 4-jets are well-described there is a poor estimation of hard 3-jet events. Whilst both LLA and O(α_s^2) models may give comparable descriptions of many hadronic final state properties at PETRA energies, their predictions will diverge considerably as the c.m. energy rises [63,125].

(iii) The most satisfactory account of the observed jet rates at c.m. energies up to 44

GeV is provided by the LLA + O(α_s) model. In the absence of 3^{rd} (and higher order) matrix element calculations, this model provides a sensible basis for future theoretical developments and is a good tool for extrapolation to higher energy scales.

We have also found that the rate of 3-jet events in the data decreases with increasing c.m. energy, consistent with a running coupling strength α_s as predicted by QCD. The data are in agreement with a Q^2 dependence of the form $\alpha_s \sim 1/\ln\frac{Q^2}{\Lambda^2}$ though other possibilities, such as α_s fixed or decreasing linearly with W, cannot be ruled out by the limited statistics and relatively narrow energy range of the PETRA data. Measurements of R_3 at higher energies, in combination with the data presented here and elsewhere [22], should clarify these issues.

CHAPTER 6

SUMMARY, CONCLUSIONS AND OUTLOOK

The three most successful perturbative QCD + fragmentation models were compared with the high statistics data sample collected by TASSO at 35 GeV. Having optimised the important parameters of each model by comparison with the data for a few relevant observables, it was found that all the models gave a reasonable overall description of the global features of hadronic events at this energy, though the quality of description of different observables varied for each model.

The differences between the model results were interpreted in terms of the underlying QCD calculations and fragmentation schemes used. The Lund $O(\alpha_s^2)$ model described properties in the event plane, mainly determined by hard gluon bremsstrahlung, very well, but was deficient in the properties transverse to this plane, which are more sensitive to soft gluon and hadronisation effects. The Webber LLA model gave a good description of the transverse observables, but overestimated those quantities in the plane. The Lund LLA + $O(\alpha_s)$ model provided a good representation of the transverse properties but underestimated some quantities in the plane, though here the discrepancy between MC and data was much smaller than for the LLA model. This suggests that the amount of hard gluon radiation is somewhat underestimated, despite matching the $O(\alpha_s)$ matrix element onto the cascade to try and get this feature correct. It is tempting to suggest that the slight lack of gluon emission in the event plane could be made up by $O(\alpha_s^2)$ corrections to the $O(\alpha_s)$ matrix element, though this cannot of course be proved, and hadronisation effects are probably just as large as such corrections.

The best overall description of the data was given by the Lund LLA + $O(\alpha_s)$ model, and it was concluded that this model was successful in reproducing accurately most features of the data because it includes QCD calculations of both hard and multiple soft gluon emission processes.

The models were then compared with most of the available data collected across a wide range of energies explored at PETRA and PEP: $12.0 \leq < W > \leq 41.5$ GeV, keeping the parameters fixed at the values optimised for 35 GeV. The evolution of the mean values of the observables as a function of c.m. energy within this range was generally well described, and though there was relatively little to choose between them, the Lund LLA + O(α_s) model was again the most successful.

The energy domain around 60 GeV is presently being explored by the TRISTAN collider, whilst SLC and LEP will soon have e^+e^-collisions at $\sim$ 93 GeV, and LEP-2 could be operating at 200 GeV by the mid-1990's. Within the next decade there should hence be abundant data spanning a 200 GeV energy range, providing an opportunity to test rigorously the perturbative QCD calculations and fragmentation models which this analysis has shown to be very successful. With this in mind, the model predictions were extended up to W = 200 GeV in terms of both mean values and differential distributions of the observables. These calculations provide both an estimate of the properties of hadronic events at higher energies and an illustration of the differences between the model predictions. Interestingly the two parton cascade models gave similar predictions of the event properties around W = 200 GeV, which differed significantly from the O($\alpha_s{}^2$) model predictions. One important factor to bear in mind is that the influence of the hadronisation process, which sets in around $Q^2 \sim 1$ GeV^2, upon the final state should decrease as W increases. In other words, the properties of the final state should be predominantly determined by the parton-level processes which are in principle calculable by QCD. The convergence of the two LLA cascade models at high energies may be a reflection of this.

Top quark production was simulated at W = 200 GeV for a top mass of 60 GeV/c^2 and the distributions of thrust, aplanarity, $p_{T_{in}}$, $p_{T_{out}}$ and rapidity were found to be most sensitive to its presence.

The data at 35 GeV were also analysed in terms of explicit multijet final states, using a cluster algorithm for jet definition, and compared with the QCD model calculations. The results were checked with different jet-finding algorithms and were also found to be stable with respect to reasonable changes of the model parameter values. The differences between the model results were found to derive from the perturbative QCD parton-level calculations: The deficiency of $\geq$ 4-jet events given by the Lund $O(\alpha_s{}^2)$ model was interpreted as evidence for the need for higher order contributions from QCD perturbation theory. Similarly the poor description of the 3-jet rate by the Webber LLA model, even though $\geq$ 4-jets were well described, was taken to result from the inherent approximations in the LLA formalism, which are most serious for hard gluon emission. Only the Lund LLA + $O(\alpha_s)$ model was able to reproduce all the jet rates accurately, a remarkable achievement given that there was no tuning to these rates.

Fixing the jet-jet resolution scale at a sensible value in the cluster algorithm, the jet rates were then studied as a function of c.m. energy in the range $14.0 \leq < W > \leq 43.8$ GeV. All the models, with the parameters optimised for 35 GeV, reproduced the trend of the data, the Lund LLA + $O(\alpha_s)$ model being in addition in excellent numerical agreement for all jet rates. Jet rates were also calculated for the models up to $W = 200$ GeV, where it was found that for the two parton cascades over half of all events contain $\geq$4 jets. Such 'normal' hadronic events will hence form a background to multijet final states arising from the decay of new heavy particles, *eg.* $e^+e^- \rightarrow W^+W^-$ events where each W decays to two quarks.

The results on multijet final states reinforce the conclusions from the study of the global event characteristics: in the absence of exact perturbative QCD calculations to many orders in α_s, the best description of the data is provided by a QCD matrix element calculation of low multiplicity hard parton states combined with an approximate many order calculation using the LLA to represent multiple soft gluon emission. If such an approach is to be anything more fundamental than a complicated parametrisation of the data, the blending of the matrix element with the parton cascade must naturally be done in a theoretically respectable fashion, as has been achieved by the Lund group. Such ideas mark the way ahead for perturbative QCD + fragmentation models*, for

* There have already been exciting developments since this analysis was completed. A new parton shower model including the full next-to-leading order logarithmic contributions, in addition to the leading ones, and the $O(\alpha_s)$ matrix element, has recently been announced [136] and appears to be very successful compared with present data [137]. Such developments are very timely and welcome at the beginning of the 100 GeV collider era.

one expects the agreement of the $O(\alpha_s{}^2)$ calculations with the data to become poorer at higher energies where there is generally more resolvable gluon bremsstrahlung and the neglected higher orders in α_s become more noticeable in the hadronic final state. It remains to be seen whether the LLA-only calculations will survive the test of SLC and LEP data.

The dependence of the strong coupling constant α_s on Q^2 was investigated by studying the energy dependence of the 3-jet rate R_3, which is roughly proportional to α_s. By comparing the data with the Lund LLA + $O(\alpha_s)$ model calculations with and without a running α_s, R_3 was found to decrease in a manner consistent with a dependence of the form $\alpha_s \sim 1/\ln(\frac{Q^2}{\Lambda^2})$ as predicted by QCD, though the case $\alpha_s \sim$ constant could not be ruled out with the limited statistics and energy span of the present data. This conclusion is in agreement with other studies by the Mark II and JADE collaborations [138,139] and with a very recent analysis by the AMY collaboration using their data in the range $50 \leq W \leq 56$ GeV [140]. It was also shown from Monte Carlo studies that a measurement of R_3 using a sample of only a few thousand hadronic events at $W \sim 60$ or 93 GeV would have sufficient statistical precision to confirm (or otherwise) that $\alpha_s \sim 1/\ln(\frac{Q^2}{\Lambda^2})$ with a significance of many standard deviations. More data are hence eagerly awaited from the TRISTAN experiments as are the first data from the SLC and LEP colliders in the next few years.

In summary, we have a very thorough understanding of jet fragmentation in terms of models which combine perturbative QCD calculations with phenomenological hadronisation schemes. Ideally one would wish to have respectable theoretical calculations of hadronisation rather than phenomenological schemes. However, in the absence of such calculations, this study has shown that it is possible to gain great insight into the underlying QCD processes by careful comparison of the models with the data and interpretation of the results within the context of the models.

Appendix A

Members of the TASSO Collaboration, 1978-1988

I. Physikalisches Institut der RWTH Aachen, 5100 Aachen, FRG[1]

M. Althoff, R. Brandelik, W. Braunschweig, R. Gerhards, B. Jaax, V. Kadansky, F.-J. Kirschfink, K. Lübelsmeyer, H.-U. Martyn, G. Peise, J. Rimkus, P. Rosskamp, H.G. Sander, D. Schmitz, A. Schultz von Dratzig, H. Siebke, W. Wallraff

Physikalisches Institut der Universität Bonn, 5300 Bonn, FRG[1]

B. Bock, H. Boerner, S. Cooper, H.M. Fischer, H. Hartmann, J. Hartmann, E. Hilger, W. Hillen, A. Jocksch, G. Knop, L. Köpke, H. Kolanoski, W. Korbach, H. Kück, V. Mertens, F. Roth, W. Rühmer, R. Wedemeyer, N. Wermes, M. Wollstadt

H.H. Wills Physics Laboratory, University of Bristol, Bristol, BS8 1TL, UK[2]

B. Foster, A.J. Martin, A.J. Sephton, A. Wood

Deutsches Elektronen-Synchrotron, DESY, 2000 Hamburg 52, FRG[1]

E. Bernardi, R. Bühring, H. Burkhardt, D.G. Cassel, J. Chwastowski, A. Eskreys, R. Fohrmann, J. Franzke, K. Gather, K. Genser, H. Hultschig, P. Joos, B. Klima, W. Koch, P. Koehler, U. Kötz, H. Kowalski, A. Ladage, B. Löhr, D. Lüke, H.L. Lynch, P. Mättig, K.H. Mess, D. Notz, R.J. Nowak, J.M. Pawlak, K.-U. Pösnecker, J. Pyrlik, D.R. Quarrie, R. Riethmüller, E. Ros M. Rushton, M. Schliwa, W. Schütte, P. Söding, D. Trines, T. Tymieniecka, R. Walczak, G. Wolf, Ch. Xiao

Institut für Physik, Universität Dortmund, FRG[1]

H. Kolanoski

II. Institut für Experimentalphysik der Universität Hamburg, 2000 Hamburg, FRG[1]

E. Hilger, T. Kracht, H.L. Krasemann, J. Krüger, P. Leu, E. Lohrmann, D. Pandoulas, G. Poelz, J. Ringel, O. Römer, R. Rüsch, P. Schmüser, B.H. Wiik, W. Zeuner

Department of Physics, Imperial College, London, SW7 2AZ, UK[2]

I. Al-Agil, R. Beuselinck, D.M. Binnie, A.J. Campbell, P.J. Dornan, N.A. Downie, D.A. Garbutt, J. Hassard, C. Jenkins, T.D. Jones, W.G. Jones, J. McCardle, A. Pevsner, J.K. Sedgbeer, J. Shulman, R.A. Stern, D. Su, J.A. Thomas, W.A.T. Wan Abdullah, S.F. Yarker

Universidad Autonoma de Madrid, Madrid, Spain[3]

F. Barreiro, A. Leites, J. del Peso

Department of Nuclear Physics, Oxford University, Oxford, OX1 3RH, UK[2]

C. Balkwill, R.J.Barlow, M.G.Bowler, I.C.Brock, P.S.Bull, P.N. Burrows, R.K.Carnegie, R.J. Cashmore, P. Clarke, P.D. Dauncey, R.C.E. Devenish, P. Grossmann, C.M. Hawkes, G.P. Heath, J. Illingworth, D.J. Mellor, M. Ogg, P.N. Ratoff, B.P. Roe, G.L. Salmon, I.M. Silvester, I.R. Tomalin, M.E. Veitch, T.R. Wyatt, C. Youngman

Department of Physics, Queen Mary College, London, E1 4NS, UK[2]

S.L. Lloyd

Rutherford Appleton Laboratory, Chilton, Didcot, Oxon, OX11 0QX, UK[2]

K.W. Bell, W. Chinowsky, G.E. Forden, J.C. Hart, J. Harvey, D.K. Hasell, J. Proudfoot, D.H. Saxon, P.L. Woodworth

Fachbereich Physik der Universität-Gesamthochschule Siegen, 5900 Siegen, FRG[1]

S. Brandt, M. Dittmar, D. Heyland, M. Holder, G. Kreutz, L. Labarga, B. Neumann

Weizmann Institute, Rehovot 76100, Israel[4]

E. Duchovni, Y. Eisenberg, D. Hochman, U. Karshon, E. Kogan, G. Mikenberg, R. Mir, A. Montag, D. Revel, E. Ronat, A. Shapira, N. Wainer, G. Yekutieli

Department of Physics, University of Wisconsin, Madison, WI 53706, USA[5]

G. Baranko, T. Barklow, A. Caldwell, M. Cherney, J.E. Freeman, M. Hildebrandt, J.M. Izen, P. Lecomte, M. Mermikides, T. Meyer, D Muller, S. Ritz, G. Rudolph, D. Strom, M. Takashima, H. Venkataramania, E. Wicklund, Sau Lan Wu, G. Zobernig

1 Supported by the Bundesministerium für Forschung und Technologie
2 Supported by the UK Science and Engineering Research Council
3 Supported by CAICYT
4 Supported by the Minerva Gesellschaft für Forschung mbH
5 Supported by the US Department of Energy, contract DE-AC02-76ER00881

Appendix B

The TASSO Coordinate System

TASSO uses a right-handed cartesian coordinate system which defines the z axis to be along the positron beam direction, the y axis to be vertically upwards and the x axis to point horizontally towards the centre of the PETRA ring (Fig. B1). The $r-\phi$ plane is perpendicular to the z axis. The following symbols and parameters are used to describe a track [73] (Fig. B2):

Q is the charge of the track

R is the radius of curvature of the track in the $r-\phi$ projection

d_0 is the distance of the track from the origin in the $r-\phi$ projection at its point of closest approach, defined to be positive or negative according to whether the origin is inside or outside the circle of the track.

z_0 is the value of z at the point on the track from which d_0 is measured.

p is the momentum of the track at the point on the track from which d_0 is measured

p_t or p_{xy} is the component of p perpendicular to the z axis

θ $(0^0 \leq \theta \leq 180^0)$ is the polar angle between the track and the z axis

ϕ is the angle in the $r-\phi$ projection between the track and the x axis at the point on the track from which d_0 is measured, defined such that the $+y$ axis is at $\phi = 90^0$ and the $-y$ axis is at $\phi = 270^0$.

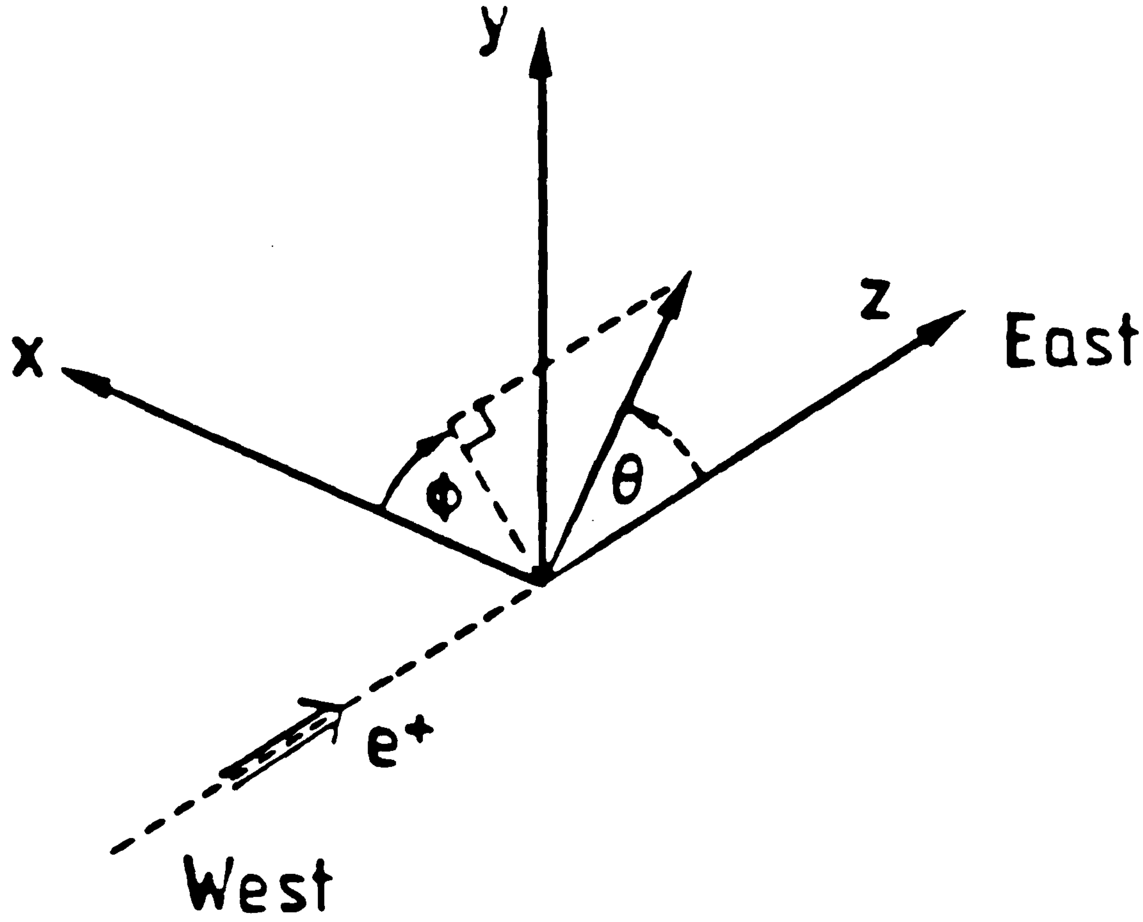

Fig. B.1 The TASSO coordinate system

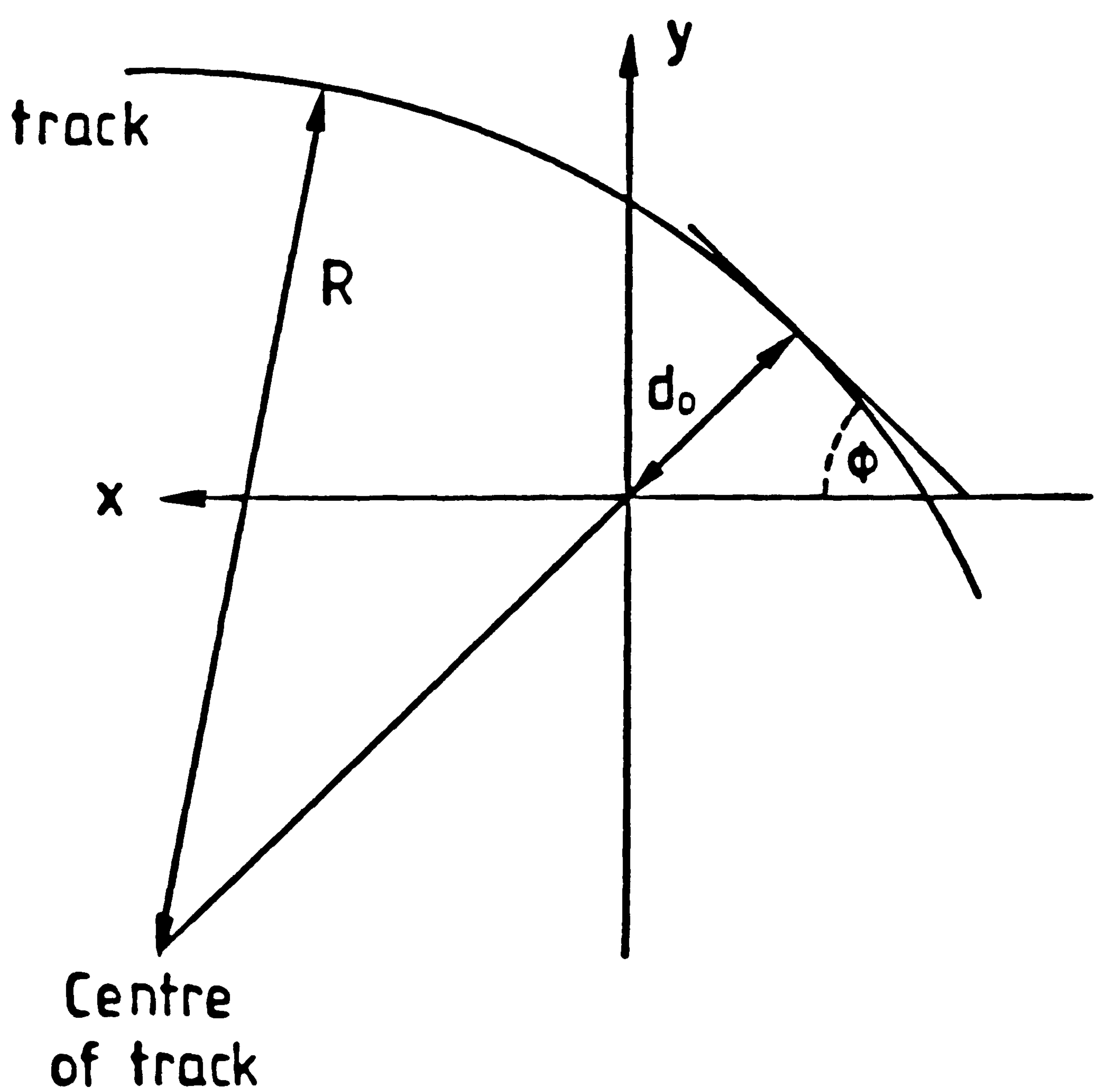

Fig. B.2 A track in the r-ϕ projection. The value of d_0 is positive for this track.

References

[1] H. Fritzsch, M. Gell-Mann, H. Leutwyler, Phys. Lett. **47B** (1973) 365.

[2] G. Kramer, Theory of Jets in Electron Positron Annihilation, Springer Tracts of Modern Physics, Vol **102**, Springer (1984).

[3] C.N. Yang, R.L. Mills, Phys. Rev. **96** (1954) 191.

[4] M. Gell-Mann, Phys. Rev. **125** (1962) 1067.

[5] See *eg.* R.P. Feynman, Photon-Hadron Interactions, Benjamin, Reading (1972).

[6] For an introduction to this topic see *eg.* M. Creutz, Quarks, Gluons and Lattices, Cambridge U.P. (1983).

[7] See *eg.* M. Gell-Mann, Y. Ne'eman, The Eightfold Way, Benjamin, New York (1972).

[8] M.Y. Han, Y. Nambu, Phys. Rev. **139B** (1965) 1006.

[9] E. Reya, Phys. Rep. **69** (1981) 195.

[10] CELLO Collab., H-J. Behrend *et al*, Phys. Lett. **B183** (1987) 400.

[11] R. Marshall, RAL 88-049 (1988).

[12] VENUS Collab., H. Yoshida *et al*, Phys. Lett. **198B** (1987) 570.
AMY Collab., H. Sagawa *et al*, Phys. Rev. Lett. **60** (1988) 93.
TOPAZ Collab., I. Adachi *et al*, Phys. Rev. Lett. **60** (1988) 97.

[13] T. Kamae, Talk at the XXIV International Conference on High Energy Physics, Munich 4-10 August 1988; to appear in the proceedings.

[14] See *eg.* R. Gatto, Proceedings of the International Symposium on Electron and Photon Interactions at High Energies, Hamburg 1965, 106.

[15] G. Hanson *et al*, Phys. Rev. Lett. **35** (1975) 1609.

[16] TASSO Collab., M. Althoff *et al*, Z. Phys. **C22** (1984) 307.

[17] See *eg.* R.J. Cashmore, Sci. Prog., Oxf. **71** (1987) 305.

[18] UA1 Collab., G. Arnison *et al*, Phys. Lett. **132B** (1983) 214.
UA2 Collab., P. Bagnaia *et al*, Z. Phys. **C20** (1983) 117.
UA1 Collab., G. Arnison *et al*, Phys. Lett. **158B** (1985) 494.
UA2 Collab., J. Appel *et al*, Z. Phys. **C30** (1986) 341.
AFS Collab., T. Åkesson *et al*, Z. Phys. **C32** (1986) 317.

[19] TASSO Collab., R. Brandelik *et al*, Phys. Lett. **97B** (1980) 453.

[20] J.G. Körner, G. Schierholz, J. Willrodt, Nucl. Phys. **B185** (1981) 365.

[21] CELLO Collab., Contributed paper to the XXIV International Conference on High Energy Physics, Munich 4-10 August 1988.

[22] S. Bethke, Heidelberg Habilitation Thesis, LBL 50-208 (1987).

[23] S.L. Wu, Phys. Rep. **107** (1984) 59.

[24] M. Dine, J. Sapirstein, Phys. Rev. Lett. **43** (1979) 668 and references therein.

[25] K.G. Chetyrkin, A.L. Kataev, F.V. Tkachov, Phys. Lett. **85B** (1979) 277.

[26] S.G. Gorishny *et al*, Proc. Conf. on Hadron Structure, Smolenice, Czechoslovakia, November 1987, ed. D. Krupa, Vol. **14** Physics and Applications, Inst. of Phys. EPRC. Slovak Academy of Sciences, Bratislava, 1988, and Dubna preprint JINR E2-88-254.

[27] W.J. Marciano, Phys. Rev. **D12** (1975) 3861.
G.A. Leibbrandt, Rev. Mod. Phys. **47** (1975) 849.

[28] J. Ellis *et al*, Nucl. Phys. **B111** (1976) 253; erratum **B130** (1977) 516.

[29] G. Kramer, G. Schierholz, J. Willrodt, Z. Phys. **C4** (1980) 149.
E. Laermann, P.M. Zerwas, Phys. Lett. **89B** (1980) 225.

[30] A.C. Hirshfeld, G. Kramer, D.H. Schiller, DESY 74-33 (1974) 253.

[31] S. Brandt *et al*, Phys. Lett. **12** (1964) 57.
E. Farhi, Phys. Rev. Lett. **39** (1977) 1587.

[32] C.L. Basham *et al*, Phys. Rev. **D17** (1978) 2298; Phys. Rev. Lett. **41** (1978) 1585.

[33] A. De Rujula *et al*, Nucl. Phys. **B138** (1978) 387.

[34] L.S. Brown, S.D. Ellis, Phys. Rev. **D24** (1981) 2383.

[35] G. Sterman, S. Weinberg, Phys. Rev. Lett. **39** (1977) 1436.

[36] G. Kramer, B. Lampe, DESY 86-119 (1986).

[37] T. Appelquist, H. Georgi, Phys. Rev. **D8** (1973) 4000.
A. Zee, Phys. Rev. **D8** (1973) 4038.

[38] D.W. Duke, R.G. Roberts, Phys. Rep. **120** (1985) 275.

[39] K. Fabricius *et al*, Phys. Lett. **97B** (1980) 431; Z. Phys. **C11** (1982) 315.

[40] R.K. Ellis *et al*, Nucl. Phys. **B178** (1981) 421.

[41] F. Gutbrod *et al*, Z. Phys. **C21** (1984) 235.

[42] T.D. Gottschalk, M.P. Schatz, Phys. Lett. **150B** (1985) 451.

[43] TASSO Collab., M. Althoff *et al*, Z. Phys. **C26** (1984) 157.

[44] G. Altarelli, G. Parisi, Nucl. Phys. **B126** (1977) 298.

[45] K. Konishi, A. Ukawa, G. Veneziano, Nucl. Phys. **B157** (1979) 45.
G.C. Fox, S. Wolfram, Nucl. Phys. **B168** (1980) 285.
K. Kajantie, E. Pietarinen, Phys. Lett. **93B** (1980) 269.
R.D. Field, S. Wolfram, Nucl. Phys. **B213** (1983) 65.
R. Odorico, Nucl. Phys. **B228** (1983) 381.

[46] G.S. LaRue *et al*, Phys. Rev. Lett. **38** (1977) 1011.

[47] T. Sjöstrand, Int. J. Mod. Phys. **A3** (1988) 751.

[48] B. Andersson, Lund preprint LU TP 88-2 (1988).

[49] T. Sjöstrand, M. Bengtsson, Comput. Phys. Commun. **43** (1987) 367.

[50] B. Andersson, G. Gustafson, G. Ingelman, T. Sjöstrand, Phys. Rep **97** (1983) 33.

[51] R. Sommer, Nucl. Phys. **B291** (1987) 673.
J. Ambjørn *et al*, Phys. Lett. **159B** (1985) 335.
E. Laermann *et al*, Phys. Lett. **173B** (1986) 437.
H. Joos, I. Montvay, Nucl. Phys. **B225** (1983) 565.
M. Campostrini *et al*, Phys. Lett. **193B** (1987) 78.

[52] B. Andersson, G. Gustafson, B. Söderberg, Z. Phys. **C20** (1983) 317.

[53] T. Sjöstrand, Lund preprint LU TP 85-10 (1985).

[54] G. Marchesini, B.R. Webber, Nucl. Phys. **B238** (1984) 1.
B.R. Webber, Nucl. Phys. **B238** (1984) 492.

[55] P. Dauncey, D. Phil. Thesis, University of Oxford, RAL T 034 (1986).

[56] A.H. Mueller, Phys. Lett. **104B** (1981) 161; Nucl. Phys. **B213** (1983) 85.
B.I. Ermalaev, V.S. Fadin, JETP Lett. **33** (1981) 269.
L.V. Gribov, E.M. Levin, M.G. Ryskin, Phys. Rep. **100** (1983) 1.
A. Bassetto, M. Ciafaloni, G. Marchesini, Phys. Rep. **100** (1983) 201.
Ya.I. Azimov *et al*, Phys. Lett. **165B** (1985) 147.

[57] JADE Collab., W. Bartel *et al*, Phys. Lett. **157B** (1985) 340.

[58] B. Andersson, G. Gustafson, T. Sjöstrand, Phys. Lett. **94B** (1980) 211.

JADE Collab., W. Bartel *et al*, Phys. Lett. **101B** (1981) 129.

[59] T.D. Gottschalk, Nucl. Phys. **B214** (1983) 201.

[60] R. Odorico, Z. Phys. **C30** (1986) 257.

[61] M. Bengtsson, T. Sjöstrand, Nucl. Phys. **B289** (1987) 810.

[62] G. Ingelman, Physica Scripta **33** (1986) 39.

[63] P.N. Burrows, G. Ingelman, Z. Phys. **C34** (1987) 91.
P.N. Burrows, G. Ingelman, Proceedings of the Workshop on Physics at Future Accelerators, CERN 87-07 (1987) Vol. II 369.

[64] D. Amati *et al*, Nucl. Phys. **B173** (1980) 429.
G. Curci, W. Furmanski, R. Petronzio, Nucl. Phys. **B175** (1980) 27.

[65] B. Klima, DESY 86-070 (1986).

[66] G. Marchesini, B.R. Webber, Cavendish-HEP-87/9 (1987).

[67] G. Marchesini, B.R. Webber, Cavendish-HEP-87/8, UPRF-87-212 (1987).

[68] B.R. Webber, Phys. Lett. **193B** (1987) 91.

[69] M. Bengtsson, T. Sjöstrand, Phys. Lett. **185B** (1987) 435.

[70] P.N. Burrows, TASSO Note N^0 375 (1987).

[71] T.D. Gottschalk, D.A. Morris, Nucl. Phys. **B288** (1987) 729.

[72] Mark II Collab., A. Petersen *et al*, Phys. Rev. **D37** (1988) 1.

[73] C.M. Hawkes, D. Phil. Thesis, University of Oxford, RAL T 011 (1985).

[74] D.J. Mellor, D. Phil. Thesis, University of Oxford, RAL T 036 (1986).

[75] TASSO Collab., W. Braunschweig *et al*, Z. Phys. **C37** (1988) 171.

[76] D. Notz, O. Hell, TASSO Note N^0 367 (1986).

[77] TASSO Collab., R. Brandelik *et al*, Phys. Lett. **83B** (1979) 261.

[78] D.M. Binnie *et al*, Nucl. Instr. Meth. **228** (1985) 267.

[79] C. Youngman, Ph.D. Thesis, University of London, RL-HEP/T/82 (1982).

[80] H. Boerner *et al*, Nucl. Instr. Meth. **176** (1980) 151.

[81] H.-U. Martyn, TASSO Note N^0 201 (1982).
H. Siebke, TASSO Note N^0 302 (1984).

[82] TASSO Collab., R. Brandelik *et al*, Phys. Lett. **113B** (1982) 98.

[83] TASSO Collab., M. Althoff *et al*, Phys. Lett. **139B** (1984) 126.
H. Siebke, W. Braunschweig, TASSO Note N^0 277 (1983).

[84] H. Burkhardt *et al*, Nucl. Instr. Meth. **184** (1981) 319.

[85] K.W. Bell *et al*, Nucl. Instr. Meth. **179** (1981) 27.

[86] T.R. Wyatt, D. Phil. Thesis, University of Oxford, RL-HEP/T/110 (1983).

[87] M. Ogg, D. Phil. Thesis, University of Oxford, RL-HEP/T/89 (1981).

[88] TASSO Collab., R. Brandelik *et al*, Phys. Lett. **108B** (1982) 71.

[89] V. Kadansky *et al*, Physica Scripta **23** (1981) 680.

F.-J. Kirschfink, Ph.D. Thesis, RWTH Aachen, PITHA 84/80 (1984).

[90] TASSO Collab., M. Althoff *et al*, Phys. Lett. **138B** (1984) 441.

A. Jocksch, H. Kolanoski, H. Kück, TASSO Note N^0 298 (1984).

A. Jocksch, T. Kracht, TASSO Note N^0 306 (1984).

[91] I. Brock, D. Phil. Thesis, University of Oxford, RL-HEP/T/106 (1983).

E. Hilger *et al*, TASSO Note N^0 118 (1980).

[92] A.J. Martin, private communications.

[93] D.G. Cassel, H. Kowalski, Nucl. Instr. Meth. **185** (1981) 235.

[94] D. Notz, Nucl. Instr. Meth. **A235** (1985) 380.

[95] B. Foster, S. Lloyd, SIMPLE manual, private communication.

[96] F.A. Berends, R. Kleiss, Nucl. Phys. **B177** (1981) 237.

F.A. Berends, R. Kleiss, Nucl. Phys. **B178** (1981) 141.

[97] TASSO Collab., M. Althoff *et al*, Z. Phys. **C29** (1985) 29.

[98] Mark II Collab., A. Petersen *et al*, Phys. Rev. Lett. **55** (1985) 1954.

TPC/Two-Gamma Collab., H. Aihara *et al*, Z. Phys. **C28** (1985) 31.

[99] HRS Collab., D. Bender *et al*, Phys. Rev. **D31** (1985) 1.

[100] For a general review see D.H. Saxon, RAL-86-057 (1986).

[101] JADE Collab., W. Bartel *et al*, Z. Phys. **C21** (1983) 37.

JADE Collab., W. Bartel *et al*, Phys. Lett. **134B** (1984) 275.

[102] J.D. Bjorken, S.J. Brodsky, Phys. Rev. **D1** (1970) 1416.

[103] L. Clavelli, D. Wyler, Phys. Lett. **103B** (1981) 383.

[104] TASSO Collab., R. Brandelik *et al*, Phys. Lett. **113B** (1982) 499.

[105] P. Mättig, TASSO Note N^0 336 (1985).

[106] For a review of recent experimental results in two photon physics see:

S.L. Cartwright, RAL-86-100 (1986).

[107] J. Chwastowski, private communications.

[108] TASSO Collab., W. Braunschweig *et al*, DESY 88-050 (1988).

[109] F.A. Berends *et al*, Phys. Lett. **148B** (1984) 489.

[110] R.D. Field, R.P. Feynman, Nucl. Phys. **B136** (1978) 1.

[111] C. Youngman, TASSO Note N^0 147 (1980).

[112] Review of Particle Properties, Particle Data Group, M. Aguilar-Benitez *et al*, Phys. Lett. **170B** (1986) 104.

[113] K. Genser, TASSO Note N^0 366 (1986).

[114] F. James, M. Roos, Comput. Phys. Commun. **10** (1975) 343.

[115] K. Genser, private communications.

[116] L. Labarga, TASSO Note N^0 369 (1987).

[117] TASSO Collab., M. Althoff *et al*, Phys. Lett. **126B** (1983) 493.
JADE Collab., W. Bartel *et al*, Phys. Lett. **146B** (1984) 121.
HRS Collab., M. Derrick *et al*, Phys. Lett. **146B** (1984) 261.
TPC Collab., H. Aihara *et al*, Phys. Rev. **D34** (1986) 1945.

[118] R.J. Cashmore, Oxford Nuclear Physics 96/87 (1987).

[119] S. Bethke, Z. Phys. **C29** (1985) 175.

[120] The unfolded multiplicity distribution for the data was supplied by J. Chwastowski, private communications.

[121] TASSO Collab., W. Braunschweig *et al*, Oxford Nuclear Physics 42/88 and DESY 88-107; to appear in Z. Phys. C.

[122] B.R. Webber, private communications.

[123] P. Hoyer *et al*, Nucl. Phys. **B161** (1979) 349.

[124] K. Genser, P. Mättig, private communications.

[125] P.N. Burrows, Oxford Nuclear Physics 43/88 and DESY 88-122; to appear in Z. Phys. C.

[126] B.R. Webber, Phys. Lett. **143B** (1984) 501.

[127] Z. Koba, *et al*, Nucl Phys. **B40** (1972) 317.

[128] M.G. Bowler, P.N. Burrows, Z. Phys. **C31** (1986) 327.

[129] T. Sjöstrand, Z. Phys. **C26** (1984) 93.

[130] JADE Collaboration, W. Bartel *et al*, Z. Phys. **C33** (1986) 23.

[131] T. Sjöstrand, Comput. Phys. Commun. **28** (1983) 229.

[132] TASSO Collab., W. Braunschweig *et al*, Oxford Nuclear Physics 29/88 and DESY 88-046 (1988); to appear in Phys. Lett. B.

[133] F. Barreiro, S. Brandt, M. Gebser, Nucl. Instr. and Methods **A240** (1985) 237.

[134] F. Gutbrod, G. Kramer, G. Rudolph, G. Schierholz, DESY 87-047 (1987).

[135] P. Mättig, M. Dittmar, Z. Phys. **C35** (1987) 221.

[136] K. Kato, T. Munehisa, contributed paper to the XXIV International Conference on High Energy Physics, Munich, 4-10 August 1988.

[137] T. Kamae *et al*, contributed paper to the XXIV International Conference on High Energy Physics, Munich, 4-10 August 1988.

[138] S. Bethke, Proc. XXIII Rencontre de Moriond, Les Arcs (France), March 1988; LBL Report LBL-25247 (1988).

[139] JADE Collab., S. Bethke *et al*, DESY 88-105 (1988).

[140] AMY Collab., I.H. Park *et al*, Contributed paper to the XXIV International Conference on High Energy Physics, Munich, 4-10 August 1988.